Unravelling nanoscale molecular processes in organic thin films

Dissertation
zur Erlangung des akademischen Grades

doctor rerum naturalium
(Dr. rer. nat.)

im Fach Physik
Spezialisierung Experimentalphysik

eingereicht an der
Mathematisch-Naturwissenschaftlichen Fakultät
der Humboldt-Universität zu Berlin

von

Herrn M.Sc. Sebastian Bommel

Präsident der Humboldt-Universität zu Berlin
Prof. Dr. Jan-Hendrik Olbertz

Dekan der Mathematisch-Naturwissenschaftlichen Fakultät
Prof. Dr. Elmar Kulke

Gutachter: 1. Prof. Dr. Stefan Kowarik
2. Prof. Dr. Andreas Stierle
3. Priv.-Doz. Dr. Andreas Opitz

Tag der mündlichen Prüfung: 19.05.2015

Abstract

This thesis deals with thin films of conjugated molecules which have proven potential for applications in organic optoelectronics, biosensing, surface modification and nanoscale surface patterning. Despite their technological relevance many fundamental questions remain open regarding the supra-molecular assemblies within (crystalline) nanostructures. Molecular scale understanding is lacking regarding the surface processes during molecular self-assembly and regarding the stability of these films. Furthermore, we are only beginning to understand the role of internal and rotational degrees of freedom of the molecular building blocks on the thermal and mechanical properties as well as growth processes of these functional nanomaterials. To address these questions in this thesis *in situ* x-ray methods are used to monitor growth processes and atomic scale changes during annealing in organic thin films.

In the first part of this thesis we investigate the major surface processes during multilayer growth of the prototypical molecule C_{60}, that is the surface diffusion, nucleation and step-edge crossing. A novel combination of x-ray growth oscillations and real-time diffuse x-ray scattering provides information about the evolution of the thin film morphology. Moreover, by comparing the experimental findings with kinetic Monte-Carlo (KMC) simulations we determine, for the first time, a consistent set of energy parameters, yielding an effective Ehrlich-Schwoebel barrier of $E_{ES} = 110$ meV, a surface diffusion barrier of $E_D = 540$ meV and a binding energy of $E_B = 130$ meV. The interaction range between C_{60} molecules is shorter than the interaction range for atoms but longer than that of colloids. Therefore its growth behavior exhibits both atom-like features such as an E_{ES} of energetic origin, as well as similarities to colloidal growth with extended lateral diffusion. Not only C_{60} homoepitaxial growth but also substrate interactions have been considered for describing post-growth dewetting processes. For C_{60} a thermally-activated post-growth dewetting on mica has been observed for the first monolayer and from temperature-dependent measurements an effective activation barrier for upward interlayer transport of (0.33 ± 0.14) eV has been quantified.

In the second part of this thesis we turn to the investigation of the thermomechanical properties of the supra-molecular assembly of the organic semiconductor PTCDI-C_8. Temperature-dependent Grazing Incidence X-ray Diffraction (GIXD) experiments

reveal extraordinary large positive and, surprisingly, negative thermal expansion coefficients of the crystal structure. The molecules within the supra-molecular assembly perform temperature-controlled cooperative rotational motions leading to the change of the molecular crystal structure at different temperatures. The interplay between the increasing influence of molecular interactions for low temperatures, on the one hand, and the rising impact of entropy with increasing temperature, on the other hand, influences the structural evolution and gives rise to continuously tunable, reversible mechanical properties.

The results of this thesis provide quantitative descriptions of molecular scale dynamics regarding the movement of single ad-molecules as a function of growth conditions and regarding the cooperative motions of single molecules in supra-molecular and crystalline ensembles. We hope that our molecular scale picture of these processes will stimulate further work towards the optimized, rational design of functional molecular thin films and nanomaterials.

Kurzfassung

Die vorliegende Doktorarbeit beschäftigt sich mit der Untersuchung von dünnen Filmen aus konjugierten Molekülen, welche für die organische Optoelektronik, Bio-Sensorik, Oberflächenmodifikation und –Strukturierung genutzt werden. Trotz der technologischen Bedeutung gibt es offene Fragen bezüglich der supra-molekularen Anordnungen der Moleküle in (kristallinen) Nanostrukturen zu klären. Das Verständnis auf der molekularen Skala für die Prozesse während des Wachstums und die Stabilität solcher Filme fehlt. Außerdem steht man erst am Anfang den Einfluss der internen und Rotations-Freiheitsgrade der Moleküle sowohl auf die thermischen und mechanischen Eigenschaften als auch auf das Wachstum solcher Materialien zu verstehen. Um diese Fragen in dieser Arbeit anzugehen, werden Echtzeit Röntgenmethoden genutzt, um die Oberflächenprozesse während des Wachstums und den Einfluss der Temperatur auf organische dünne Filme zu beobachten.

Im ersten Teil der Arbeit untersuchen wir die bedeutendsten Oberflächenprozesse während des Wachstums von C_{60}, die Oberflächen-Diffusion, die Nukleation und die Stufenkanten-Diffusion. Mit der neuartigen Kombination von Röntgen-Wachstumsoszillationen und diffuser Röntgenstreuung erhalten wir detaillierte Informationen über die Entwicklung der Morphologie während des Wachstums. Durch einen Vergleich der experimentellen Ergebnisse mit kinetic Monte-Carlo (KMC) Simulationen bestimmen wir zum ersten Mal einen konsistenten Satz von Energieparametern zur Beschreibung der Wachstumsdynamik: eine effektive Ehrlich-Schwoebel Barriere von $E_{ES} = 110$ meV, eine Oberflächendiffusions-Barriere von $E_D = 540$ meV und die Bindungsenergie von $E_B = 130$ meV. Die Wechselwirkungsreichweite von C_{60} ist kürzer als die von Atomen, aber länger als die von Kolloiden. Daher weist das Wachstum von C_{60} Ähnlichkeiten zu atomaren Systemen auf, z.B. dass E_{ES} energetischen Ursprungs ist, wohingegen die ausgeprägte laterale Diffusion der von Kolloiden ähnelt. Für die Beschreibung der Stabilität von C_{60} Filmen nach dem Wachstum spielt nicht nur die C_{60}-C_{60} Wechselwirkung eine Rolle, sondern auch die Substrat-Wechselwirkungen. Für C_{60} auf Mica beobachten wir eine thermisch aktivierte Entnetzung nach dem Wachstum der ersten Monolage. Durch temperatur-abhängige Messungen ist eine effektive Aktivierungsenergie für Interlagen-Transport während des Entnetzens von (0.33 ± 0.14) eV bestimmt worden.

Der zweite Teil der Arbeit setzt sich mit den Untersuchungen der thermomechanis-

chen Eigenschaften von kristallinen dünnen Filmen des organischen Halbleiters PTCDI-C_8 auseinander. Temperatur-abhängige Röntgenstreu-Experimente (GIXD) zeigen, dass außergewöhnlich große positive und überraschenderweise negative thermische Ausdehnungskoeffizienten auftreten. Die Moleküle innerhalb des molekularen Ensembles vollführen kooperative rotierende Bewegungen als Reaktion auf die Temperaturänderung, die zu dieser anomalen thermischen Expansion führen. Das Zusammenspiel zwischen dem wachsenden Einfluss der intermolekularen Wechselwirkungen für niedrige Temperaturen und die steigende Bedeutung der Entropie des Systems für wachsende Temperaturen beeinflussen die Struktur-Ausbildung und führen zu den reversiblen Eigenschaften.

Die Ergebnisse dieser Arbeit beleuchten die Dynamik der Moleküle bzgl. der Bewegungen einzelner adsorbierter Moleküle während des Wachstums und bzgl. kooperativer Bewegungen einzelner Moleküle in supra-molekularen Ensembles. Unsere Beschreibung dieser Prozesse auf der molekularen Skala wird die weitere Arbeit auf dem Weg zu funktionalen molekularen dünnen Filmen beleben.

Contents

1 Functional organic nanomaterials

Molecular and organic semiconducting nanomaterials [1–4] are becoming increasingly significant in our everyday life. The advantages of molecular materials compared to inorganic ones, such as the large diversity of molecules with desired opto-electronic properties, the low-cost and large area processing [5–8], lead to an increased incorporation of organic materials in electronic and opto-electronic devices like organic photovoltaic (OPV) devices [9–11], organic-field-effect transistors (OFETs) [12–17] and organic light emitting diodes (OLEDs) [18–21]. OLEDs can be already found in smartphone displays as well as in television screens. The unbroken demand for low-cost and large area electronic devices makes molecular materials a subject of intensive research studies.

Importantly, the thin film growth, the resulting morphology and the molecular packing play a decisive role for the performance of molecular organic devices [9, 11, 22–27]. The molecular packing determines the overlap of π-conjugated orbitals and therefore the charge carrier mobility [28–30]. Thin film morphology has to be controlled , e.g. in photovoltaic devices, with regard to the exciton diffusion length for sufficient device performances [31].

Unravelling the growth for functional molecular nanomaterials

Therefore, understanding the growth of molecular materials on surfaces is an indispensable prerequisite for the rational design of complex nanomaterials from molecular building blocks, as well as for optimizing the performance in thin film-based applications such as solar cells and organic light emitting diodes [11,26–29,31]. So far, molecular self-assembly and growth on larger length scales has often been characterized by scaling laws to describe surface roughening and evolving island densities [32, 33]. To achieve a molecular scale understanding of the molecular thin film growth the three major surface processes during growth have to be unraveled:

- the surface diffusion of a single molecule,
- the lateral binding of molecules, which determines the formation of dimer, trimer and larger cluster of molecules,
- and the step-edge crossing when a substantial surface fraction is covered and incoming molecules are deposited on existing islands.

On this molecular level, a range of studies have elucidated the kinetics of diffusion and nucleation (see, for example, refs [34–39]) and the Ehrlich– Schwoebel barrier for interlayer transport across a molecular step edge [34,40–42]. In the last decades, the energy barriers for atomic growth have been refined to take into account the local neighborhood during multilayer growth, for example, by including concerted gliding of islands or by distinguishing between different step-edge orientations [43–46]. Yet to date, there is no organic compound for which even the 'minimal' set of the three parameters diffusion barrier, lateral binding energy and Ehrlich–Schwoebel barrier have been simultaneously quantified to describe multilayer molecular growth. Therefore, predictive simulations of the rate- and temperature-dependent morphology in molecular multilayer growth have so far been impossible, contrary to the situation for elemental atomic systems [47–49] and colloids [50–52]. Therefore the following question arises:

- *Question 1: Can a minimal set of energy barriers, which describes the fundamental surface processes during growth, be measured, which allows material scientists to perform predictive simulations on the design of future molecular materials?*

To address this challenging topic the lateral and vertical growth of the prototypical molecular semiconductor fullerene C_{60} [53–55] has been investigated by real-time and *in situ* x-ray scattering [56–60]. Kinetic Monte-Carlo (KMC) simulations [43, 61, 62] have been fitted to the experimental results on the layer coverages and the island densities as a function of growth temperature, deposition rate and time to quantify the energy barriers.

Importantly, C_{60} exhibits properties in between those of atoms and colloids. On the one hand, its van-der-Waals diameter of 1 nm [63] is closer to atomic dimensions than to the µm length scale of colloidal systems. On the other hand, C_{60} resembles colloids with its short-range nature of the effective center-of-mass interactions [64], which decay as $-1/r^9$ with r being the center-of mass separation stemming from the averaged van-der-Waals interactions (approximately $-1/r^6$) between the individual carbon interaction sites [65]. These forces between atomic, molecular or colloidal building blocks are of prime importance for kinetic growth processes [66, 67], similar to their role in equilibrium phase behavior and self-assembly [68, 69]. C_{60} is therefore not only relevant for device applications, but also an important, fundamentally unique material bridging atoms and colloids. Following this the second question of this thesis is:

- *Question 2: How does the intermediate range of attractive interactions of the fullerene C_{60} between elemental and colloidal systems influence the growth dynamics?*

The energy barriers describing the surface processes are not only essential for the kinetics during the growth but also after the growth is stopped. As growth is a non-equilibrium

process, which means that the structure during growth does not necessarily have to be the most stable one, post-growth reorganization [70,71] can occur and can obviously influence the stability of these low-dimensional nanostructures. The kinetic paths of the molecules during the reorganization process are directly influenced by the energy barriers. Therefore the third question is:

- *Question 3: Does post-growth dewetting occur for the material system of C_{60} on mica and what are the kinetics of the dewetting processes, e.g. as a function of temperature?*

Cooperative molecular rotations in organic thin films

The molecular scale understanding of the movement of single ad-molecules during growth and a rational choice of growth conditions ultimately leads to an optimized design of functional nanomaterials. Going one step further to a mechanical functionality of supramolecular assemblies the subsequent challenge is to address and control the internal and rotational degrees of freedom of the molecular building blocks with external stimuli. Such responsive materials [72] show the ability to respond to the external stimuli like heat or irradiation of light by mechanoresponsive processes on the molecular and/or supramolecular level. These materials have attracted increasing attention because of their potential in data storage [73], bio-nanotechnology [74] and molecular scale mechanics [75–80]. To translate molecular motions to macroscopic levels many molecular building blocks within a highly crystalline material, such as the organic semiconductor PTCDI-C_8 [81], must be able to alter cooperatively.

These cooperative mechanical motions on the nanoscale can be found in materials with large positive and, especially, negative thermal expansion (NTE) [82–84]. NTE materials, for which the interatomic/ intermolecular distances contract upon heating, can be found for liquids like water in the temperature range of $0-4$ °C, for inorganic materials like metal oxides [85–87] and metal-organic frameworks (MOFs) [88,89]. For metal oxides and MOFs (correlated) translational-rotational motions [87,88] of compound-subgroups as a function of temperature lead to an NTE within the crystalline material. NTE materials can rarely be found for pure organic materials such as polymers [75] and organic crystals [90–93]. Following this the fourth question of this thesis arises:

- *Question 4: What is the impact of temperature on the surface crystal structure of the organic semiconductor PTCDI-C_8 ?*

The appearance of NTE goes beyond the normal thermal expansion. Thereby, an increase of temperature causes an increase of the anharmonic vibrations of the involved

atoms about their equilibrium positions. However, for large positive and especially for negative thermal expansion this explanation cannot be used anymore. To explore the driving force of NTE in organic materials is challenging. Organic crystals are held together by weak van-der-Waals, electrostatic and/ or hydrogen-bonding forces [94, 95], which easily expand upon heating. For molecules with asymmetric dimensions the additional vibrational and rotational degrees of freedom have to be considered for describing the cooperative molecular processes during annealing. Therefore the fifth question this thesis tackles is:

- *Question 5: What is the impact of temperature on the molecular orientations of the asymmetric PTCDI-C_8 molecule and which mechanism governs the anomalous thermal expansion in organic thin films?*

Analyzing molecular processes, such as the movement of single ad-molecules on the surface as a function of growth conditions for the prototypical molecular semiconductor C_{60} and cooperative mechanical motions of molecules in supra-molecular and crystalline ensembles of PTCDI-C_8, yields a broader fundamental understanding of molecular scale dynamics in regard to intermolecular interactions. This molecular scale understanding helps to make one step further to the rational design of molecular functional nanomaterials.

The thesis is organized as follows: After the introduction (chapter 1) a brief overview to the growth of (molecular) thin films and the intermolecular interactions in molecular solids is given in chapter 2. Chapter 3 deals with the basics of the applied x-ray scattering techniques. In chapter 4 the growth of the fullerene C_{60} is discussed and in chapter 5 the temperature-dependent structure of PTCDI-C_8 is illuminated.

Parts of the work summed up in this thesis have been published or are to be published soon. Please see the publication list at the end of this thesis.

2 Molecular organic thin films

Molecular organic thin films are increasingly used in organic devices ranging from electronics and biosensing to opto-electronics. Two major material classes of organic semiconducting materials can be distinguished: i) small molecules and ii) conducting polymers. While small molecules have a limited size of a few nanometers, polymers consist of repeating building blocks resulting in sizes of up to 100 nm. For both the opto-electronic properties are governed by delocalized π-conjugated electron system.

Importantly, the thin film growth, the resulting morphology and the molecular packing play a decisive role for the performance of organic devices [9, 11]. For the formation of such supra-molecular assemblies the intermolecular interactions such as van-der-Waals and electrostatic forces are of great importance [28, 66, 67].

Therefore, this chapter review the most important aspects of molecular thin film growth and the intermolecular interactions in molecular organic thin films. In the first section the atomistic growth process will be discussed giving insights in possibilities of modeling the growth by using rate equations and kinetic Monte-Carlo methods. In the following section, a brief introduction on the intermolecular forces in molecular crystals is given. The molecular materials and the substrates used here are briefly presented in the next section of this chapter. For C_{60} the short range of attractive interactions is discussed in detail compared to atomic and colloidal interactions. Finally, a description of the Organic Molecular Beam Deposition (OMBD) system is given, which has been used in this thesis for the growth of molecular thin films.

2.1 Molecular thin film growth

For the fabrication of molecular thin films and therefore for organic devices the two processes of solution-based fabrication and vacuum deposition like organic molecular-beam deposition [5–7] are the methods of choice. For the vacuum-based deposition used in this thesis the processes during growth of thin films can be summarized as follows. Molecules are deposited on the surface, which has a temperature T, with a rate f. After impinging on the surface the single molecule (ad-molecule) performs a random-walk on the surface, which is characterized by the diffusion coefficient D. For hopping from one

adsorption site to the other a molecule has to overcome the diffusion barrier E_D (see Figure 2.1). Dimer, trimer and larger island clusters are formed by the lateral aggregation of ad-molecules. The lateral binding between two molecules is quantified by a lateral binding energy E_B. The total lateral binding energy of a cluster of $s+1$ molecules is $s \cdot E_B$. Once a substantial surface fraction is covered molecules deposited on top of an existing island become more important. These molecules can either descend from the island contributing to the formation of a full single layer or remain on the layer starting the nucleation of the next layer.

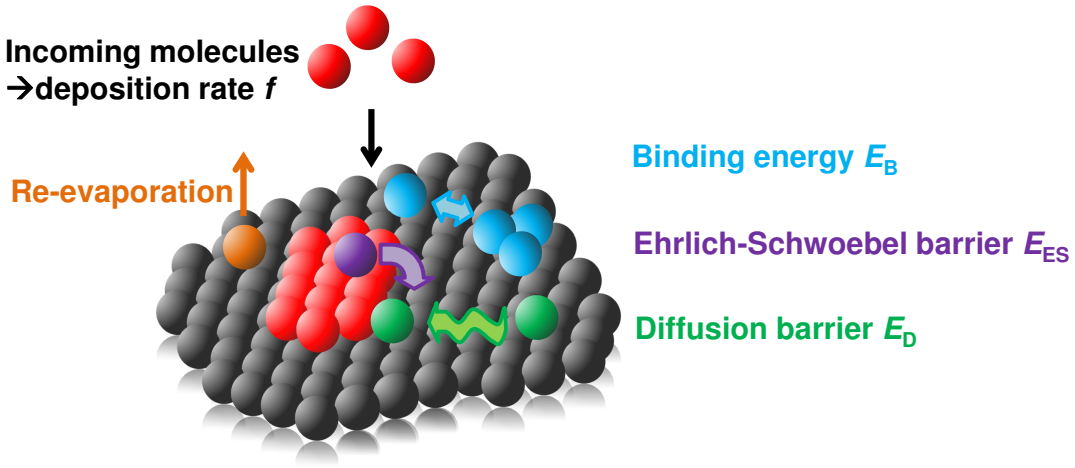

Figure 2.1: Molecular processes during growth. The diffusion barrier, binding energy and the Ehrlich-Schwoebel barrier play the decisive role during the growth as they can be accounted for the thin film morphology.

For descending from the island the molecules have to overcome an additional energy barrier, called Ehrlich-Schwoebel barrier, E_{ES}. Such barrier was first observed for tungsten on tungsten growth in 1966 by Ehrlich and Hudda [96] and its consequences for stepped surface growth were analyzed by Schwoebel and Shipsey [97]. The physical origin of the additional energy barrier can be understood in a simplified picture. A molecule or an atom descending a step-edge traverses a transition state of lower coordination, which is directly connected to weaker binding and thus a higher energy [98]. Importantly, the occurrence of the step-edge barrier depends on the range of interactions. In colloids, the range of attractive interactions is so small that the reduced coordination associated with an edge is not 'sensed'. This effectively leads to the vanishing of an energetic barrier at the edge. Instead, one observes a purely diffusive pseudo Ehrlich–Schwoebel barrier, arising from a lower diffusion probability along the geometrically longer path across the step edge [50].

Generally, the intra- and interlayer hopping processes are thermally activated processes. The energy E_D needed for hopping from one adsorption site to the other determines the diffusion coefficient D. The diffusion coefficient D can be written in terms of a hopping rate as a Arrhenius law

$$D = \nu_0 \cdot exp\left(-\frac{E_D}{k_B T}\right). \tag{2.1}$$

ν_0	Attempt frequency, typical magnitude 10^{13} Hz
E_D	surface diffusion barrier
k_B	Boltzmann constant
T	Temperature

While for the first monolayer the interaction of the molecule and the substrate plays the decisive role for surface diffusion for layers beyond the first one the molecule-molecule interaction is a key parameter. Consequently, one would expect a change of the aggregation behavior as it was observed, e.g. for diindenoperylene (DIP) on SiO_2 [99]. Furthermore, the temperature is not only the decisive parameter for the surface processes but also for the re-evaporation of molecules, which finally determines the sticking coefficient.

However, thin film growth cannot be characterized exclusively by equilibrium thermodynamics as the processes during growth are kinetically limited. Therefore, the observed structures during growth are not necessarily the most stable structures. But these structures can be described by considering the detailed kinetic path of the molecules during growth taken the different surface processes into account. Such kinetically limited growth can lead to post-growth reorganization in organic thin film growth [70, 71, 100]. This is one of the reasons for performing real-time and *in situ* observation of growth. Please see reference [101] for further reading on the balance between kinetics and thermodynamics during growth.

2.1.1 Modelling growth: from rate equations to kinetic Monte-Carlo (KMC) simulations

The above described molecular scale processes such as surface diffusion, the lateral binding between molecules and the step-edge crossing govern the thin film growth of complex nanostructures. To describe the growth processes the thin film growth have to be compared with dedicated models and/or simulations. From modelling thin film growth the energy barriers can be quantified, which makes predictive simulations of complex nanostructures possible.

In this section a brief overview of theoretical possibilities of modeling thin film growth will be given. However this section cannot cover the entire progress made in the last decades. Further details can be found in references [47, 48, 98, 102]. Please note, that the growth theories were developed for the growth of atomic systems but will be discussed regarding the growth of molecules in the following.

2.1.1.1 Rate equation approach for modeling ad-atom and island density

For following particle ensembles (atoms, molecules and even colloids) during growth an atomistic theory of nucleation was developed in the 1960's and 70's by Zinsmeister [103–105], Stowell [106] and Venables [102, 107]. Only the elements of the two-dimensional nucleation theory most relevant to this work will be presented. A key parameter in the two-dimensional nucleation theory is the critical cluster size i^*. Cluster consisting of i^*+1 molecules are assumed to be stable and cannot disintegrate. From analyzing net rates for the attachment of particles (atoms or molecules) rate equations for the total density of stable clusters N, the density of ad-molecules n_1 and for the coverage of stable clusters θ can be derived. The rate equation for the island density N is fed by the ad-molecule density n_1 [98]:

$$\frac{dN}{dt} = \underbrace{\sigma_{i^*} D n_1 n_{i^*}}_{\text{Formation of stable cluster}} \underbrace{-2N\frac{d\theta}{dt}}_{\text{Loss due to coalescence}} \quad . \tag{2.2}$$

σ_{i^*} is a capture number describing the propensity for a cluster consisting of i^* molecules to capture an ad-molecule. D denotes the diffusion coefficient (see equation 2.1). n_1 is the density of ad-molecules. Furthermore, the density of clusters consisting of i^* molecules is represented by n_{i^*}. In general, the density of clusters of s-molecules n_s can be written as [98]

$$n_s \approx (n_1)^s exp\left(\frac{E_s}{k_B T}\right) \text{ for } (2 \leq s \leq i^*). \tag{2.3}$$

E_s is $\propto E_B$ and denotes the total binding energy of a cluster of s molecules. That is the energy needed to separate a cluster into single ad-molecules [98]. The energy for a single ad-molecule E_1 is 0. For the derivation of the ad-molecule density n_1 a complete condensation of impinging molecules is assumed. Consequently, the ad-molecule density is decreased by the formation of stable clusters and the capturing at larger clusters. By introducing an average capture number for stable islands $\bar{\sigma}$ the rate equation for the

density of ad-molecules n_1 can be written as [98]

$$\frac{dn_1}{dt} = f \underbrace{- \sigma_{i^*} D n_1 n_{i^*}}_{\text{Loss due to stable cluster formation}} \underbrace{- \bar{\sigma} D n_1 N}_{\text{Loss due to capture at larger clusters}} \tag{2.4}$$

From equations 2.2, 2.3 and 2.4 the island and ad-molecule densities can be fitted to the experiment in order to get information about surface diffusion barrier and binding energy of a certain material system. The capture numbers σ_{i^*} and $\bar{\sigma}$ can be held constant for many purposes [98, 102].

From equations 2.2 and 2.4 two different temporal regimes can be derived.

1. Transient nucleation regime

   For early times the loss terms for the ad-molecule density in equation 2.4 can be neglected. This yields the following expressions for the ad-molecule density n_1 and the island density N as a function of the total coverage $\theta = f \cdot t$:

   $$n_1 \propto \theta \tag{2.5}$$
   $$N \propto \theta^{i^*+2}. \tag{2.6}$$

2. Steady state nucleation regime

   As the capture of ad-molecules by stable islands is getting more important the steady state regime sets in. The incoming molecules are almost completely captured by stable clusters resulting in the balance of the incoming particle flux f and the last loss term in equation 2.4, which gives a rough estimate of the ad-molecule density as a function of the island density N

   $$n_1 \approx \frac{f}{D\bar{\sigma}N}. \tag{2.7}$$

   Using this for equations 2.2 and 2.3 and integrating over time gives (neglecting the coalescence) the key result of nucleation theory is:

   $$N \approx \theta^{\frac{1}{i^*+2}} \left(\frac{f}{D}\right)^{\frac{i^*}{i^*+2}} exp\left(\frac{i^* \cdot E_B}{k_B T}\right) \tag{2.8}$$
   $$N \propto \left(\frac{f}{D}\right)^{\frac{i^*}{i^*+2}}. \tag{2.9}$$

   This scaling law directly connects the kinetic parameters diffusion coefficent D and deposition rate f with the island density measured in the experiment. Notably, the

law is only valid for a low coverage regime as coalescence effects were negelected. This coalescence effect leads to a decrease of the island density N as islands merge together and, hence, the island density exhibit a characteristic maximum.

Importantly, the above rate equations do not include the nucleation of a second layer. For the consideration of the nucleation of top layers the interlayer diffusion, characterized by the Ehrlich-Schwoebel barrier, has to be integrated in a proper way. One theoretical approach was introduced by Trofimov *et al.* [108, 109]. For other theoretical approaches dealing with second layer nucleation and the incorporation of interlayer transport I refer to the references [34, 47, 98, 110].

2.1.1.2 Analytical mean-field growth model by Trofimov

Trofimov *et al.* [108] extended the rate equations model by Venables [102] presented in the last section by the incorporation of a feeding zone, which controls the interlayer transport and therefore the nucleation of a top layer on an existing layer. Therefore, the atomistic analytical model provides rate equations for ad-molecule density, island density and coverage for each layer [108]. Woll *et al.* [110] simplified the model by neglecting in-plane information such as island and ad-atom density ending up with just one rate equation for the coverage of the s-th layer θ_s:

$$\frac{d\theta_s}{dt} = \begin{cases} R_1(1-\theta_1) + R_{s>1}(\theta_1 - \xi_1) & \text{for } s = 1 \\ R_{s>1}(\xi_{s-1} - \xi_s) & \text{for } s > 1. \end{cases} \tag{2.10}$$

The parameter R_s incorporates the sticking coeffienct of the s-th layer.

The feeding zone parameter ξ_s (see Figure 2.2 for an illustration) for the s-th layer denotes an area on top of the s-th layer where arriving molecules will contribute to the growth of the $(s+1)$-th layer if they hit within the zone or jump down to the lower layer if they hit outside the feeding zone [108, 111]. The feeding zone parameter ξ_s is defined as follows:

$$\xi_s = \begin{cases} 0 & \text{for } \theta_s < \theta_{s,cr} \\ 1 - exp\left(-\left[\sqrt{-ln(1-\theta_s)} - \sqrt{-ln(1-\theta_{s,cr})}\right]^2\right) & \text{for } \theta_s \geq \theta_{s,cr} \end{cases}. \tag{2.11}$$

Here, the critical layer coverage $\theta_{s,cr}$ of the s-th layer gives the coverage of a layer that has to be reached before the $(s+1)$th layer starts to nucleate on top of it. This rate equation of the layer coverage has been widely used to quantify the vertical layer filling during the growth of organic thin films [99, 110–113]. Additionally, the model enables the quantification of the interlayer transport rate [111]. Therefore, the model is also used in

this thesis for the quantification of the layer filling during the organic thin film growth in Section 4.2. In the last sections it was demonstrated that rate equations and scaling laws can be used for following the ad-molecule density, the island density and the layer coverage during growth.

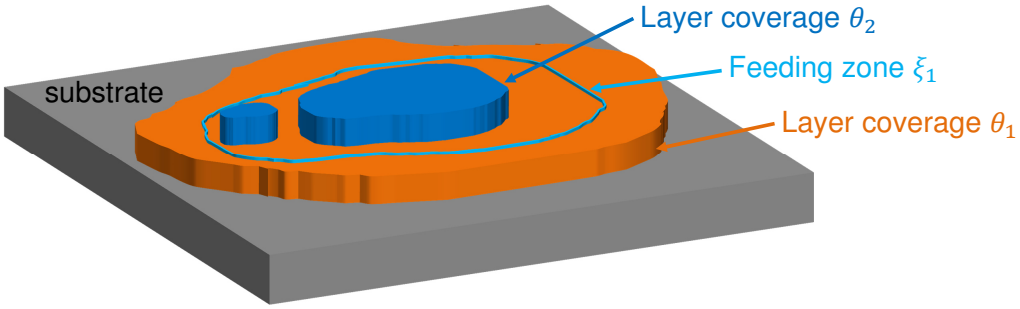

Figure 2.2: Illustration of the feeding zone introduced in the analytical growth model of Trofimov *et al.*. The feeding zone parameter for the s-th layer ξ_s denotes an area on top of the s-th layer where arriving molecules will contribute to the growth of the $(s+1)$-th layer if they hit within the zone or jump down to the lower layer if they hit outside the feeding zone. In this way, the parameter controls the interlayer transport during the growth.

Therefore, they can be used for the quantification of the surface diffusion barrier, lateral binding energy, critical island size i^* and interlayer transport by comparing experimental and theoretical measures such as island density and layer coverage.

Nevertheless, rate equations and scaling laws are limited as, for instance, they are based on the distinction between stable and unstable clusters and provide no information about the real-space morphology such as island shapes during growth or particle-resolved dynamics. Further, the derived scaling laws are only valid for a very limited range of layer coverages during the growth.

2.1.1.3 Kinetic Monte-Carlo (KMC) Simulations of the thin film morphology

To follow the complete evolution of morphology during multilayer growth on a single-particle level kinetic Monte-Carlo (KMC) simulations is the method of choice. KMC methods enable the modeling of a large time and length scale (approx. 10^7 particles). While molecular details such as molecular vibrations are neglected the evolution of a system is directed by events and associated rates (*coarse-grained* approach). These rates have to be adapted to the specific problem.

Growth simulations are usually performed on a lattice representing the adsorption sites of the atoms or molecules (e.g. on a (111)-fcc surface). The intra- and interlayer diffusion

of a particle at site i to a site j is conducted via an activated process with an Arrhenius-type rate $r_{i,j}$, which can be defined as

$$r_{i,j} = \frac{2k_BT}{h} \cdot exp\left(-\frac{E_D + s_iE_B + m_{i,j}E_{ES}}{k_BT}\right). \tag{2.12}$$

There are several approaches for the incorporation of the lateral bonding [48]. The presented rate follows the Clarke-Vvedensky bond-counting approach [114, 115]. The prefactor $\nu_0 = 2k_BT/h$ is chosen in accordance with previous KMC studies for atomic systems [116–118]. For leaving the adsorption site i a particle has to overcome a total energy barrier if the event has to occur. The total energy barrier consists of a barrier for free diffusion, E_D, and a lateral binding energy E_B, which contributes with the number of lateral neighbors s_i. The Ehrlich-Schwoebel barrier E_{ES} has to be considered ($m_{i,j} = 1$), if the particle at site i crosses an up- or downward step to reach site j. Otherwise, the lateral diffusion ($m_{i,j} = 0$) is given by the surface diffusion barrier and the lateral binding energy. Notably, more complex rates can be derived when taking the orientation of the step-edge or the different diffusion paths around a step-edge into account [44]. With the KMC input parameters T (substrate temperature) and f (deposition rate), which are taken directly from the experiment, the evolution of thin film growth can be followed. The comparison between experimental measures like island shape, island density and layer coverages and the simulated data gives an estimate of the surface processes represented by the energy barriers. Additionally, particle-resolved dynamics enables us to quantify the diffusion process of particles [112]. Further details of KMC simulations can be found in the references [43, 61] and the references therein.

Within this thesis KMC techniques have been used for the simulation of the multilayer growth of the fullerene C_{60} in Section 4. The simulations were performed by N. Kleppmann in the group of Prof. S.H.L. Klapp at the TU Berlin.

2.1.2 Growth modes

So far, nano- or microscopic processes during growth, which are relevant for the thin film formation, have been discussed. As a result of these individual processes different morphologies of the grown film can be formed on the macroscopic length scale. An established approach to describe the formation of the macroscopic growth modes uses the surface free energies of the substrate $\gamma_{\text{substrate}}$ and the thin film γ_{film} and the interfacial free energy between the substrate and film $\gamma_{\text{interface}}$ [5, 102, 107]. Generally, the system tends to grow in an energetically favored state (minimized energy).

Vollmer-Weber growth: formation of 3D islands For $\gamma_{\text{film}} + \gamma_{\text{interface}} > \gamma_{\text{substrate}}$ the formation of 3D islands is favored as the material system tends to leave the substrate uncovered (see Figure 2.3).

Frank-van-der-Merve growth: layer-by-layer growth The thin film tends to form layer by layer instead of isolated islands, when $\gamma_{\text{film}} + \gamma_{\text{interface}} < \gamma_{\text{substrate}}$.

Stranski-Krastonov growth: layer-island growth This growth mode is a mixture of the aforementioned modes. First, one (or more) completely filled layer is built (wetting layer), which is followed by the formation of isolated islands. The transition from wetting to dewetting can be explained by the differences of substrate-adsorbate and adsorbate-adsorbate energies. Furthermore, also differences of the bulk energy of the different layer, for example because of substrate induced strain may cause a transition form 2D (layer-by-layer) to 3D (island) growth.

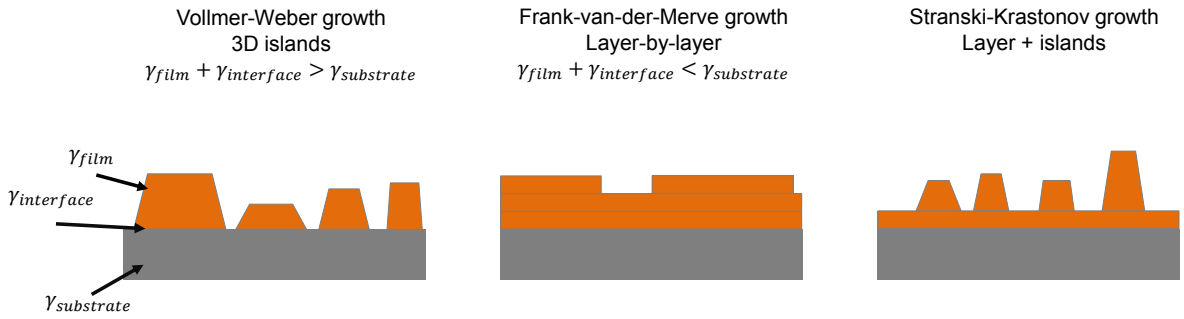

Figure 2.3: Macroscopic growth modes. During the growth of small molecules or atoms different growth modes can occur depending on the surface free energies of the substrate $\gamma_{\text{substrate}}$, the thin film γ_{film} and the interfacial free energy between the substrate and film $\gamma_{\text{interface}}$. One distinguishes between the formation of 3D islands (Vollmer-Weber growth), layer-by-layer growth (Frank-van-der-Merve growth) and the formation of islands on top of one (or more) wetting layers (Stranski-Krastonov growth).

2.2 Organic and molecular crystals

Highly crystalline molecular arrangement can be formed during molecular thin film growth. The structure of a (surface) crystal is the result of the minimization of the energy of the material system. Note, that for surface structures also the surface and interfacial energies have to be considered. Furthermore, the molecular arrangement and, in particular, the molecular packing of the crystal structure is a result of intermolecular forces between the molecules within the crystals.

2.2.1 Inter- and intramolecular interactions

Depending on the charge distribution within the molecule different forces contribute to the crystal formation.

***Van-der-Waals* forces** Attractive forces between two neutral and nonpolar molecules (no static dipole moment) are called *van-der-Waals* or dispersive forces. Fluctuating dipole moments due to temporally changing charge distributions within one molecule induce a dipole moment in a neighboring molecule, which directly give rise to the attractive forces between the molecules. Generally, this dipole-dipole interaction potential of two dipoles as a function of the distance r can be expressed as

$$V_{dis}(r) = -\frac{A}{r^6}. \tag{2.13}$$

A denotes a material specific constant.

Repulsive forces In addition to the dispersive forces there are repulsive forces from the inner electrons and the atomic nuclei, which prevent the molecular crystal from collapsing. Coulomb repulsion and the Pauli principle causes the repulsive forces. If two molecules come closer, it is forbidden to find additional electrons in the regions where the fully-occupied orbitals overlap. An theoretical approach to describe this model uses the following potential

$$V_{rep}(r) = \frac{B_n}{r^n} \tag{2.14}$$

with the material specific constant B_n and $n = 8..15$.

For $n = 12$ the *Lennard-Jones potential* describing the attraction and the repulsion

between atoms and molecules is derived (see Figure 2.4 for an illustration of the potential):

$$V_{LJ}(r) = \frac{B_{12}}{r^{12}} - \frac{A}{r^6} \tag{2.15}$$

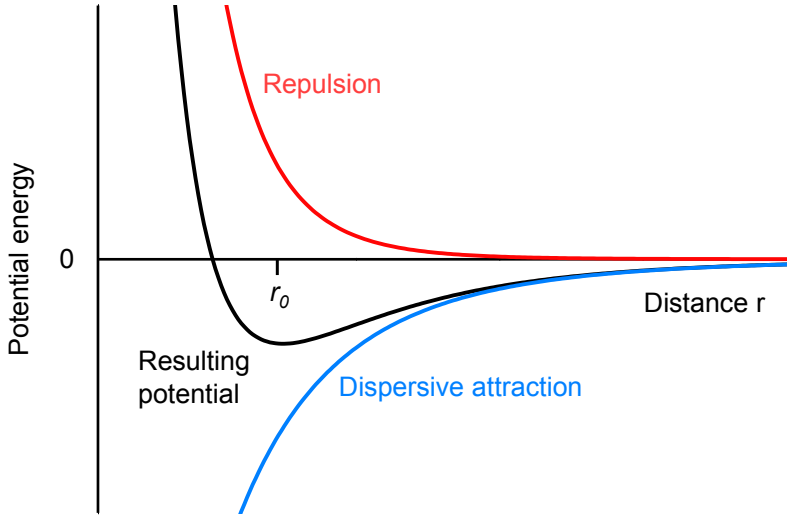

Figure 2.4: Potential energy between two atoms or molecules. The interaction between two atoms or molecules is hallmarked by attractive and repulsive forces. The equilibrium distance between two particles is denoted by r_0.

An alternative approach for describing the attractive and repulsive interactions between two atoms or molecules is the Morse potential [119]

$$V_{Morse}(r) = D_e((1 - exp(-\beta(r - r_0)))^2 - 1) \tag{2.16}$$

with D_e being the dissociation energy and r_0 the equilibrium distance. The equilibrium distance for C-C bonding is 0.12 nm - 0.15 nm.

Electrostatic coulomb forces: dipole-dipole interaction For molecules with polar substitutes and a permanent dipole moment and molecules, which are charged in a heteropolar fashion, e.g. crystal salts, the intermolecular forces between molecules are naturally determined by a static monopole, dipole and quadrupole. The Coulomb forces with their long range are particular interesting for special types of crystals like donor-acceptor complexes and radical-ion salts.

A special case for an electrostatic dipole-dipole interaction is the *h-bonding*. The positive partially charged hydrogen atom bonds to a more negatively charged atom like oxygen, nitrogen or fluorine [120].

2.2.2 Molecular crystal structures

The least repulsive and the densest packing within the crystal is energetically favored, which will be determined by atom-atom potentials.

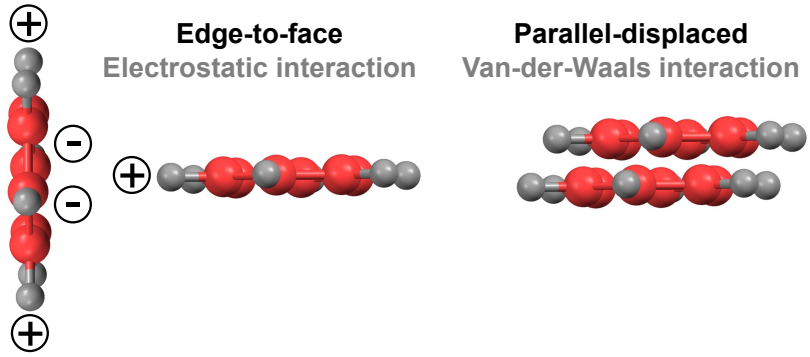

Figure 2.5: Competition between attractive forces and the static quadrupole forces in molecular crystals. Benzene shows two conformational arrangements, the face-to-edge and parallel-displaced arrangement, due to the electrostatic and van-der-Waals forces.

The formation of molecular crystalline structures is strongly influenced by the different intermolecular interactions. Especially in π-conjugated organic systems of complex molecules the competition between attractive forces and the static quadrupole forces gives rise to the formation of specific bonding configurations. This can be observed for the formation of a benzene dimer in Figure 2.5. The edge-to-face/ T-shaped arrangement of two benzene molecules is favored in the gas- and liquid phase due to electrostatic forces [121]. Beside the T-shaped arrangement calculations show, that also a parallel-displaced arrangement of benzene molecules exist, which is favored by van-der-Waals forces [121]. This conformation of molecules maximizes the dispersive attractions by maximizing the polarizable contact area. The parallel-displaced arrangement can also be understood regarding the intrinsic structure of the planar molecule. Planar molecules are not stucture-less as the van-der-Waals diameter of atoms correspond to "hills" and the space between two adjunct atoms denotes a valley. Conformations in which hills are directly positioned above a valley are energetically favored due to involved electrostatics compared to a arrangement in which the molecules directly lie above one another. The parallel-displaced face-to-face configuration can be found for the aromatic molecule PTCDI-C_8 [16] following the close-packed condition and optimized intermolecular interactions. PTCDI-C_8 has one molecule per unit cell, so that the molecules are equivalent under translation [121].

For further reading please see the references [94, 121] and the references therein.

2.2.3 Crystal structures upon temperature treatment

When changing the temperature of a crystalline structure, either in a crystal or in a thin film, the structure will be adopted according to the minimization of the energy of the structure. For an increase in temperature the impact of the entropy increases. In contrast, for decreasing temperature ($T \to 0$) the inner energy given by the intermolecular interactions almost exclusively determine the structure formation. Consequently, for temperature-dependent studies of the crystalline structure the intermolecular interactions as well as the entropy have to be considered.

Materials usually expand upon heating as the interatomic bond length increase due to "longitudinal vibrations". This can be understood using the potential energy versus interatomic distance diagram given by the Lennard-Jones (see equation 2.15) or the Morse potential (2.16).

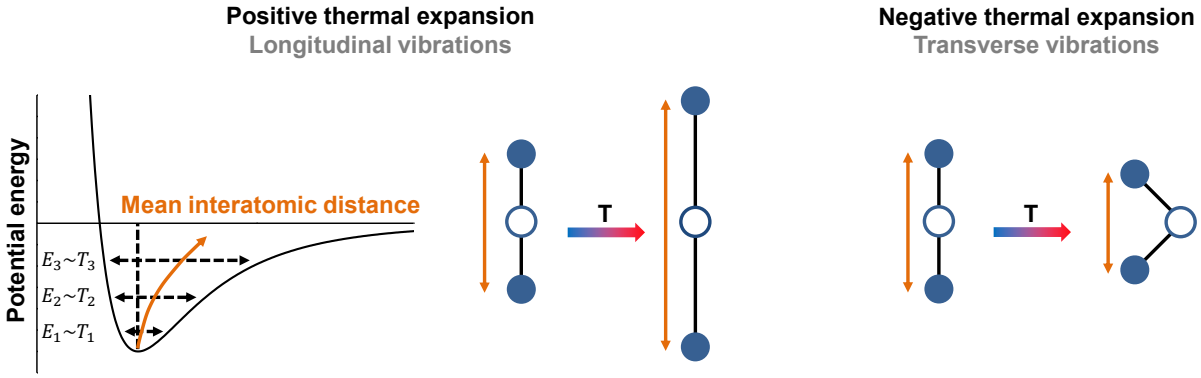

Figure 2.6: Positive and negative thermal expansion. Materials usually expand upon heating as the potential energy rises due to the increase in temperature, which directly lead to an increase of the mean interatomic distance. This positive thermal expansion is attributed to longitudinal vibrations. However, some materials contract with increasing temperature, which can be attributed to transverse vibrations.

While increasing the temperature the vibrational energy rises and because of the asymmetric potential the mean interatomic distances increase (see Figure 2.6). The thermal expansion can be quantified by a linear expansion coefficient α

$$\alpha = \frac{\Delta l}{\Delta T} \frac{1}{l_0} \tag{2.17}$$

with the change in length Δl for a particular temperature change $\Delta T = T_2 - T_1$ and the initial length l_0.

Interestingly, there are a few materials, for which the interatomic/ intermolecular distances contract upon heating. This negative thermal expansion (NTE) was observed in

metal oxides [82, 85–87], metal-organic frameworks (MOFs) [88, 89], polymers [75] and organic crystals [91–93]. In all cases the NTE is accompanied by structural, in particular rotational changes within the molecular material. For metal oxides and MOFs (correlated) translational-rotational motions of compound-subgroups as a function of temperature, which are caused by transverse vibrations [82], lead to an NTE within the crystalline material. As organic crystals are held together by weaker van-der-Waals, electrostatic and/ or hydrogen-bonding forces, which easily expand upon heating, the mechanisms for NTE in organic materials are complex.

In addition to the usual tranverse vibrations in organic molecules hinge- or scissor-type motion could explain the appearance of the NTE. In general, the NTE reported yet is attributed to the change of molecular orientations of the organic material. In pentacene crystals negative thermal expansion was accompanied with a change of the herringbone angle within the molecular packing [93]. For dumbbell-shaped organic molecules the molecular tilt (angle between long molecular axis and a crystal plane) decreases, which causes the *a*-axis to expand and the *b*- and *c*-axis to become shorter with increasing temperature [91, 92].

For a more detailed information on NTE I refer to recent reviews [82–84] of this research topic.

2.3 Molecular materials

In this thesis two different types of small molecules were used for the investigation of surface processes during growth and of the rotational motions upon annealing, the fullerene C_{60} and PTCDI-C_8 , which will be briefly introduced in the following.

2.3.1 Fullerene C_{60}

The Buckminsterfullerene C_{60} was discovered by Kroto *et al.* [54] as one of the most stable carbon clusters in the interstellar medium in 1985 [53, 55]. The discovery has opened the door for the further research of carbon nanomaterials like carbon nanotubes [122–124] and graphene [125, 126]. The C_{60} molecules, shaped like a truncated icosahedron ("football-molecule", see Figure 2.7a for an illustration), form close-packed crystals exhibiting either an fcc- or a hcp-crystal-structure [127–130]. The lattice parameter of the fcc-structure is 1.4156 Å [128]. At room temperature C_{60} exhibits orientational disorder rotating freely around the crystal sites. In contrast, for temperatures below 239 K an orientational order is formed [130, 131]. In addition to the impact on basic science, e.g. the demonstration of the wave-particle duality in quantum mechanics [132] and the realization of a single-C_{60} transistor [133, 134], C_{60} has emerged to a prototypical molecule for studying fundamental

processes in organic/ polymeric devices [10, 22, 135–139]. C_{60} is used in organic solar cells as an electron acceptor to investigate, e.g., the correlation of structure and morphology to device performance in organic solar cells [9, 11, 22].

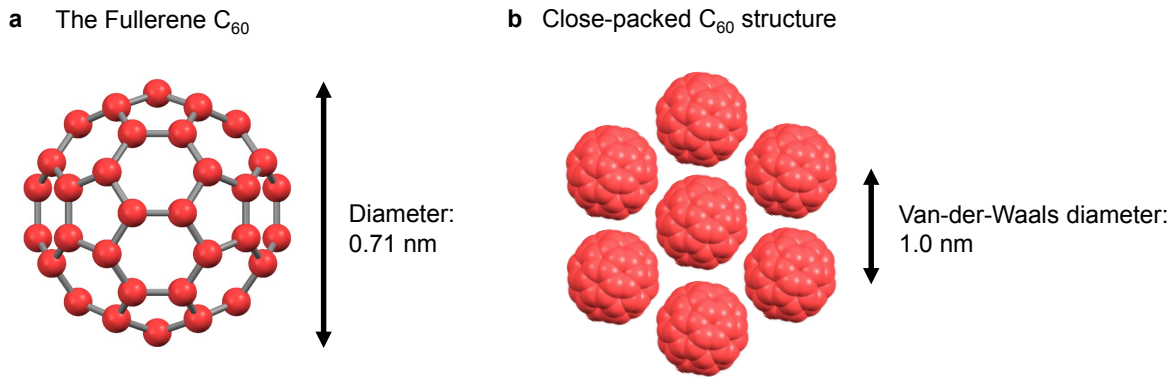

Figure 2.7: Fullerene C_{60}. (a) The 60 carbon atoms of the C_{60} molecule are arranged as a truncated icosahedron ("football-molecule"). (b) In the hexagonal close-packed structure of C_{60} molecules the distance between two nearest neighbors (*van-der-Waals* diameter) is 1.0 nm.

In this thesis the morphology formation of C_{60} thin films during the molecular self-assembly has been investigated with regard to the interaction range of the molecule. Therefore the following paragraph will give an introduction to the interaction range of C_{60} compared to atomic and colloidal systems.

Attractive interaction range of C_{60} compared to atoms and colloids The effective, centre-of-mass interaction between two C_{60} molecules decays significantly faster to zero with the (centre-of-mass) distance r than that between atoms. Specifically, the potential has the form [64, 65] (as obtained based on a calculation of Girifalco [140])

$$V_{C_{60}}(r) = \frac{\epsilon_{C_{60}}}{34}\left[9\left(\frac{1.047\cdot\sigma_{C_{60}}}{r}\right)^{43} - 43\left(\frac{1.047\cdot\sigma_{C_{60}}}{r}\right)^{9}\right] \tag{2.18}$$

, where ϵ is the depth of the potential and σ the centre-of-mass separation at which the potential is zero. The distance dependence of the attractive part of the potential, $-1/r^9$, results from an angle-average over all van-der-Waals interactions ($1/r^6$) between the individual carbon sites.

Contrary to equation 2.18, the attractive interaction between atoms can be described by a conventional Lennard-Jones potential which decreases with $-1/r^6$ for large distances:

$$V_{atom}(r) = 4\epsilon_{atom}\left[\left(\frac{\sigma_{atom}}{r}\right)^{12} - \left(\frac{\sigma_{atom}}{r}\right)^{6}\right]. \tag{2.19}$$

Note the significantly shorter attractive interaction range of C_{60} compared to atoms when normalized to their respective diameters.

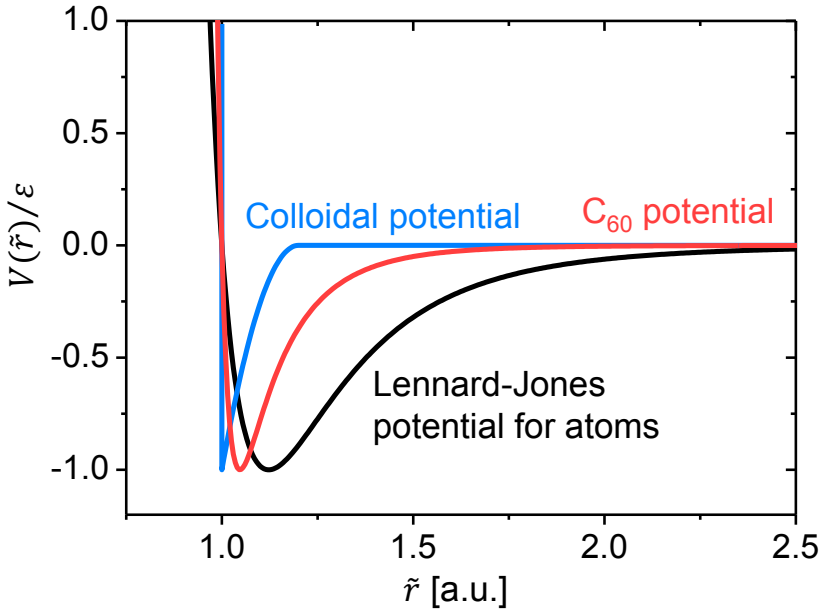

Figure 2.8: Attractive interaction range of C_{60} compared to atoms and colloids. Attractive interaction potentials for argon-atoms (black), the fullerene C_{60} (red) and colloids (blue) are shown. For comparison the potential has been expressed in terms of a respective value of ϵ and $\tilde{r}$, where ϵ is the potential minimum and where $V(\tilde{r} = 1) = 0$ holds.

An even shorter range of attractive interactions occurs in colloidal systems. Here, the attractive interaction between two colloidal particles typically originates from depletion forces induced by solvent particles. The range of the resulting attractive interaction is determined by the size of the solvent molecules, which can be orders of magnitude smaller than the size of the colloidal particles themselves [141]. The colloidal potential $V_{colloid}(r)$ depends on the radius of the colloids $R_{colloid}$ and the radius of the solvent particles $R_{solvent}$. The attractive part of the potential can be described by the Asakura-

Oosawa-Potential [142, 143]

$$V_{colloid}(r) = \begin{cases} \infty & r < 2R_{colloid} \\ -C \cdot \epsilon_{colloid} \cdot \left(1 - \frac{3}{4}\frac{r}{R_B} + \frac{1}{16}\left(\frac{r}{R_B}\right)^3\right) & 2R_{colloid} \leq r < 2R_B \\ 0 & r \geq 2R_B \end{cases} \tag{2.20}$$

with $R_B = R_{colloid} + R_{solvent}$.

To illustrate the different attraction ranges, the interaction potentials for atoms (here Argon), C_{60} and colloids (with solvent particles with a radius of $0.2R_{colloids}$) are depicted in Figure 2.8. Usually, the radius of the solvent particles are smaller leading to an even shorter range of interactions for colloids [144]. C_{60} has an intermediate range of attractive interactions, in between those of atomic and colloidal systems.

2.3.2 The organic semiconductor PTCDI-C_8

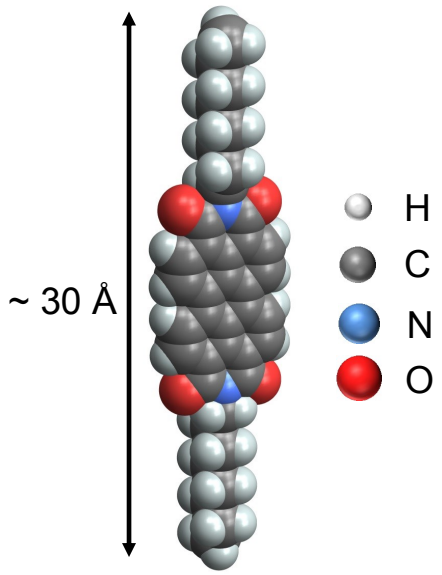

Figure 2.9: PTCDI-C_8 illustration. PTCDI-C_8 ($C_{40}H_{42}O_4N_2$) consists of two octyl chains and a PTCDI backbone.

PTCDI-C_8 (N,N'-dioctyl-3,4,9,10-perylene tetracarboxylic diimide) is a perylene derivative with the chemical formula $C_{40}H_{42}O_4N_2$. The molecule consists of a planar PTCDI backbone and two octyl chains. In recent years perylene diimides have been identified as promising n-type organic semiconductors with reasonable charge carrier mobilities [12, 145, 146]. PTCDI-C_8 has a charge carrier mobility of up to 1.7 cm^2/Vs and is

used in Organic Field-Effect transistors (OFETs) [16, 30, 147] and in organic photovoltaic devices [148]. Highly crystalline thin films on SiO_2 [149] and on sapphire [81] has been observed using *ex situ* x-ray scattering and atomic force microscopy. PTCDI-C_8 crystallizes in a primitive triclinic structure. In Table 2.1 the unit cell parameters for PTCDI-C_8 on sapphire [81] and PTCDI-C_8 crystalline needles [16] are summarized.

	a	b	c	α	β	γ
PTCDI-C_8 on sapphire [81]	9.00 Å	4.89 Å	21.65 Å	85.00°	100.70°	67.20°
PTCDI-C_8 needles [16]	8.50 Å	4.68 Å	19.72 Å	91.57°	94.01°	82.79°

Table 2.1: Reported unit cell parameters for PTCDI-C_8 .

In this thesis the impact of temperature on the molecular packing and the rotational degrees of freedom of PTCDI-C_8 are deduced from x-ray diffraction experiments. Furthermore, the intermolecular interaction within the molecular solid is discussed.

The C_{60} and PTCDI-C_8 molecules used in the framework of this thesis were brought from Sigma-Aldrich (purity > 99.5 %).

2.3.3 Substrates

Mica

In this thesis the muscovite mica is used as a substrate for the growth of the fullerene C_{60} . Mica is a crystalline mineral associated with the chemical formula $KAl_3Si_3O_{12}H_2$. The layer structure of mica is shown in Figure 2.10a [150]. As the bonding of the potassium ions and the adjacent aluminosilicate layers is weak an easy cleavage of mica in the (001)-direction is possible.

The cleavage, done either with scotch tape or with the help of a scalpel, results in large atomically flat surfaces. After cleavage part of the potassium ions are still present on the surface [150]. The surface shows a hexagonal arrangement of SiO_4 tetrahedrons after the cleavage (see Figure 2.10b), which is well suited for the growth of hexagonal close-packed C_{60} moelcules.

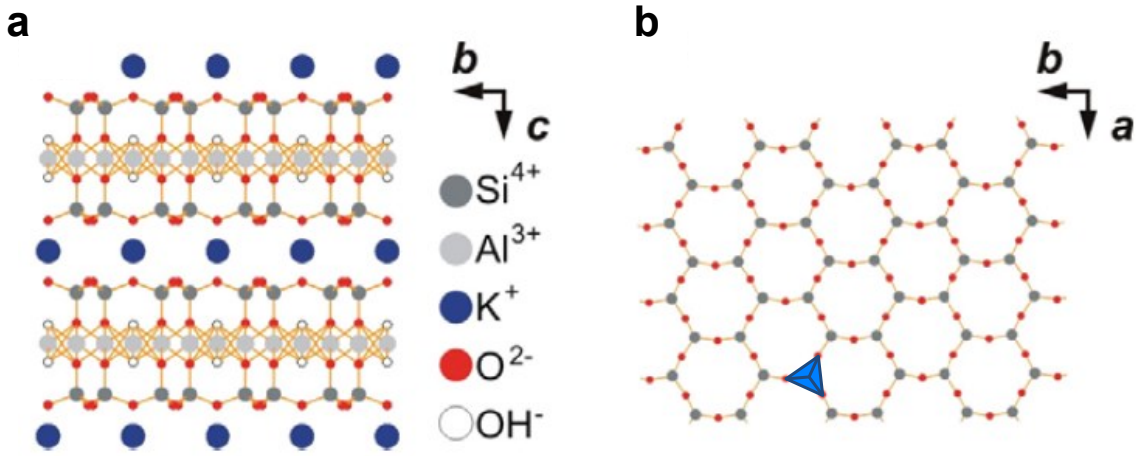

Figure 2.10: The muscovite mica. (a) Layer structure of mica and (b) hexagonal arrangement of SiO_4 tetrahedrons (in blue). The image was taken from [150] (Copyright IOP Publishing).

Silicon(100) with native oxide

For the experiments on the PTCDI-C_8 thin films the molecules were grown *in situ* and *ex situ* on smooth silicon(100) wafers with native oxide on a surface. The growth of an organic semiconductor is strongly influenced by surface contamination. Therefore the silicon wafers were cleaned in high purity and low residue acetone and isopropanol under sonication at a temperature of 40°C to 50 °C. Afterwards a treatment in ultra-pure water in the ultrasonic bath followed. The water residua were removed by nitrogen flow.

Both the freshly cleaved mica and the cleaned silicon wafer were degassed in a UHV chamber for at least four hours at a temperature of 400°C to 500°C at a base pressure of 10^{-8} mbar. The growth experiments of C_{60} on mica as well as PTCDI-C_8 on SiO_2 were performed repeatedly on the same substrate after heating it up to 500°C, resulting in a clean substrate, as confirmed by specular and diffuse x-ray scattering before every growth run.

2.4 Organic Molecular Beam Deposition (OMBD)-System

For the *in situ* and *ex situ* growth experiments performed in the framework of this thesis a portable ultra-high vacuum (UHV) chamber, shown in Figure 2.11, was used. The

UHV chamber is especially designed for organic molecular beam deposition (OMBD) in combination with real-time x-ray experiments. A Beryllium window is used for a x-ray access as Beryllium is highly transparent for x-rays. Additionally, the chamber is equipped with home-built effusion cells for the thermal deposition of molecules.

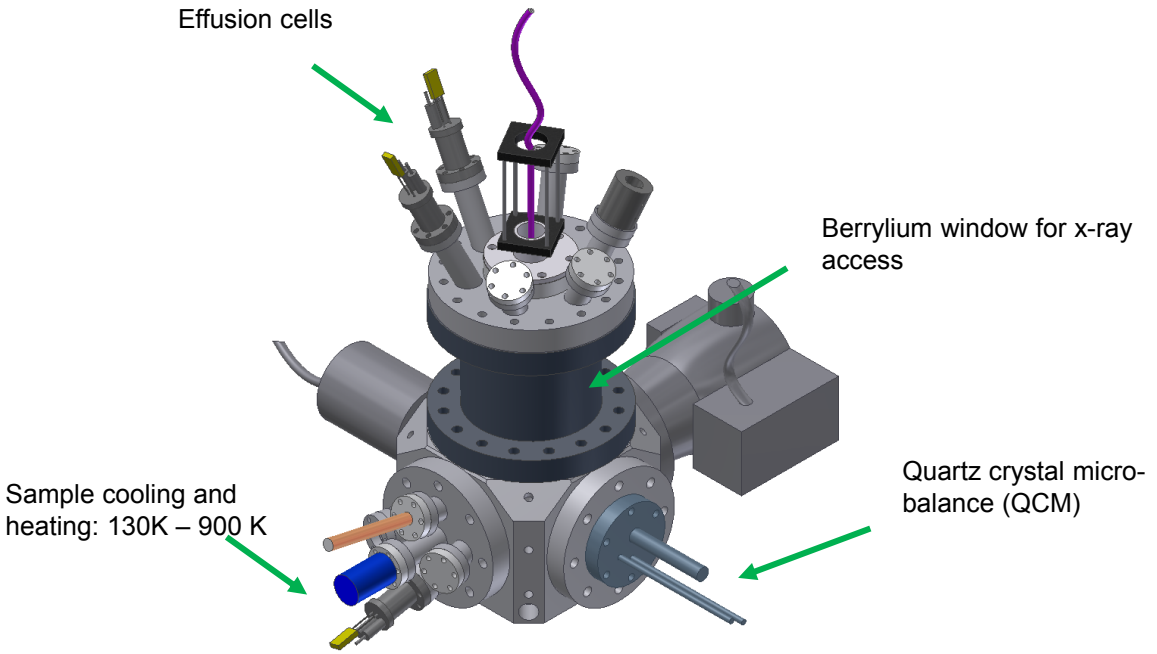

Figure 2.11: Portable UHV system for Organic Molecular Beam Deposition (OMBD). The chamber is equipped with all features to perform *in situ* growth studies on organic thin films.

For varying the molecular flux the sublimation temperature of the cells are varied; typical evaporation temperatures are 305 °C for C_{60} and 285 °C for PTCDI-C_8 . To measure the molecular flux and, respectively, the thin film thickness a quartz crystal micro-balance (QCM) is used. For varying the surface diffusivity of the molecules during growth, the sample temperature can be adjusted in a range from 130 K to 900 K with an uncertainty of approx. $\pm$ 5 K. For the temperature measurements of the sample holder as well as of the effusion cells a K-type thermocouple is used. The pumping system of the chamber consists of a roughening and turbo pump. The growth of the organic thin films was performed at a base pressure of 10^{-8} mbar.

3 Revealing structural properties of organic thin films

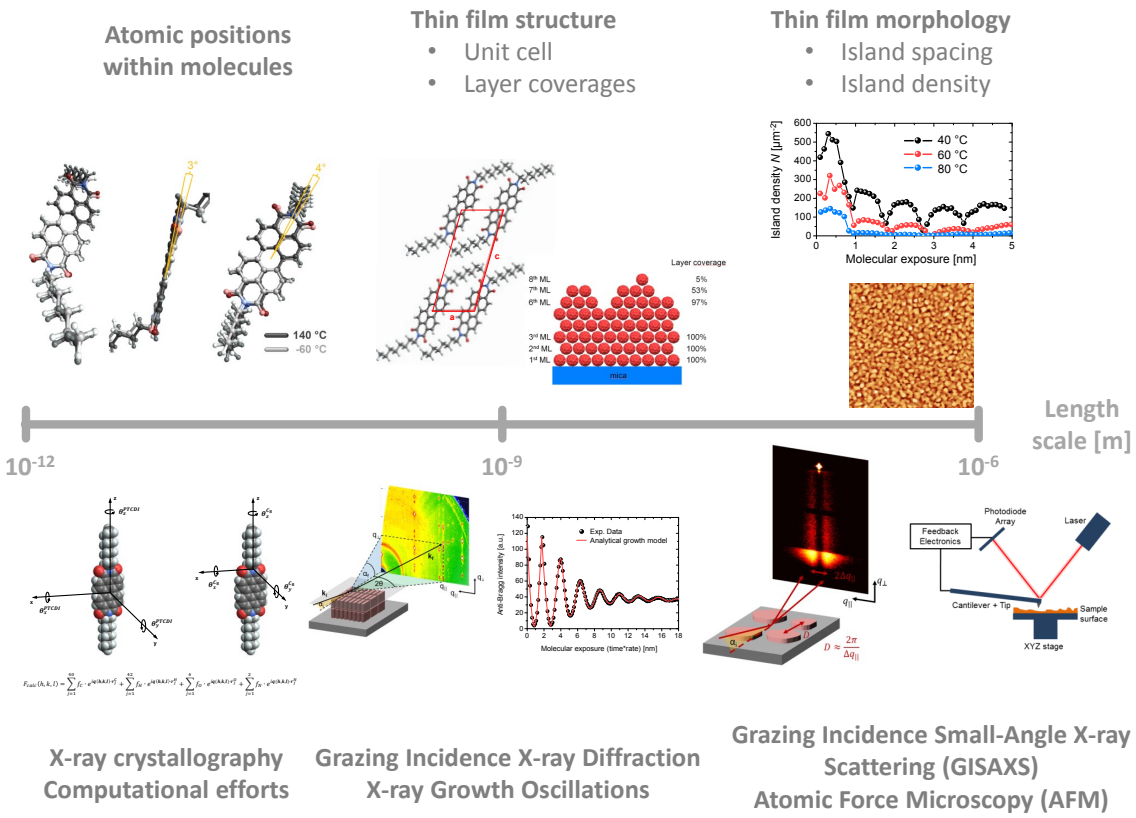

Figure 3.1: Overview of results and associated experimental methods used in this thesis. Upper row: Experimental findings as a function of length scale. Lower row: Experimental methods related to the aforementioned findings.

The functional properties of advanced materials depend on their crystallinity and morphology. Surface-sensitive x-ray scattering is a powerful tool to explore the structural properties of advanced materials with high temporal and spatial resolution. For example, x-ray scattering contributed to a better understanding of catalytic reactions on the surface [59, 60, 151] and the formation of organic heterostructures [11, 152].

In this thesis different experimental methods based on x-ray scattering are used to reveal the structural properties of organic thin films. The methods span a wide range of length scales from thin film morphology on µm-length scale to the nanoscale for surface crystal structure and layer coverages (see the upper row in Figure 3.1). Efforts have been made to approach an even smaller length scale, in particular to quantify the atomic positions within a molecule. In the lower row in Figure 3.1 the experimental methods are shown, which will be introduced in this chapter. The goal of this chapter is not a full review of the techniques used- we give references for further reading for this- but rather to give a brief overview.

This chapter is organized as follows: Firstly, a brief introduction into the theoretical basics of x-rays including the interaction of x-rays with matter and the refraction and reflection of x-rays is given. A section about x-ray reflectivity (XRR) and x-ray growth oscillations follows. Afterwards, a section about Grazing Incidence X-ray Scattering (GIXD and GISAXS) shows the possibilities to gain information on the surface crystal structure but also on the thin film morphology from these reciprocal space techniques. Finally, Atomic Force Microscopy (AFM) as a real-space method to image the morphology is introduced.

3.1 X-ray scattering

X-rays are electromagnetic waves with a wavelength in the angstroem (10^{-10} m) region and therefore in the size of an atom. The electro(-magnetic) waves can be described by a linearly polarized, plane wave $\boldsymbol{E}(\boldsymbol{r}, t)$:

$$\boldsymbol{E}(\boldsymbol{r}) \quad = \quad \boldsymbol{E}_0 \exp(i\boldsymbol{k} \cdot \boldsymbol{r}) \tag{3.1}$$

with the polarization vector $\boldsymbol{E}_0$ and the wavevector along the propagation direction $\boldsymbol{k}$ with the wavenumber $|\boldsymbol{k}| = 2\pi/\lambda$ characterized by the wavelength λ. The scattering of the x-rays with matter is characterized by an incident momentum for the incoming wave $\boldsymbol{k_i}$ and the outgoing momentum $\boldsymbol{k_f}$. At this point it is useful to introduce the momentum transfer defined as $\boldsymbol{q} = \boldsymbol{k_f} - \boldsymbol{k_i}$, which is essential for the description of x-ray scattering experiments.

In the following section the required theory will be explained, which is necessary to interpret and understand the experimental data presented in the this thesis.

3.1.1 Interaction between X-rays and matter

The ability of x-rays to interact with matter can be described on a atomic level by interaction/ scattering lengths. In an atom, x-rays are most strongly scattered by electrons. Scattering with a free electron is quantified in the elastic scattering regime ($|\boldsymbol{k_i}| = |\boldsymbol{k_f}| = 2\pi/\lambda$) by the Thomson scattering length, or the classical electron radius, $r_e = 2.82 \cdot 10^{-5}$ Å.

Interaction with an atom For the interaction of x-rays with an atom a scattered radiation field has to be considered, which is the superposition of all contributions of small volume elements of the charge distribution $\rho_{el}(\boldsymbol{r})$ of the atom. More precisely, a volume element $d\boldsymbol{r}$ at $\boldsymbol{r}$ contribute with $\rho_{el}(\boldsymbol{r})d\boldsymbol{r}$ to the entire scattered radiation field resulting in the following scattering length of an atom in single scattering approximation:

$$-r_e f_0(\boldsymbol{q}) = -r_e \int \rho_{el}(\boldsymbol{r})\ exp(i\boldsymbol{q}\cdot\boldsymbol{r})\ d\boldsymbol{r}. \tag{3.2}$$

For the summation of the different volume elements a phase factor $\boldsymbol{q}\cdot\boldsymbol{r} = (\boldsymbol{k_f} - \boldsymbol{k_i})\cdot\boldsymbol{r}$ has to be considered, which takes the different volume element positions into account.

In the kinetic approximation $f_0(\boldsymbol{q})$ is the Fourier transform of the electron density $\rho_{el}(\boldsymbol{r})$ and is also denoted as atomic form factor for atoms with free electrons. For atoms with bonded electrons dispersion and absorption effects play a role and the energy dependent dispersion correction terms f' and f'' have to be included [153–155]:

$$f(\boldsymbol{q}, E) = f^0(\boldsymbol{q}) + f'(E) + if''(E). \tag{3.3}$$

The atomic form factor for free electrons $f^0(\boldsymbol{q})$ can be analytically described by the following formula [156]:

$$f^0(\boldsymbol{q}) = \sum_{j=1}^{4} a_j e^{-b_j q^2} + c_0 \tag{3.4}$$

with a_i,b_i and c_0 as fitting parameters known for most of atoms. These parameters can be found in the International Tables of Crystallography. The dispersion correction terms f' and f'' can be derived/ extracted from reference [157].

Interaction with a molecule For the characterization and description of the scattering of x-rays with a molecule the molecular structure factor $F_{mol}(\boldsymbol{q})$ is the key quantity to

consider. This is calculated via the summation of the atomic form factors of all atoms j at the position $\boldsymbol{r_j}$ within the molecule:

$$F_{mol}(\boldsymbol{q}) = \sum_j f_j(\boldsymbol{q}) e^{i\boldsymbol{q}\cdot\boldsymbol{r_j}}. \tag{3.5}$$

Now it is possible to derive the atomic positions $\boldsymbol{r_j}$ from an experimental measure of $|F_{mol}(\boldsymbol{q})|^2$ to get information about, e.g., the rotational degrees of freedom of an molecule. The molecular structure factor can be determined in a sufficient way if the molecules are arranged in a highly crystalline structure.

Interaction with crystalline materials Crystalline materials are periodic in space and x-rays penetrating the material get diffracted at the periodic planes. The diffraction is described by Bragg's law

$$m\lambda = 2dsin(\theta) \tag{3.6}$$

where m is an integer. This condition means that constructive interference takes place for electromagnetic waves, which have an incidence angle of θ with respect to periodic lattice planes separated by a distance d.

For a quantitative description of the diffracted x-rays the crystal lattice and the scattering ability of the molecules within the crystal unit cell have to be considered. For the quantification of the unit cell structure factor, all molecules m at position r_m within one unit cell have to be summed up

$$F^{unitcell}(\boldsymbol{q}) = \sum_m F^m_{mol}(\boldsymbol{q}) e^{i\boldsymbol{q}\cdot\boldsymbol{r_m}}. \tag{3.7}$$

The crystal lattice is now defined by a translation vector $\boldsymbol{R_n} = n_1\boldsymbol{a} + n_2\boldsymbol{b} + n_3\boldsymbol{c}$ with $\boldsymbol{a}$, $\boldsymbol{b}$ and $\boldsymbol{c}$ being the basis vectors of the lattice. From $\boldsymbol{R_n}$ and the unit cell structure factor $F^{unitcell}(\boldsymbol{q})$ the structure factor of a crystal can be derived:

$$F^{crystal}(\boldsymbol{q}) = \sum_n F^{unitcell}_n(\boldsymbol{q}) e^{i\boldsymbol{q}\cdot\boldsymbol{R_n}}. \tag{3.8}$$

The diffracted signal of a crystalline material $I^{crystal} \propto \left|F^{crystal}(\boldsymbol{q})\right|^2$ is composed by the lattice sum and the molecular structure factor defining the position and, respectively, the intensity of the Bragg reflections originating from the crystalline material.

Furthermore, it can be seen that

$$\boldsymbol{q} \cdot \boldsymbol{R_n} = 2\pi \cdot integer \tag{3.9}$$

and the unique solution of this equation can be found with the help of the useful reciprocal lattice, which is used for the description of a crystal. The reciprocal lattice basis $\boldsymbol{a}^*, \boldsymbol{b}^*$ and $\boldsymbol{c}^*$ can be calculated from the basis vectors of the realspace lattice $\boldsymbol{a}, \boldsymbol{b}$ and $\boldsymbol{c}$ [153]. Therefore, a reciprocal lattice vector $\boldsymbol{G}(h,k,l)$ can be introduced:

$$\boldsymbol{G}(h,k,l) = h \cdot \boldsymbol{a}^* + k \cdot \boldsymbol{b}^* + l \cdot \boldsymbol{c}^*. \tag{3.10}$$

$\boldsymbol{G}(h,k,l)$ is located perpendicular to the lattice plane (h,k,l) in the crystal. The triple (h,k,l) denotes the *Miller indices*. Furthermore, one can show, that the unique solution for 3.9 is

$$\boldsymbol{q} = \boldsymbol{G}(h,k,l) \tag{3.11}$$

, which denotes the *Laue condition*. This means, that $F^{crystal}(\boldsymbol{q})$ is only unequal *zero* if $\boldsymbol{q}$ is equals a reciprocal lattice vector $\boldsymbol{G}(h,k,l)$.

Reflection and refraction of x-rays at interfaces So far, the interaction of x-rays with matter on a atomic level has been discussed and will now be expanded to the reflection and refraction of the electromagnetic waves at interfaces. These processes are described by the refractive index of the different media at the interface. For a homogenous medium the refractive index is complex and is quantified by a dispersive part δ and a absorptive part β:

$$n = 1 - \delta + i\beta. \tag{3.12}$$

In particular the part describing the dispersion and the absorption of the media is defined as follows [153]:

$$\delta = \frac{\lambda^2}{2\pi} r_e \rho_{el} \tag{3.13}$$

$$\beta = \frac{\lambda}{4\pi} \mu \tag{3.14}$$

The dispersive part directly connects the refractive index with the scattering properties of the materials, the electron density ρ_{el} and the scattering length of an electron r_e. λ is the wavelength of the x-ray radiation. For β describing the absorption μ denotes the absorption coefficient.

For x-ray radiation δ is positive and has values from 10^{-6} to 10^{-5}. The values for β are even smaller. Therefore, the refractive index for x-rays is always below 1, which has important consequences for the reflection and refraction at interfaces as we will see in the following sections dealing with details on scattering geometries used in this thesis.

For further reading on scattering theory and the mathematical description of x-ray scattering the reader is referred to [153].

3.1.2 X-ray reflectivity (XRR)

In Figure 3.2a the scattering geometry for x-ray reflectivity (XRR) measurements is shown. The incoming x-rays with a wave vector $\boldsymbol{k_i}$ impinge the surface under an incident angle α_i and are reflected with an angle α_f. The reflected x-rays are characterized by an wave vector $\boldsymbol{k_f}$. Consequently, XRR measurements are characterized by the following elements:

- Elastic scattering is considered: $|\boldsymbol{k_i}| = |\boldsymbol{k_f}| = \frac{2\pi}{\lambda}$
- The resulting transfer momentum or scattering vector $\boldsymbol{q_\perp} = \boldsymbol{k_f} - \boldsymbol{k_i}$ only has a component perpendicular to the surface as the x-rays are specular reflected (incident angle α_i equals the outgoing angle α_f, $\alpha = \alpha_i = \alpha_f$)
- Furthermore, XRR measurements are performed monitoring the reflected intensity by either a point or a $2D$ detector, while scanning the incident and outgoing angle in a $\alpha - 2\alpha$ geometry, also called *Bragg-Brentano* configuration [158].
- Consequently, XRR measurements are displayed as a function of the length of the scattering vector $\boldsymbol{q_\perp}$, which can now be expressed in terms of the wavelength λ and the scattering angle α: $|\boldsymbol{q_\perp}| = \frac{4\pi}{\lambda} sin(\alpha)$

The exact shape and characteristics of the XRR measurements and the information extracted from it depend on the structural properties of investigated material and will be described in the following in more detail.

XRR of a smooth surface

Figure 3.2a shows the standard geometry of a XRR measurement using the example of a perfectly smooth vacuum/ substrate interface and Figure 3.2b shows the corresponding XRR measurement. To understand the shape/ characteristics of this XRR measurement the fundamental reflection and refraction properties of the x-rays have to be considered. As a consequence of an refractive index for x-rays lower than one an critical scattering vector q_c can be derived, below which total external reflection, and thus a constant reflectivity of almost 100%, occurs:

$$\begin{aligned} q_c &= \frac{4\pi}{\lambda} sin(\alpha_c) \\ \text{with } \alpha_c &= \sqrt{2\delta} = \lambda\sqrt{\frac{\rho_{el} r_e}{\pi}} \end{aligned} \tag{3.15}$$

Therefore, the position of the critical edge gives information on the electron density ρ_{el} of the material at the interface. For $q_\perp > q_c$ a fast decay of the reflectivity R is observed. From the *Fresnel equations* a dependence of R on q can be extracted to be $R \propto 1/q_\perp^4$ for this $q_\perp$-regime.

XRR of a homogeneous thin film

As a next step one can regard an additional (non-crystalline) flat layer on top of the substrate as it is shown in Figure 3.2c. In this case a system with two interfaces, the vacuum/ thin film- interface as well as the thin film/ substrate interface, arise. Interference of the x-rays reflected at the vacuum/ film interface and at the film/ substrate interface leads to the appearance of periodic oscillations, also called *Kiessig fringes*, in the XRR measurement of such a film in Figure 3.2d. From the width of these fringes $\Delta q_\perp$ (distance between minima) the thickness of the thin film D can directly be quantified using $D = 2\pi/\Delta q_\perp$.

XRR of a multi-layer film

In the previous case the XRR signal from a thin film with homogenous electron density has been discussed. A periodic variation of electron density within the film in terms of a multi-layer structure (see Figure 3.2e) leads to a further characteristic of the XRR signal as shown in Figure 3.2f. Maxima appear at the momentum transfer q_0 in the reflected

intensity, called Bragg-reflections, due to the periodicity of the thin film electron density if Bragg's law (see equation 3.6) is fulfilled.

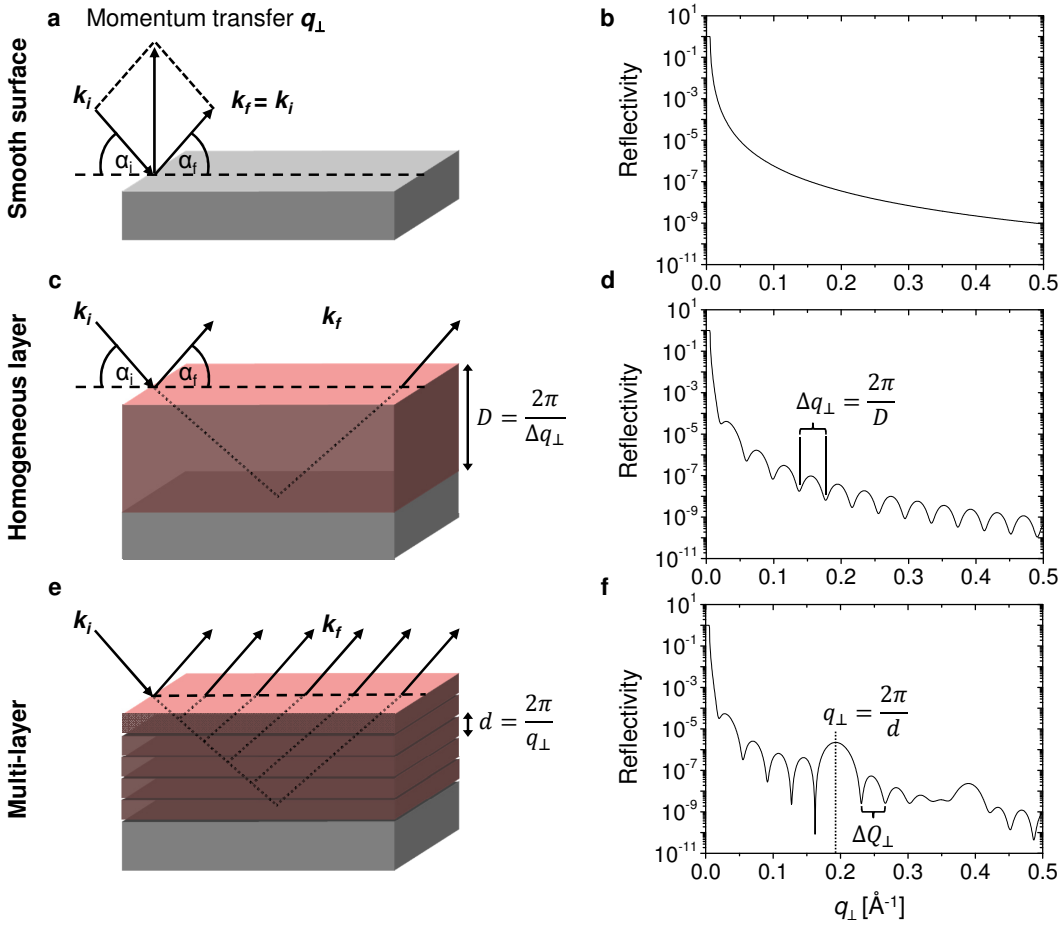

Figure 3.2: X-ray reflectivity (XRR) for different interfaces. (a)+(b) smooth surface, (c)+(d) homogeneous layer and (e)+(f) multilayer material system.

The position of the Bragg-reflection q_0 gives information on the inter-layer distance $d = 2\pi/q_0$. Additionally, side-maxima appear on the left and right side of the Bragg-reflection which are called *Laue oscillations*. These oscillations stem from the thickness of the thin film. The number of oscillations corresponds to the number of coherently scattering layers as the intensity of each layer is coherently summed up resulting in $(n + 1)$-layers for n oscillations. Therefore, the size of the coherently ordered domain $\Delta D = 2\pi/\Delta Q_\perp$ can be estimated from the width of these oscillations $\Delta Q_\perp$.

Influence of thin film roughness on x-ray reflectivity

In the previous paragraphs a perfectly smooth thin film was assumed to describe the information and effects which can be gained from XRR measurements. For a rough thin film less x-rays are reflected specularly but also diffusely as it is shown in Figure 3.3a.

The *Kiessig fringes* are smeared out and the number of fringes decreases with increasing surface roughness as can be seen in Figure 3.3b.

However, the diffuse scattering also contains a lot of useful information about the thin film nanostructure as will be shown in section 3.1.4.3.

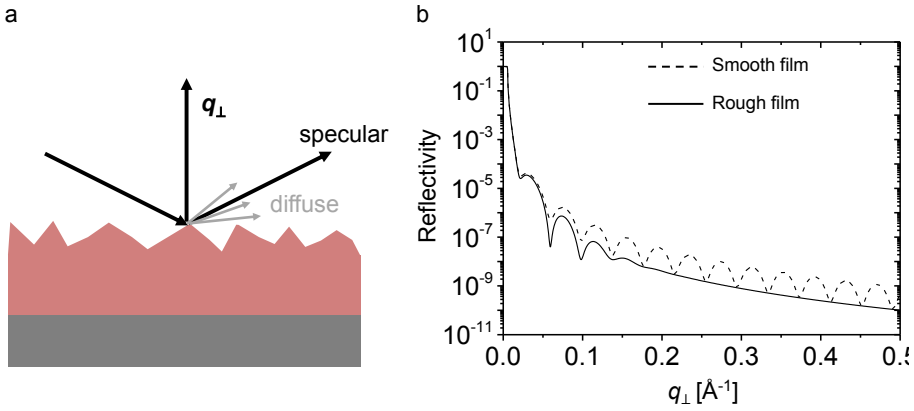

Figure 3.3: Influence of the surface roughness on the XRR intensity. For increasing roughness more X-rays are scattered diffusely.

Modeling XRR measurements

For revealing detailed structural information like surface/ interfacial roughness as well as (layer) thicknesses for, e.g. layered structures as shown in Figure 3.2f the exact characteristic of x-ray reflectivity measurements displayed by Kiessig fringes as well as the Bragg reflections/ Laue oscillations have to be fitted by dedicated models of the electron density.

Kinematic approximation The simplest model for x-ray reflectivity can be derived in so called kinematic approximation assuming the scattering to be weak compared to the incident beam intensity and neglecting multiple scattering events, which means that a x-ray photon is scattered only once. For modeling XRR this approximation holds only for weak reflectivity $q_\perp \gg q_c$. The approximation of single-scattering events enables us to simply sum up the scattering amplitudes from each individual layer n (represented by the corresponding atomic/ molecular form factor) taking the different pathways into account by including a phase factor (see also equation 3.5). The reflected intensity of a n-layer system $I_{reflected}$, each layer separated by a spacing d_{layer} is then given by

$$I_{reflected}(q_\perp) = \left| \sum_n f(q) e^{i \cdot q_\perp \cdot n \cdot d_{layer}} \right|^2 \tag{3.16}$$

with n the number of crystalline layer, $q_\perp$ the momentum transfer and d_{layer} the thickness of one crystalline layer.

Dynamical theory: Parratt formalism A common formalism for modeling XRR measurements for a broad $q_\perp$-range is the *Parratt formalism*. In this model, the thin film is devided into N layers individually described by an refractive index n_j, a constant electron density $\rho_{el,j}$ and their interfaces. With such a model of electron density the reflected x-ray intensity has to be calculated and to be fitted on the experimental data. In the Parratt formalism the reflectivity of each layer with two interfaces is recursively calculated using the *Fresnel equations* beginning with the N^{th} layer on top of the substrate and ending up with the very 1^{st}. For including layer roughness an exponential damping term or (many) small boxes between the layers can be introduced to smear out the electron density profile between adjacent layers.

A detailed description of the formalisms for modeling XRR measurements can be found in [153].

3.1.3 Anti-Bragg growth oscillations during organic thin film growth

Generally, scattering techniques like reflection high energy electron diffraction (RHEED), helium scattering and x-ray scattering are well suited for the investigation of growth processes in real-time and *in situ* as they are *non-invasive*. X-ray (specular) growth oscillations, i.e. periodic oscillations of the specular x-ray reflectivity over the deposition time, are an import tool for the investigation and characterization of the self-assembly of crystalline materials [42, 100, 110–112, 159]. The cause of the temporal modulations of the x-ray intensity are reflections from consecutive layers which alternately interfere destructively and constructively as shown in Figure 3.4a.

The evolution of the oscillations provides information about the layer nucleation and filling as well as about the film roughening. The origin of the appearance of x-ray growth oscillations is different from the effects leading to growth oscillations in RHEED and helium scattering. Due to the low penetration depth/ large scattering cross-section of electrons and helium atoms these techniques are mainly sensitive to the top-surface structure, contrary to x-rays, which are able to penetrate the entire thin film. Consequently, reflections at lattice planes and interfaces contribute to x-ray growth oscillations. For RHEED and helium scattering the film roughness during layer-by-layer growth, which is smooth for completely filled and rough for half filled monolayers, determines the evolution of growth oscillations with a period of one monolayer. However, x-ray growth oscillations have an oscillation period of two monolayers as the x-rays are reflected from consecutive layers and alternately interfere destructively.

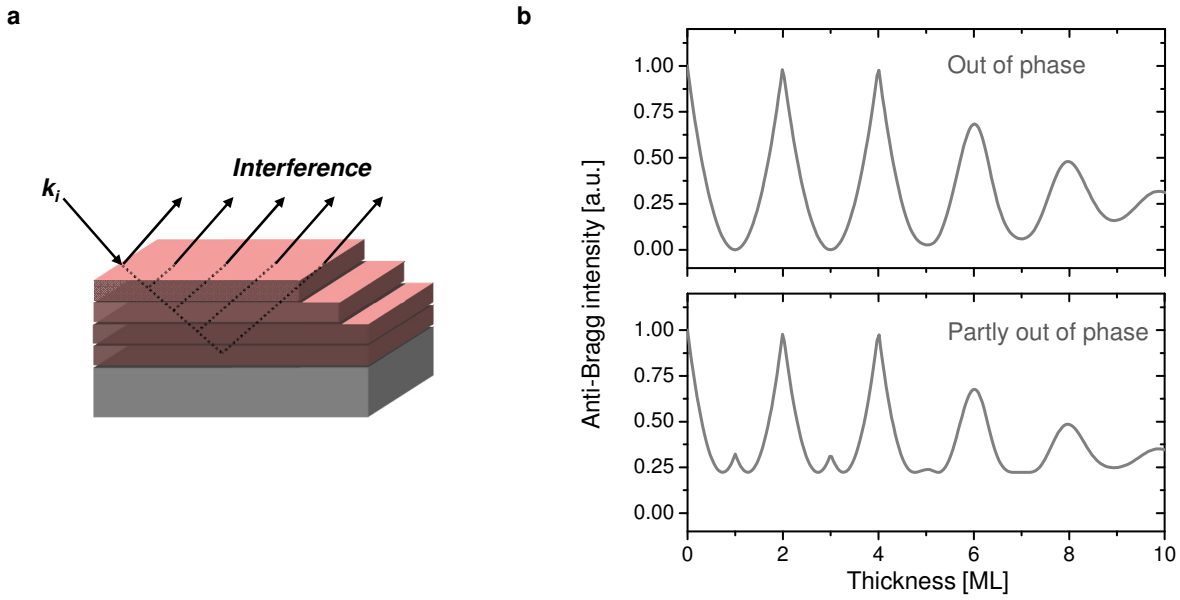

Figure 3.4: X-ray growth oscillations. (a) X-rays are reflected from consecutive layers and alternately interfere destructively and constructively causing the observed temporal evolution. (b) Typical anti-Bragg growth oscillations for two different phases between substrate and ad-layers.

To quantify the evolution of growth the x-ray growth oscillations can be modeled in the kinematic approximation by a summation of the different scattering amplitudes for each crystalline layer n, which is given by the molecular form factor F_{mol} and the layer coverage of the respective layer θ_n, and the substrate. For both a phase factor has to be considered, which results in the following reflected intensity of growing crystalline films at the anti-Bragg point $q_z = q_{Anti-Bragg} = q_{Bragg}/2$:

$$I_{anti-Bragg}(q_z = q_{anti-Bragg}) = \left| A_{sub} e^{i\phi_{sub}} - F_{mol} \sum_n \theta_n(t) e^{i\pi n} \right|^2 . \tag{3.17}$$

A_{sub}	Scattering amplitude of the substrate
ϕ_{sub}	Phase between substrate and ad-layers
F_{mol}	Molecular form factor
n	Layer number
θ_n	Coverage for the n^{th}-layer

For odd and even layer numbers each contribution of the respective layer has an alternating sign, which results in the occurrence of growth oscillations at the anti-Bragg point as shown in Figure 3.4b. For perfect layer-by-layer growth, which means one monolayer

is completely filled before the next layer starts to nucleate, the scattering contribution of odd layers cancel that of even layers. The shape and amplitude of the anti-Bragg growth oscillations are strongly affected by the interference of substrate and film scattering. In Figure 3.4b the anti-Bragg growth oscillations for different phases between substrate and ad-layers are shown. The substrate scattering amplitude A_{sub}, the phase between the substrate and the ad-layers ϕ_{sub} and the molecular form factor F_{mol} can be derived from the maximum intensity at the very beginning of growth, the first minimum of intensity as well as from the saturation level of the growth oscillations [100]. Consequently, the layer coverages $\theta_n(t)$ can be fitted according to analytical growth models presented in section 2.1.1.2, which provides information on the vertical evolution of growth. The intensity damping of the oscillations reflects the onset of slight roughening.

X-ray growth oscillations cannot only be recorded at the anti-Bragg point but also beyond the anti-Bragg conditions [100, 111]. Measurements at optimized q-values could result in larger amplitudes and lower intensity damping during the growth, which allows to model growth processes with rough film morphology.

3.1.4 Grazing Incidence X-ray Scattering

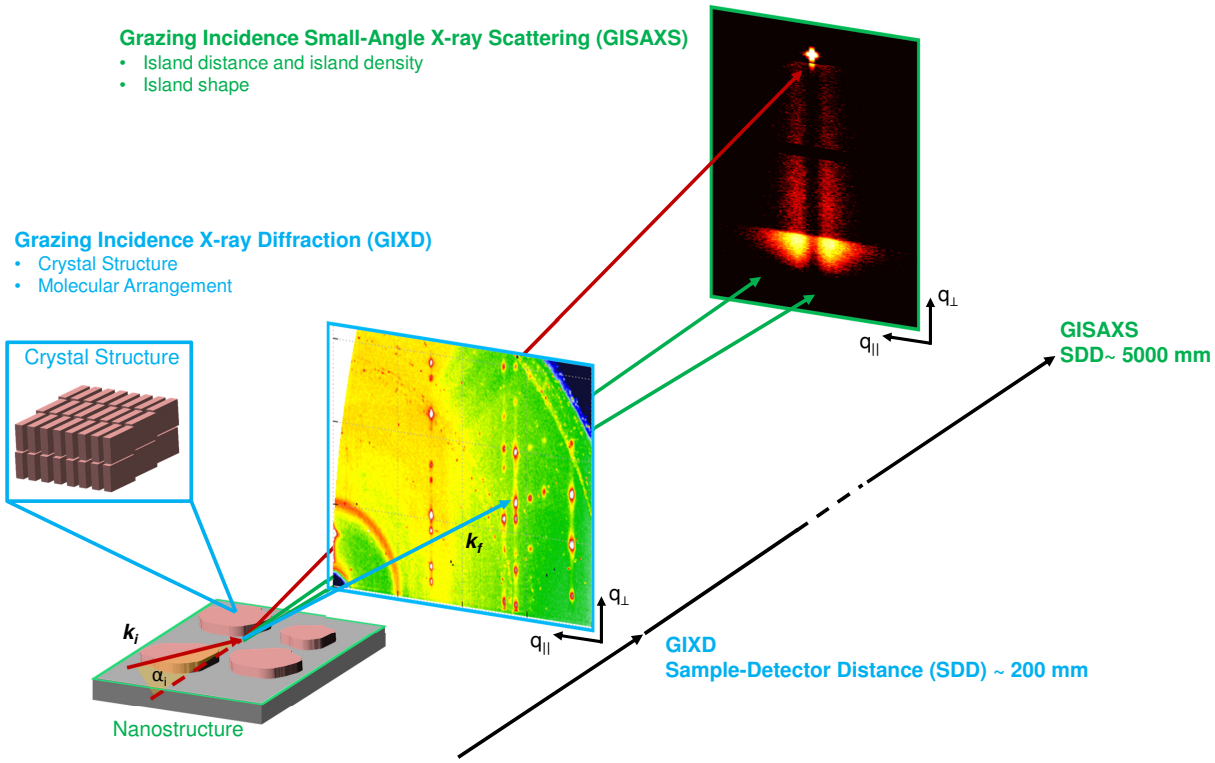

Figure 3.5: Surface sensitive Grazing Incidence X-ray Scattering. Depending on the length scale one aims to investigate one distinguishes between Grazing Incidence Small-Angle X-ray Scattering (GISAXS) and Grazing Incidence X-ray Diffraction (GIXD), which differ in the magnitude of the scattering angle. GIXD enables us to reveal the crystalline thin film structure, while GISAXS allows for quantifying the nanostructure.

3.1.4.1 Basics of Grazing Incidence X-ray Scattering

For incident angles α_i smaller than α_c the z-component of the transmitted wave vector $k_{t,z}$ becomes complex, which gives rise to an evanescent and therefore surface-sensitive x-ray scattering:

$$k_{t,z} \approx k\sqrt{\alpha_i^2 - \alpha_c^2} = ik\sqrt{\alpha_c^2 - \alpha_i^2}. \tag{3.18}$$

The electrical field in z-direction inside the medium can be written as:

$$E \propto exp(ik_{t,z}z) \propto exp(-zk\sqrt{\alpha_c^2 - \alpha_i^2}) = exp(-z\Lambda^{-1}). \tag{3.19}$$

The amplitude of this wave decreases inside the medium with increasing penetration depth Λ. A wave with this properties is called an *evanescent wave*. Consequently, the penetration depth can be varied to increase the surface sensitivity by changing the incident angle α_i. Experiments with x-rays under grazing incidence are called *Grazing Incidence X-ray Scattering*. Depending on the length scale one aims to investigate one distinguishes between Grazing Incidence Small-Angle X-ray Scattering (GISAXS) and Grazing Incidence X-ray Diffraction (GIXD) (or Grazing Incidence Wide-Angle X-ray Scattering (GIWAXS)). See Figure 3.5 for an illustration of both Grazing Incidence X-ray Scattering techniques. Both techniques differ in magnitude of the scattering angle, which enables one to probe different length scales on the surface and is directly connected to different sample-to-detector distances (SDD).

Detailed information on the theoretical aspects of Grazing Incidence X-Ray Scattering can be found in [160, 161].

3.1.4.2 Grazing Incidence X-ray Diffraction (GIXD)

For small SDD in the range of 200 mm large scattering angles, and, therefore small length scales can be probed. This makes GIXD a powerful tool to probe the crystalline structure of thin films [23, 152, 162]. Within this thesis the surface structure of organic materials such as crystal lattice parameters and the molecular packing was obtained by measuring the Bragg reflections as a function of the lateral momentum transfer $q_{||}$.

Additionally, for revealing the 3D structure of organic thin films the vertical momentum transfer $q_\perp$ was recorded in asymmetric geometry ($\alpha_i \neq \alpha_f$) as it is shown in Figure 3.6. For this, the 2D detector image has to be transformed into reciprocal space. Generally, the incoming x-rays with wavelength λ impinge on the surface with an incident angle α_i and are diffracted on the crystalline surface structure featuring an outgoing angle α_f and a lateral scattering angle of 2θ. The three-dimensional scattering vector $\boldsymbol{q}$ can be derived using

$$\boldsymbol{q} = \begin{pmatrix} q_x \\ q_y \\ q_z \end{pmatrix} = \frac{2\pi}{\lambda} \begin{pmatrix} cos(\theta) \cdot cos(\alpha_f) - cos(\alpha_i) \\ sin(\theta) \cdot cos(\alpha_f) \\ sin(\alpha_i) + sin(\alpha_f) \end{pmatrix}, \tag{3.20}$$

which allows the calculation of $q_{||} = \sqrt{q_x^2 + q_y^2}$ and $q_\perp = q_z$.

To shed light on the epitaxial order of organic materials with respect to the substrate surface the sample can be rotated around the surface normal. For organic materials on amorphous substrates such as PTCDI-C_8 on SiO_2 a 2D powder or textured structure has been observed resulting in a random distribution of lateral orientations with a layered structure in vertical direction.

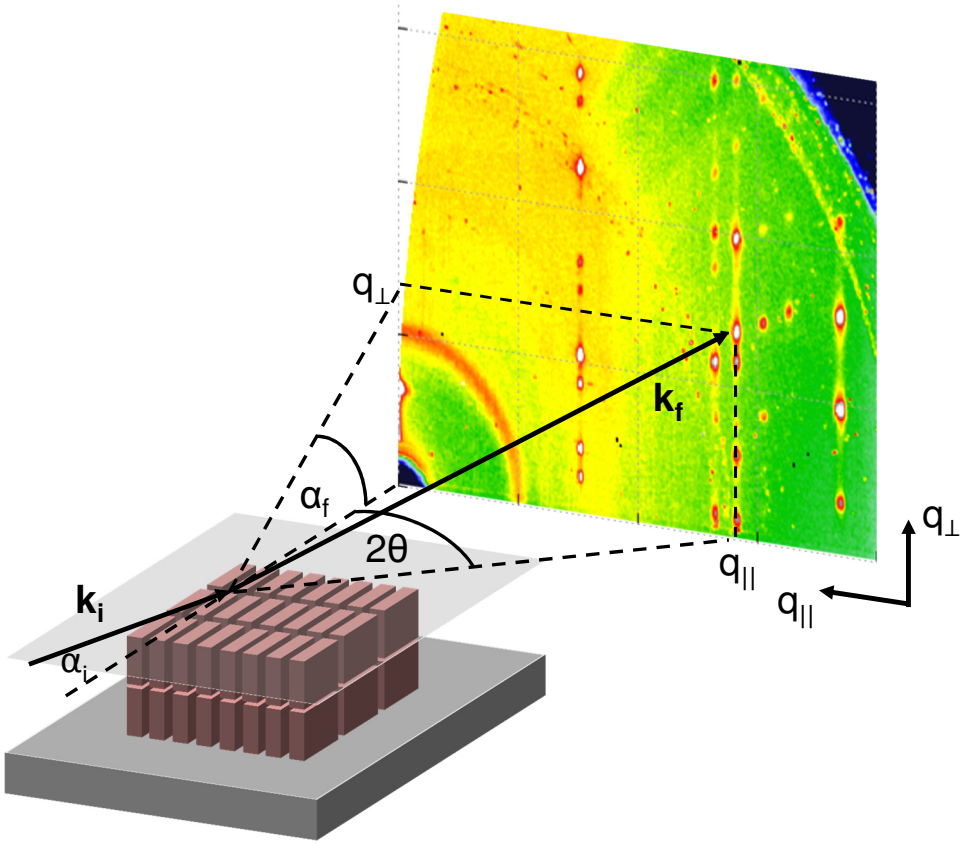

Figure 3.6: Grazing Incidence X-ray Diffraction for revealing the surface crystal structure. 3D surface crystallography gives insights into the crystalline surface structure as well as the molecular arrangement.

The intensity distribution in the reciprocal space is composed of the unit cell structure factor and the molecular structure factor (see 3.8). The positions of the Bragg reflections give rise to the unit cell parameters and the intensity modulation of the reflections is caused by the molecular arrangement.

For obtaining information about the unit cell parameters for PTCDI-C_8 a statistical data processing formalism developed by Linus Pithan at the Humboldt-Universität zu Berlin [163] was used. First, a mask of the Bragg reflections in reciprocal space was produced. The formalism compares calculated positions of Bragg reflections for a set of unit cell parameters with the mask of the experimentally observed diffraction pattern. A

statistical evaluation of the hits as a function of the unit cell parameters gives the unit cell parameters describing the experimental data best.

3.1.4.3 Grazing Incidence Small-Angle X-ray Scattering (GISAXS)

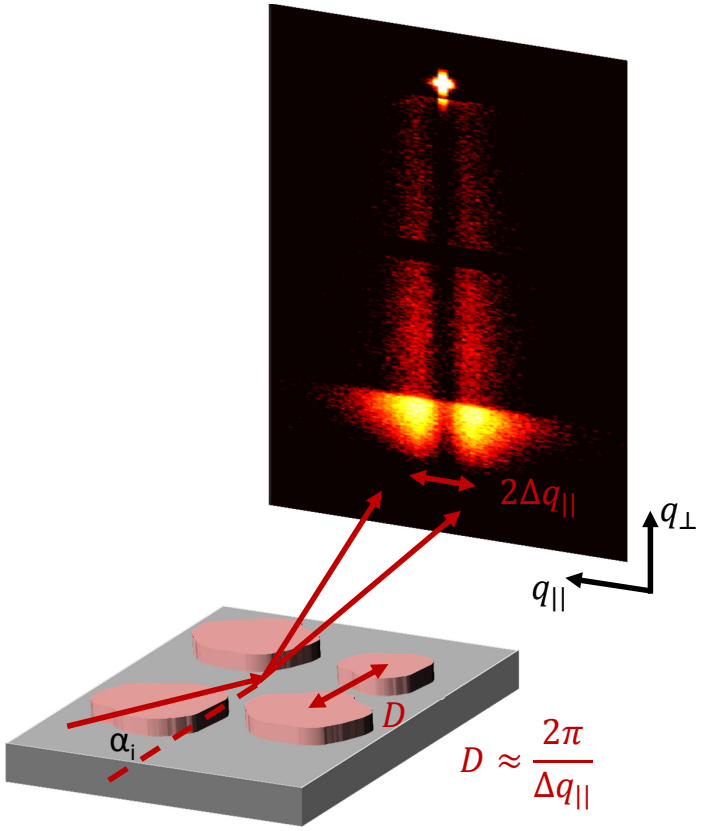

Figure 3.7: GISAXS scattering geometry. GISAXS sheds light on the thin film nanostructure. The average island distance of the nanostructure causes two characteristic maxima in the diffusely scattered intensity along the momentum transfer $q_{||} \approx 2\pi/D$.

Increasing the sample-to-detector distance from approximately 200 mm for GIXD experiments to several meters enables one to investigate the small scattering angles (GISAXS), and therefore to monitor large real-space length scales such as the thin film nanostructure (see Figure 3.7 for the scattering geometry). The scattered GISAXS intensity is composed of the structure factor $S(q_{||}, q_\perp)$ for the nearest-neighbor distance D between islands and the form factor $F(q_{||}, q_\perp)$ for island diameter and island shape. Dedicated programs like *IsGISAXS* [164] or *FitGISAXS* [165] are well suited for modelling the 2D GISAXS scattering pattern in order to deduce island distance, island diameter and island shape. In the framework of this thesis GISAXS is used to follow the evolution of the

nanostructure during growth. In the growth experiments performed the average island distance D causes two characteristic maxima in the diffusely scattered intensity along the momentum transfer $\Delta q_{||} \approx 2\pi/D$ [57, 58] , on which will this thesis focus. To show that this estimation is true, in Figure 3.8 the contribution of structure factor and form factor to the overall GISAXS intensity is shown. For the calculation cylindrical shaped islands with a diameter of 20 nm and the 1D paracrystal model [166] with an nearest-neighbor distance of 100 nm was used. For details on the calculation of GISAXS scattering pattern I refer to references [164, 165, 167] and the references therein.

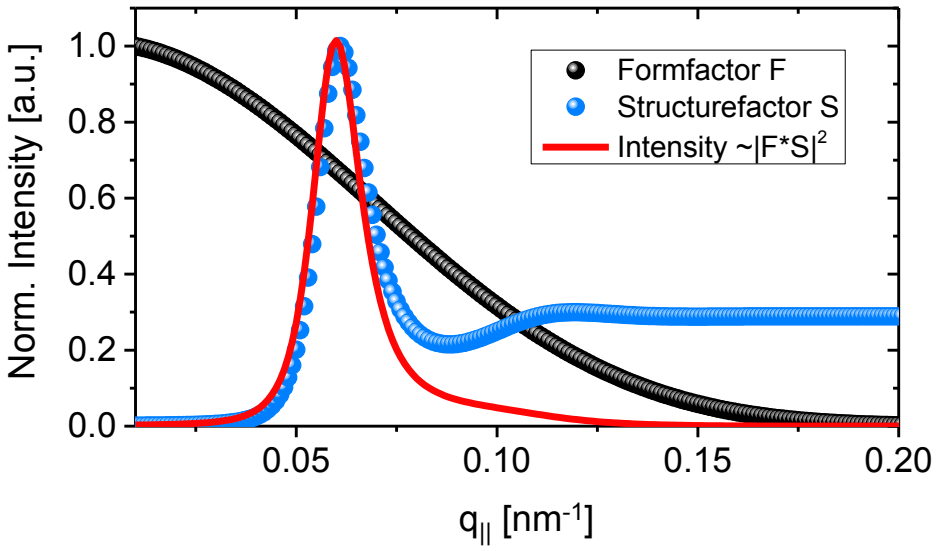

Figure 3.8: Contribution of structure factor S and form factor F to the GISAXS intensity. The scattered GISAXS intensity is composed of the structure factor $S(q_{||}, q_{\perp})$ for the nearest-neighbor distance D between islands and the form factor $F(q_{||}, q_{\perp})$ accounting for the island diameter and their shape.

An additional feature of GISAXS scattering patterns is an increased intensity at the critical angle of the material along $q_{\perp}$. This *Yoneda peak* [168] is due to the intensity enhancement at the surface because of constructive interference between the incoming and outgoing wave at the critical angle.

3.1.5 Beamline P03 at PETRA III

The real-time and *in situ* experiments presented in this thesis have been performed at the Micro- and Nanofocus X-ray Scattering (MiNaXS,P03) beamline [58,169,170] at PETRA III (DESY) in Hamburg. The storage ring PETRA III at DESY in Hamburg is operated at an energy of 6 GeV with an positron beam current of 100 mA. The MiNaXS beamline is a high-brilliance beamline combining low divergence with high photon flux, which allows to perform real-time and *in situ* experiments in Grazing Incidence Small-Angle X-ray Scattering (GISAXS) as well as Grazing Incidence X-ray Diffraction (GIXD) geometry with sufficient temporal and spatial resolution. The optics of the beamline consists of two cryo-cooled silicon (111) crystals, which allow for an energy variation from 8 to 23 keV with an energy resolution of $\Delta E/E \cong 10^{-4}$. Compound refractive lenses (CRL) are used for collimation and focussing resulting in minimal beam sizes of 7 μm in horizontal and 5 μm in vertical direction. In the experiments presented in this thesis a beamsize of about 22 x 18 μm has been used.

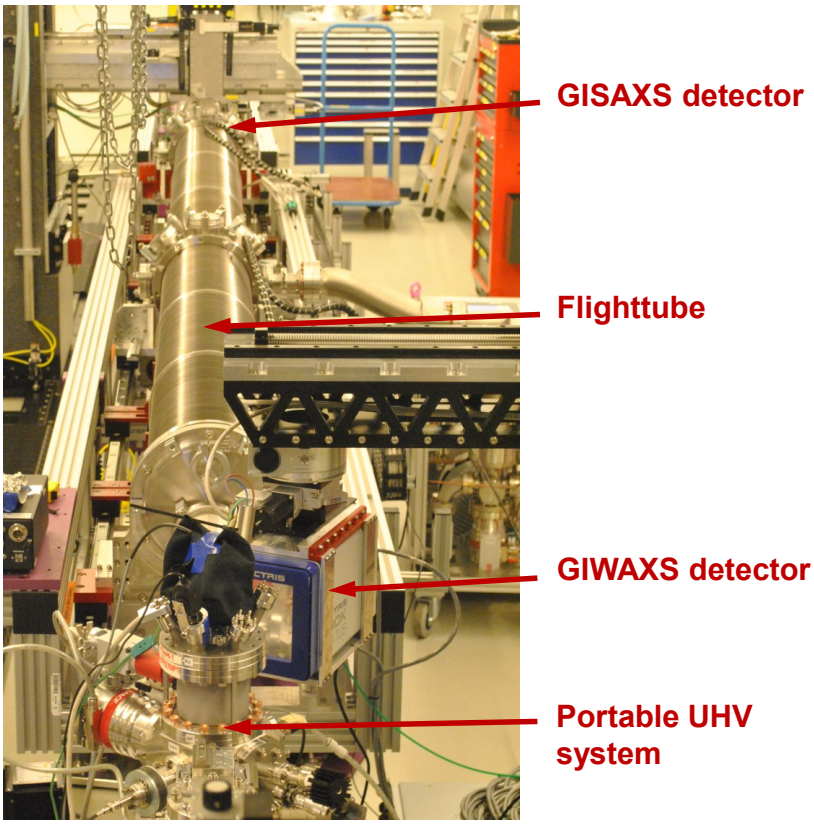

Figure 3.9: Experimental setup at the MiNaXS beamline during the performed experiments.

In Figure 3.9 an image of the beamline during the experiments is shown. Our portable UHV system is mounted on a *Huber* goniometer which has two angular and three trans-

lational degrees of freedom. For the GISAXS experiments a flighttube has been used in order to avoid air scattering. A 2D area detector with a high dynmical range (PILATUS 300K, Dectris) has been used for the GISAXS as well as for the GIXD experiments.

3.1.6 Lab-based x-ray sources

Parts of the x-ray experiments have been carried out at a lab-based rotating Cu anode x-ray system with a comparatively high photon flux of $5 \cdot 10^8$ photons/ s. The widely-used *rotating anode* setup for generating x-rays is schematically shown in Figure 3.10.

Electrons are generated by a thermal emission from a filament and are accelerated towards a water-cooled rotating Cu anode. The incident electron collides with an atom and removes an atomic electron from the inner K-shell. Subsequently, one electron from the outer L-shell relaxes on this created vacancy by generating Cu-Kα radiation corresponding to the energy difference between K- and L-shell (8.05 keV or 1.54 Å).

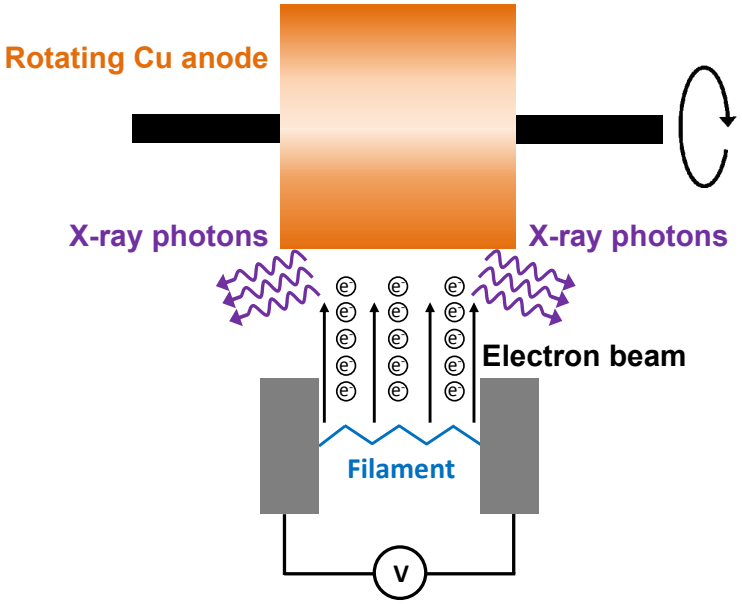

Figure 3.10: Working principle of a rotating anode x-ray source.

The x-ray system is connected to a (3 + 2) axis diffractometer which enables x-ray reflectivity (XRR) as well as Grazing Incidence X-ray Diffraction (GIXD) experiments with a resolution of 0.01 $Å^{-1}$ and 0.01 $Å^{-1}$, respectively. This x-ray system has been used for the investigations on the post-growth dewetting process of C_{60} on mica. Furthermore, the system has been used for *ex situ* measurements, e.g. for revealing the adsorption geometry of C_{60} on mica.

3.2 Atomic-Force Microscopy (AFM)

Scanning probe microscopy techniques are well suited for imaging surface topographies. For characterizing the surface morphology a scanning probe (tip) is moved close to the sample, while measuring characteristic sample-probe interactions. In atomic force microscopy (AFM) experiments the deflection of the cantilever is monitored by a photo diode array with a help of a laser beam. In Figure 3.11 an illustration of the AFM working principle and an image of the cantilever including the tip are shown. The deflection of the cantilever is highly sensitive to surface-tip interactions, which allows for mapping of the surface topography.

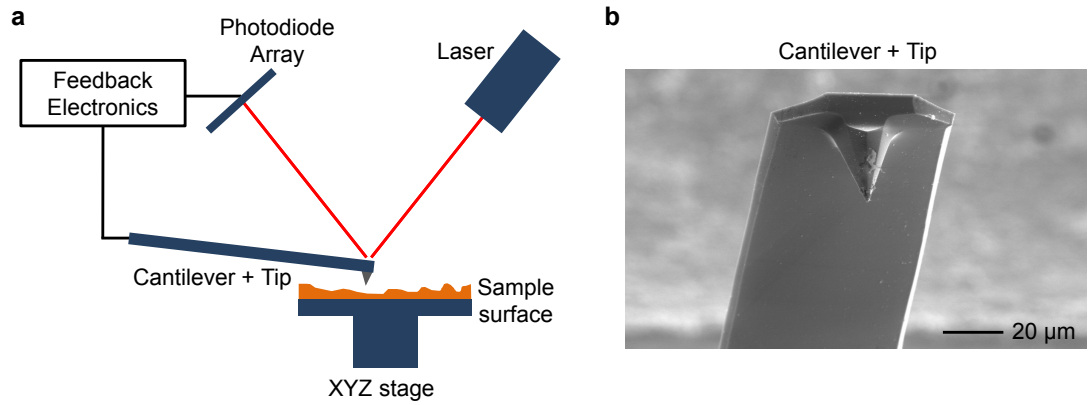

Figure 3.11: Atomic Force Microscopy (AFM) for imaging the surface topography. (a) Illustration of the working principle of an AFM and (b) an image of a cantilever including the tip (image was taken from [171]).

For large surface-tip distances no interaction occurs. When moving closer to the sample, attractive van-der-Waals interactions predominate and for very small distances repulsive forces due to Coulomb interactions occur. The AFM images presented in this thesis were recorded in tapping mode, where the change of oscillation amplitude gives rise to the surface topography [172], using a *JPK NanoWizard® II*.

4 Unravelling the multilayer growth of the fullerene C_{60}

Molecular semiconductors like the fullerene C_{60} are increasingly used in devices, but the understanding of elementary nanoscopic processes in molecular film growth such as the surface diffusion, the lateral binding and the step-edge crossing is in its infancy. So far, molecular self-assembly and growth [5, 6] has often been characterized by scaling laws to describe surface roughening and evolving island densities [32, 33]. On a molecular level, a range of studies have elucidated the kinetics of diffusion and nucleation (see, for example, refs [34–40]) and the Ehrlich–Schwoebel barrier for interlayer transport across a molecular step edge [34, 41, 42]. Yet to date, there is no organic compound for which even the 'minimal' set of the three parameters diffusion barrier, lateral binding energy and Ehrlich–Schwoebel barrier have been simultaneously quantified to describe multilayer molecular growth. Therefore, predictive simulations of the rate- and temperature-dependent morphology in molecular multilayer growth have so far been impossible, contrary to the situation for elemental atomic systems [47–49] and colloids [50–52]. The prototypical molecular semiconductor C_{60} is not only relevant for device applications, but also an important, fundamentally unique material bridging atoms and colloids. On one hand, its van-der-Waals diameter of 1 nm [63] is closer to atomic dimensions than to the mm length scale of colloidal systems. On the other hand, C_{60} resembles colloids with its short-range nature of the effective centre-of-mass interactions [64, 65].

From the experimental side, a particular challenge in studying C_{60} growth is that post-growth changes [70, 71] make the interruption of this non-equilibrium process to image different growth stages potentially misleading. It is therefore essential to use *in situ* real-time techniques.

In this chapter a combination of specular x-ray growth oscillations [56] with real-time diffuse x-ray scattering [58, 173] to simultaneously follow the vertical and lateral morphology during growth is employed. A comparison of experimental measures like island density and layer coverages with kinetic Monte Carlo (KMC) simulations of coarse-grained C_{60} molecules provides a understanding of processes occuring on the nanoscale. Then, the three relevant parameters determined are the Ehrlich–Schwoebel barrier, the sur-

face diffusion barrier and the lateral binding energy. With these parameters alone, we achieve quantitative agreement with the experimental data, enabling us to predict the rate-, temperature- and thickness dependency of the film morphology. Moreover, the analysis demonstrates that the short interaction range of C_{60} as compared with atoms affects the relative heights of diffusion barrier and binding energy and results in comparatively long diffusion times. However, unlike the colloidal systems, C_{60} has a true energetic Ehrlich–Schwoebel barrier, rather than the pseudobarrier that colloids display [50]. Given the observed results a step forward to answering the fundamental question of the rational design of molecular nanomaterials is made.

The chapter is organized as follows: In section 1 the vertical and lateral structure of the fullerene C_{60} on mica will be discussed. Section 2 deals with the real-time evolution of the lateral and vertical thin film morphology during the multilayer growth of C_{60}. In section 3 a self-consistent set of energy barriers, the diffusion energy, the lateral binding energy and the step-edge barrier, is quantified for the first time, which makes predictive simulations of C_{60} nanomaterials possible. Afterwards, section 4 gives information about the influence of the short-range nature of attractive interactions of the fullerene on the growth dynamics. Finally, the postgrowth dewetting of C_{60} on mica is followed in real-time for different temperature in order to shed light on the surface processes involved.

4.1 Structural order of C_{60} on mica(001)

In this section we focus on a short overview of the lateral and vertical structure of C_{60} thin films. To shed light on the crystallographic order x-ray reflectivity (XRR) and Grazing Incidence X-ray Diffraction (GIXD) measurements have been performed *ex situ* on a rotating anode lab source (Cu-K_α radiation, $\lambda = 1.54$ Å), see Section 3.1.6 for details.

4.1.1 Vertical film structure of C_{60} on mica(001)

In Figure 4.1 the XRR measurement of 10 monolayer(ML) C_{60} on mica, grown at 60 °C, as a function of the vertical momentum transfer $q_\perp$ is shown. Pronounced *Kiessig fringes* as well as several Bragg-reflections can be seen. The appearance of *Kiessig fringes* and Bragg-reflection for a C_{60} thin film implies the growth of smooth crystalline C_{60} layers, which is a prerequisite for the observation of growth oscillations. The mica Bragg-reflections can be assigned to be (001)-, (002)- and (003)-reflections stemming from the layered mica structure introduced in Section 2.3.3. The much broader and weaker reflection at 0.76 $Å^{-1}$ stems form the crystalline C_{60} layers and can be assigned to the fcc(111)-reflection of the C_{60} thin film.

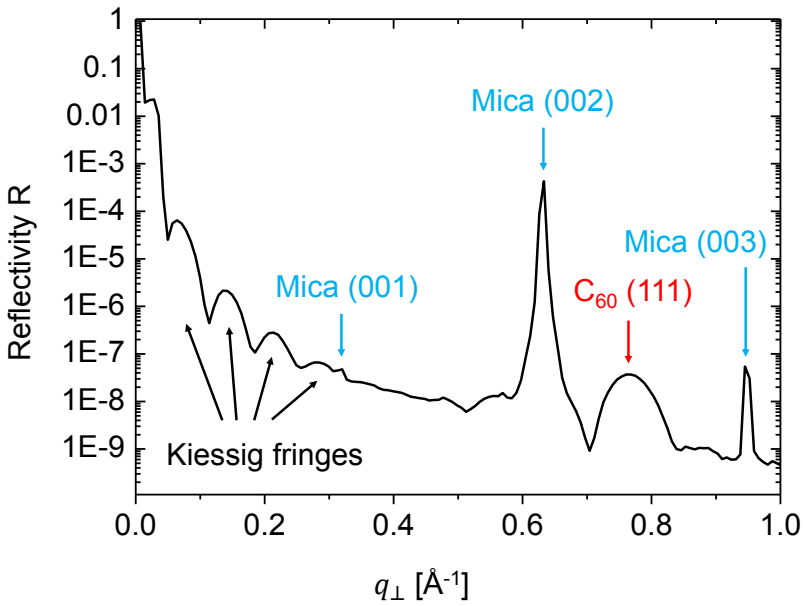

Figure 4.1: Smooth crystalline layer growth of C_{60} on mica(001). X-ray reflectivity measurement of a 10 monolayer(ML) thick C_{60} film on mica(001) indicates a smooth crystalline layer structure for C_{60} on mica. The out-of-plane lattice constant corresponding to the C_{60}(111) Bragg reflection is 8.3 Å.

The C_{60}(111)-orientation perpendicular to the surface is favored for substrates with a C_{60}-substrate interaction being weaker than the C_{60}-C_{60} interaction, such as for mica [122]. From the position of the Bragg-reflection the fcc lattice parameter as well as the C_{60} layer spacing can be deduced. The fcc lattice parameter is 14.2 Å and nicely agrees with literature [130]. Additionally, the spacing of C_{60} layers can be derived to 8.3 Å.

4.1.2 Epitaxial order of C_{60} on mica(001)

To reveal the epitaxial order of C_{60} on the crystalline mica(001) GIXD has been used, which provides information on the registration between mica and C_{60} crystallites as a function of the in-plane momentum transfer $q_{||}$. In particular, azimuthal rotation of the sample at constant lateral momentum transfer $q_{||}^{C_{60}(220)} = 1.254$ Å^{-1} and $q_{||}^{mica(020)} = 1.394$ Å^{-1} corresponding to the C_{60} (220)-reflection (lattice spacing of 5 Å) and mica (020)-reflection (lattice spacing of 4.5 Å) has been used to reveal the epitaxial order of C_{60} regarding the underlying mica substrate. In Figure 4.2a the GIXD reflections of C_{60} and mica are shown in red and blue for a 15 ML thin C_{60} film as a function of the azimuthal rotation angle.

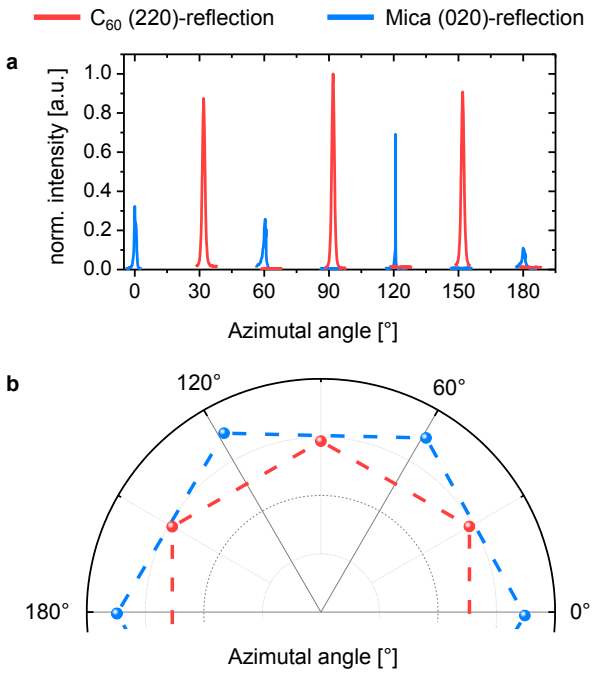

Figure 4.2: Epitaxial growth of C_{60} on mica(001). (a) GIXD reflections at $q_{||}^{C60(220)} = 1.254$ Å^{-1} and $q_{||}^{mica(020)} = 1.394$ Å^{-1} and (b) pole figure of C_{60} and mica reflections as a function of the azimuthal angle show that both C_{60} and mica feature a reflection every 60° so that one can exclude a 2D powder like growth of C_{60}.

Both C_{60} and mica feature a reflection every 60° so that we can exclude a 2D powder like growth of C_{60}. Nevertheless, multiple domains and stacking faults are possible and cannot be excluded. The angular offset of the C_{60}-reflection regarding the mica-reflection of approx. 30°, clearly shown in the corresponding pole figure in Figure 4.2b, indicates a relative orientation of the C_{60} unit cell on the underlying mica with, as well, 30° between C_{60} and mica crystallites. This epitaxial growth of hexagonal arranged C_{60} molecules (C_{60}-fcc(111)-orientation normal to the surface) on top of the hexagonal SiO_4-tetrahedron substrate layer of mica [150] is illustrated in Figure 4.3. From this, two different adsorption geometries have been reported [174]: the C_{60} molecules can directly be located on top of one SiO_4-tetrahedron or between the triangle built up by tetrahedrons. To answer this question in a detailed way, more extensive x-ray scattering experiments have to be performed as has been done in reference [174] in terms of multi-reflection pole figures and in reference [175] in terms of the analysis of crystal truncation rods (CTRs), which goes beyond the scope of this work. Not only the adsorption geometry of C_{60} on top of mica is shown in Figure 4.3 but also the lattice spacings extracted from the positions of C_{60} and mica Bragg-reflection are displayed. For the hexagonal SiO_4-tetrahedron substrate layer of mica a distance of neighboring tetrahedrons is found to be 5.2 Å which is in accordance

with previous structural studies of the material system C_{60}/ mica [174, 176]. For C_{60} a distance in the $(0\bar{1}1)$-direction of 10 Å is deduced for C_{60} neighbors within the hexagonal arrangement of the fcc(111) surface structure, which nicely agree with the *van-der-Waals* diameter[1] of the fullerene C_{60} of 10 Å [63].

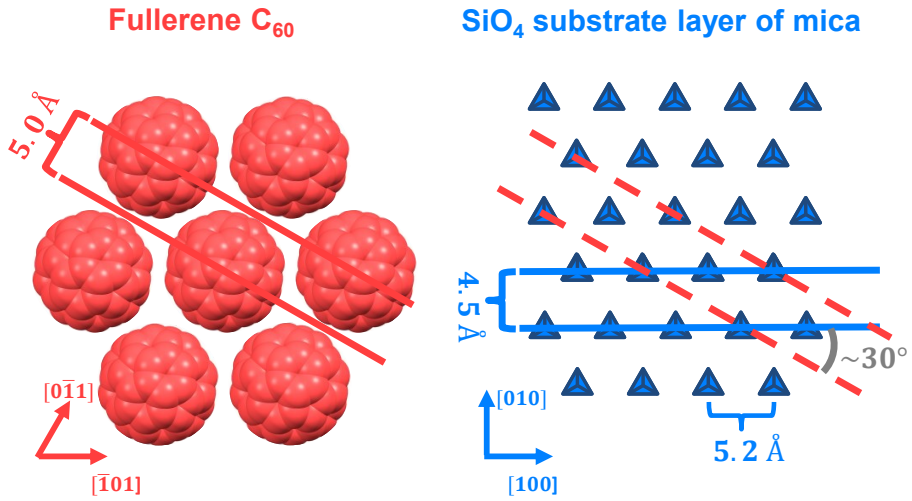

Figure 4.3: Adsorption geometry of C_{60} on mica. The C_{60} molecules grow in hexagonal arranged C_{60} molecules (C_{60}-fcc(111)-orientation normal to the surface) on top of the hexagonal SiO_4-tetrahedron substrate layer of mica.

Strain Due to the epitaxial order of C_{60} on top of mica an estimate of the amount of lattice strain is appropriate. To this end, a closer inspection of the lattice parameters gained by GIXD has been performed. As we have learnt from the previous considerations the fullerene C_{60} crystallizes in the face-centered cubic (fcc) structure and exhibits a lattice constant in the bulk crystal of 14.15 Å [130]. The (220)-reflection of C_{60} on mica for a 15 ML thin film is located at $q_{||}^{C60(220)} = 1.254$ Å^{-1} in reciprocal space. Comparing the experimental finding with the theoretical position of the reflection in reciprocal space at $q_{||}^{C60} = 1.256$ Å^{-1} calculated for the lattice constant of the crystal bulk phase, we find that the lattice strain is at most 0.2% for the 15 ML thin film, which is very small for a molecular system which can be as large as 8% strain for PTCDA on Au(111) [177]. Note, a lattice mismatch of 3.8% has been observed considering the lattice spacing of C_{60} (5.0 Å) and the neighboring distance of SiO_4-tetrahedrons on mica surface (5.2 Å) deduced from the Bragg reflections. This observation is in agreement with literature [122], in which a lattice mismatch of 3.4% has been reported for one monolayer of C_{60} on mica.

[1] Measure of the degree of the close-packing within a hard-sphere model

4.1.3 Structural order of C_{60} on mica: Summary

- Smooth and crystalline layer structure of C_{60} on mica(001) normal to the surface with a layer separation of 8.3 Å and a fcc lattice spacing of 14.2 Å,
- epitaxial growth of C_{60} on mica with a hexagonal arrangement of C_{60} molecules reproducing the hexagonal mica surface structure,
- lattice mismatch of 3.8% between C_{60} and underlying SiO_4-tetrahedrons on mica surface.

4.2 Real-time evolution of the vertical and lateral film morphology: layer-by-layer growth of C_{60} on mica

For a comprehensive understanding of the processes during growth, the surface morphology has to be measured on the molecular length scale with an experimental time resolution that is fast compared to the minute timescale of the deposition of a monolayer. Interrupting growth to take a series of real-space microscopy images can be problematic, as the morphology can be altered. For our system of C_{60} on top of a closed first C_{60}-layer on mica this route is indeed impossible because of quick dewetting effects characterized by a time constant of $\propto 10$ minutes (see Section 4.5 for details on C_{60} dewetting). Also, *in situ* low energy electron microscopy (LEEM) unfortunately - while very successfully used in a range of studies [178, 179] - cannot be applied due to charging effects on mica. Therefore, we use x-ray scattering that can be performed non-invasively during growth and yields time-resolved information about the layer formation. This information is extracted through specular reflectivity measurements at the so-called anti-Bragg position of C_{60} corresponding to half the Bragg value ($q_{anti-Bragg} = 1/2 q_{Bragg}$) of the C_{60}(111)-reflection (see Figure 4.4a). Lateral information is available through simultaneous measurement of the diffuse scattering (GISAXS) during the growth, giving information about the island distance and island density. The growth has been performed in our portable UHV chamber designed for molecular beam deposition described in section 2.4 at a base pressure of 10^{-8} mbar. Fullerene C_{60} has been thermally deposited on freshly cleaved mica for two different deposition rates (0.1 ML/min and 1 ML/min) and for three different substrate temperatures (40 °C, 60 °C and 80 °C) to study rate-, temperature- as well as time-thickness-dependency of the island density and layer coverage.

4.2.1 Layer-by-layer growth of the fullerene C_{60} on mica(001)

The time-dependent specular x-ray reflectivity as a function of molecular exposure, that is time*deposition rate, is shown in Figure 4.4b for growth at $T = 60$ °C substrate temperature and a deposition rate of $f = 0.1$ ML/min. The anti-Bragg intensity oscillates with a period of two monolayers (ML) as the x-rays are reflected from consecutive C_{60} layers and alternately interfere destructively and constructively with an intensity- modulation of up to 90%. Here, the diffusely scattered intensity can be neglected in an analysis of the specular reflectivity, as it represents less than 1% of the total intensity. The oscillations are indicative of a layer-by-layer growth and only after the first three layers one observes a damping of the oscillations, reflecting the onset of slight roughening. While the diffuse scattering is weak, it nevertheless contains important lateral information.

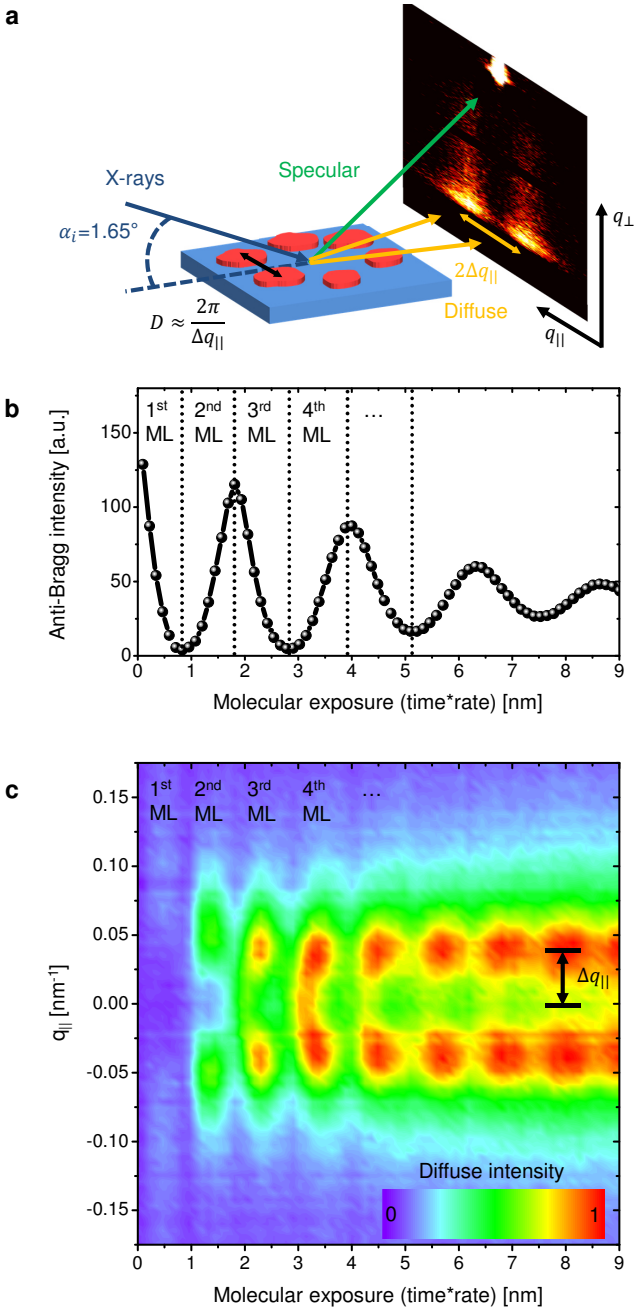

Figure 4.4: Specular and diffuse x-ray scattering during C_{60} growth. (a) Scattering geometry: The 2D scattering pattern contains both lateral (momentum transfer $q_{||}$) and vertical ($q_\perp$) information on the surface morphology. (b) The specular x ray reflectivity at the anti-Bragg point $q_\perp = 0.38$ Å^{-1} oscillates indicating layer-by-layer growth ($T = 60$ °C). (c) The diffusely scattered intensity oscillates with the nucleation and coalescence of every layer and exhibits a characteristic peak-splitting $\Delta q_{||}$.

Figure 4.4c shows a map of the diffusely scattered intensity as a function of lateral momentum transfer $q_{||}$ and molecular exposure. In contrast to the anti-Bragg oscillations,

the diffusely scattered intensity oscillates with a period of one monolayer. As the first molecules are deposited in a monolayer, the surface roughness and therefore the diffusely scattered intensity rises due to nucleation of islands. Eventually, as the islands coalesce, the roughness and diffuse intensity decrease again, before reaching a minimum for a smooth complete layer. For each C_{60} layer the diffusely scattered intensity has two maxima along $q_{||}$, because the characteristic average island distance D causes an increase of the diffusely scattered intensity at $\Delta q_{||} \approx \pm 2\pi/D$ [57, 58, 173].

So far, the observed specular and diffuse growth oscillations (and their origin) have been discussed on a more qualitative level. In the following a quantitative analysis on the growth characteristic of C_{60} on mica will be given for the lateral as well as the vertical film morphology.

4.2.1.1 Vertical film morphology: detailed information on layer filling

From the specular x-ray growth oscillations not only qualitative information can be obtained but also quantitative information. From the change in oscillation period a variation of the sticking coefficient is deduced. The sticking coefficient is found to decrease during the growth of the first four layers for all studied temperatures. Quantitatively, we find for a temperature of 60°C that with respect to the growth of the first monolayer, the sticking coefficient decreases by 5% in the second ML, 25% in the third ML and 30% from the fourth layer onwards. This decrease is due to the different mica-C_{60} and C_{60}-C_{60} interactions. It is further influenced by a different island density in each layer, which leads to a change in the free diffusion times and aggregation behavior.

Going beyond an analysis of the oscillations period the whole anti-Bragg oscillations shape can be calculated in kinematic approximation using

$$I_{anti-Bragg} = \left| A_{sub} e^{i\phi_{sub}} - F_{mol} \sum_{n=1} \theta_n(t) e^{i\pi n} \right|^2 \tag{4.1}$$

with the layer coverages θ_n for the n^{th}-layer. The substrate amplitude A_{sub}, the substrate phase ϕ_{sub} and the molecular form factor F_{mol} are determined by maximal, minimal and saturation intensity of the real-time experiment [100]. For extracting the layer coverages during growth we employed the mean-field analytical model for thin film growth by Trofimov et al. [108, 109] and Woll et al. [110], which has already been used in growth studies of organic systems [99, 110, 111]. The fitted anti-Bragg growth oscillations for the film grown at $T = 60$°C with a deposition rate $f = 0.1$ ML/min are shown in Figure 4.5a up to 16^{th} monolayer. Excellent agreement between experimental data and fit can be seen. Fitting the anti-Bragg growth oscillations enables us to quantify the layer nucleation.

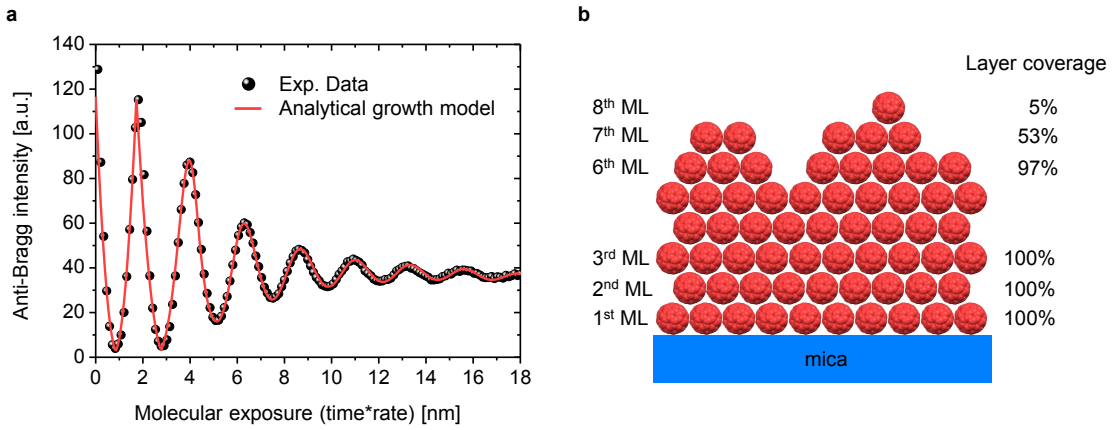

Figure 4.5: Vertical layer nucleation of C_{60} on mica. (a) Anti-Bragg growth oscillations fitted by the analytical growth model and (b) illustrated layer coverages at a molecular exposure of approx. 7 nm. The analytical growth model predicts that the 6^{th}, 7^{th} and the 8^{th} monolayer grow simultaneously resulting in an increase of thin film roughness.

In particular, the model predicts that the first monolayer at $T = 60$ °C is filled 99% before the first 1% of the second monolayer is nucleated. Additionally, roughening and the onset of the simultaneous growth of, e.g., three monolayer has been quantified as illustrated in Figure 4.5b. At a molecular exposure of approx. 7 nm the 6^{th}, 7^{th} and the 8^{th} monolayer grow simultaneously leading to an increase of the film roughness, whereby the further decrease in anti-Bragg intensity is explicable.

Anti-Bragg intensity during the growth of the first monolayer of C_{60} on mica One curious side-observation of the C_{60} growth oscillations is, that the reflectivity of the C_{60} growth oscillations reaches almost zero after deposition of one C_{60} ML, i.e. the reflected counts are reduced from $I_{max} = 1.3 \cdot 10^6$ to $I_{1ML} = 4 \cdot 10^4$. Using the formula for the anti-Bragg oscillations given by equation 4.1, we fit the experimental growth oscillations and in particular the value of the minimal reflectivity at 1 ML coverage:

$$I_{anti-Bragg}(1ML) = \left| A_{sub} e^{i\phi_{sub}} - F_{mol} \sum_{n=1}^{1} 1 \cdot e^{i\pi \cdot 1} \right|^2 . \tag{4.2}$$

Obviously, the scattering can vanish if the amplitudes involved are comparable and the phases are destructive (near 180°). If we insert the numbers appropriate for our system, we find indeed a nearly vanishing resulting intensity:

$$I_{anti-Bragg}(1ML) \propto I_{max} \cdot \left| 1 \cdot e^{i\left(170° \frac{\pi}{180°} - \pi\right)} - 0.92 \right|^2 = \frac{I_{max}}{32}. \tag{4.3}$$

Note that C_{60} has a scattering amplitude that is a little smaller than the mica scattering amplitude ($F_{Mol} = 0.92 \cdot A_{sub}$) and has a relative phase of $\phi_{sub} = 170°$. In Figure 4.6a graphical illustraction of the scattering amplitude and the phase is shown in a complex plane.

An alternative Parratt formalism calculation of the absolute reflection intensities (with the same qualitative and quantitative result) uses the material densities of 1.65 g/cm^3 for C_{60} [180] and 2.83 g/cm^3 for mica [181]. From the density the mica and C_{60} scattering length density (SLD) are calculated using

$$SLD = \frac{\rho}{M} \cdot N_{Avogadro} \cdot N_{el} \cdot r_e \tag{4.4}$$

with the bulk material density ρ, the molar mass M (taking into account the chemical composition of mica ($KAl_3Si_3O_{12}H_2$) and the fullerene C_{60}), the number of electrons N_{el} (for $KAl_3Si_3O_{12}H_2$ and C_{60} respectively) and the Thomson scattering length $r_e = 2.818 \cdot 10^{-5}$ Å. This gives a mica scattering length density of $2.4 \cdot 10^{-5}$ Å^{-2} in agreement with literature values [182], and for C_{60} a scattering length density of $1.4 \cdot 10^{-5}$ Å^{-2} is obtained. Using these values for the SLD and a C_{60} monolayer thickness of 8.3 Å(corresponding to the C_{60} lattice constant deduced in Section 4.1.1) we arrive at SLD profiles shown in Figure 4.6b for the bare substrate (vacuum/ mica interface) and the one monolayer C_{60} on mica structure (vacuum/ C_{60} (1ML)/ mica). To this end, the Parratt formalism has been used for the calculation of the reflectivity of stratified layers from the scattering density profile. Figure 4.6c shows the calculated x-ray reflectivity as a function of $q_\perp$ for the bare substrate and 1ML on the substrate. For the C_{60} on mica reflectivity a pronounced dip (*Kiessig fringe*) can be seen at the anti-Bragg point of C_{60} ($q_\perp = q_{AB}^{C60} = 0.38$ Å^{-1}, which is equivalent to an incidence angle $\theta = 1.65°$) due to the C_{60} layer reflectivity. From the simulated reflectivity we find a reduction by a factor of 31 at the anti-Bragg point ($4.3 \cdot 10^{-6}$ for bare mica to a reflectivity of $1.4 \cdot 10^{-7}$ with one C_{60} ML) neglecting the small contribution of surface roughness in the calculation. Comparison with the experimentally observed reduction by a factor of 32 as obtained from the growth oscillations count rates for 0 ML and 1 ML in Figure 4.6d shows good agreement between theory and experiment.

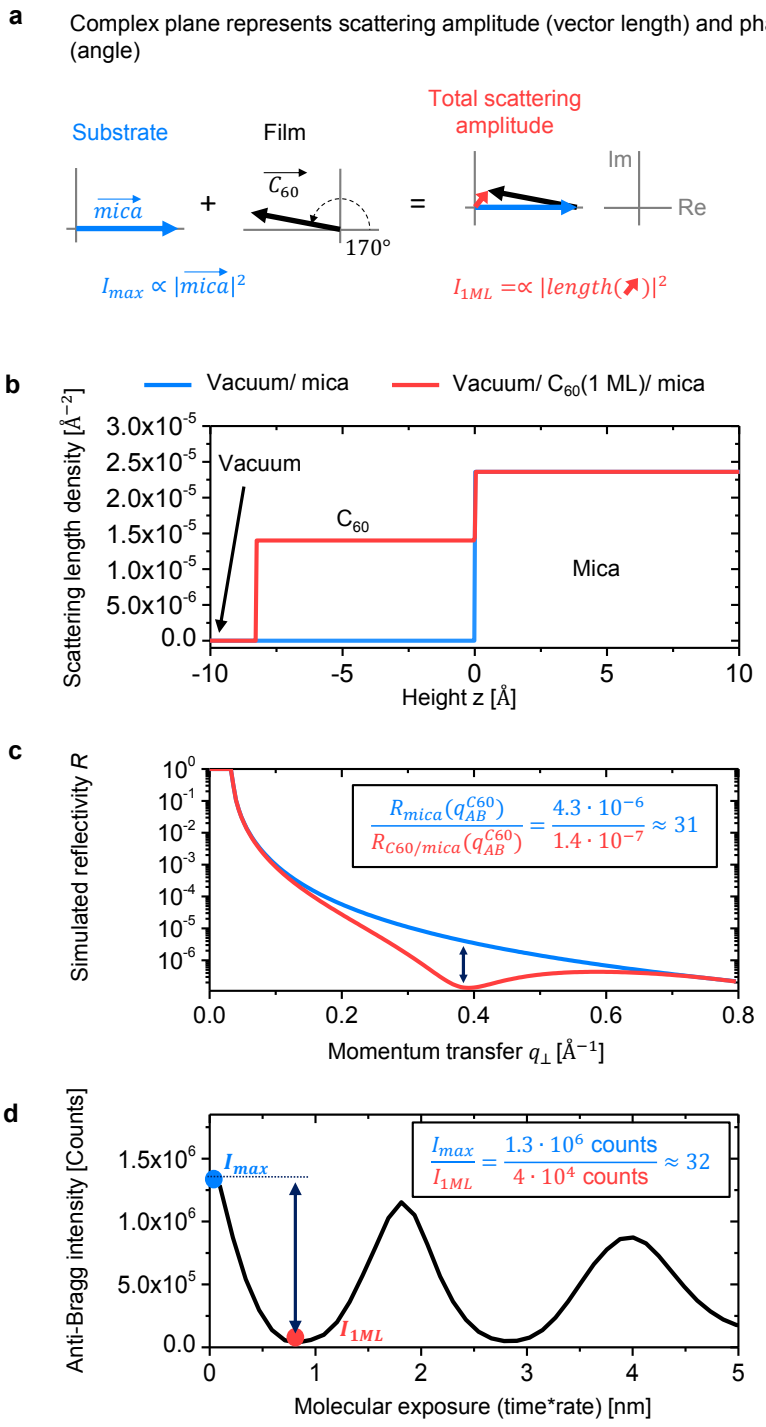

Figure 4.6: Anti-Bragg intensity for the first grown monolayer of C_{60} on mica. (a) Complex plane representing the scattering amplitude and phase illustrates the difference in reflected intensity between the bare substrate (I_{max}) and one monolayer on top of the substrate (I_{1ML}). (b) Scattering length density for the simulation of the (c) reflectivity for the bare substrate and one monolayer C_{60} on mica. (d) Measured anti-Bragg intensity in total counts.

Layer-by-layer growth for all employed growth conditions In general, pronounced growth oscillations indicating layer-by-layer growth for C_{60} on mica have been observed for all employed growth conditions in the temperature range from 40 °C to 80 °C for a low (0.1 ML/ min) and high deposition rate (1 ML/ min) shown in Figure 4.7.

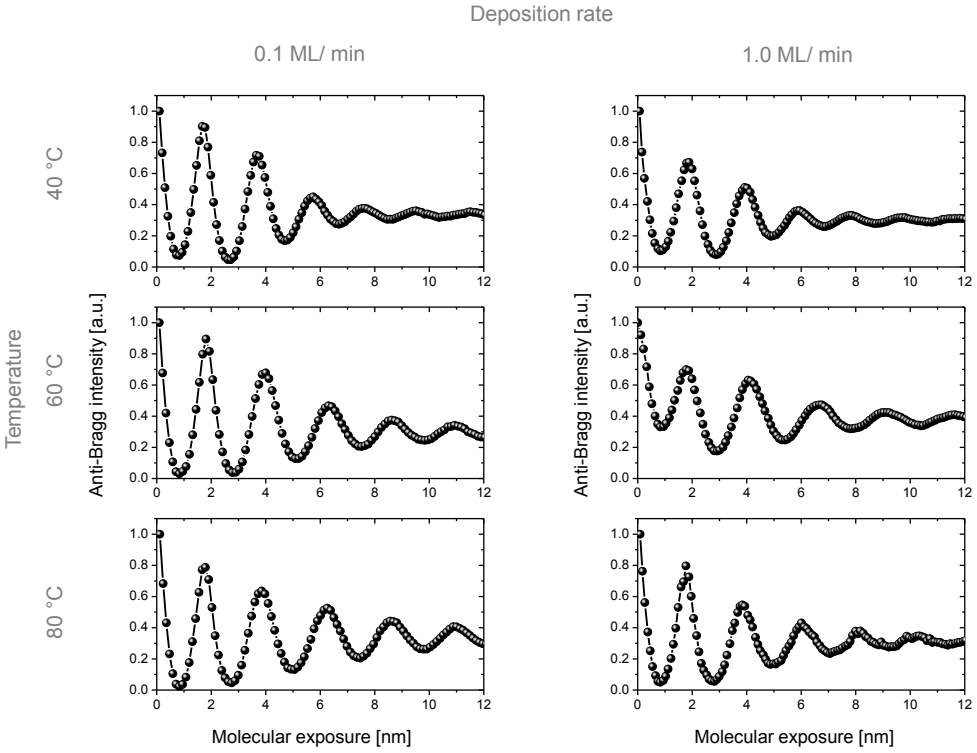

Figure 4.7: Layer-by-layer growth for all employed growth conditions. Growth oscillations for all employed growth conditions have been observed, which indicate layer-by-layer growth.

The specular growth oscillations contain information on the vertical growth characteristics like the onset of layer nucleation and change of sticking coefficient as a function of layer number. The simultaneous measurement of specular growth oscillations and diffuse scattering (GISAXS) enables us the characterization of the evolving lateral nanostructure.

4.2.1.2 Lateral film morphology: Insight in nucleation, lateral island growth and coalescence

To quantify the lateral nanostructure during growth the island density N has been directly extracted from the average island distance $D \approx 2\pi/\Delta q_{||}$ using

$$N = \frac{2}{\sqrt{3}} \frac{1}{D^2} = \frac{1}{2\sqrt{3}\pi^2} (\Delta q_{||})^2. \tag{4.5}$$

For this a hexagonal arrangement of compact (cylindrical shaped) islands is assumed. The average island distance D is directly deduced from the peak splitting $\Delta q_{||}$, which has been observed in the diffusely scattered intensity. This diffusely scattered intensity is shown in Figure 4.8 as a function of $q_{||}$ and molecular exposure for all applied growth temperatures (40 °C, 60 °C and 80 °C) for a deposition rate of 0.1 ML/ min.

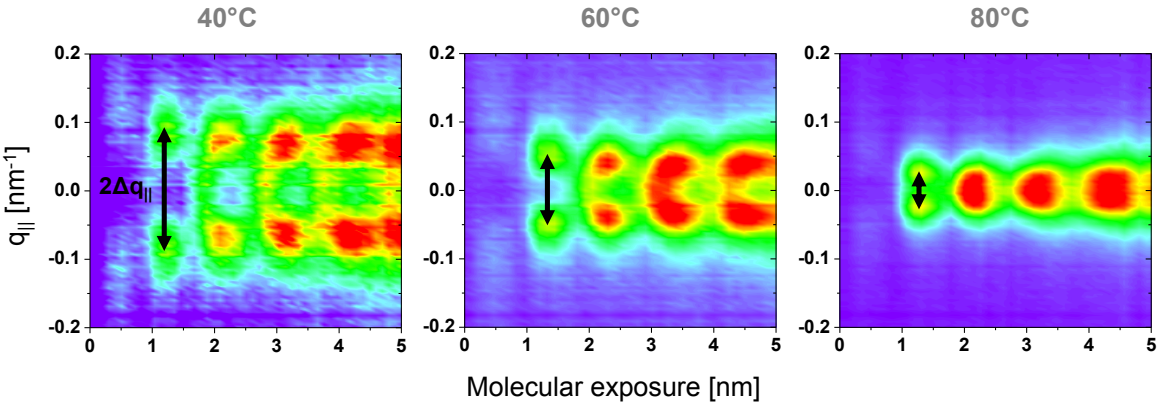

Figure 4.8: Peak-splitting in diffusely scattered intensity as function of temperature. The peak-splitting $\Delta q_{||}$ decreases with increasing temperatures associated with a strong dependence of the nanostructure on temperature.

To extract the exact peak position $\Delta q_{||}$ the 1D scattering pattern as a function of $q_{||}$ has been fitted for each measurement point in growth time using a symmetric double Lorenztian function

$$I_{diff}(q_{||}) = I_0 \left(\frac{\omega}{2(q_{||} + \Delta q_{||})^2 + \omega^2} + \frac{\omega}{2(q_{||} - \Delta q_{||})^2 + \omega^2} \right) + I_{back} \tag{4.6}$$

with the amplitude I_0, the width ω and the background intensity I_{back}. The island density as a function of molecular exposure can be calculated with $\Delta q_{||}$ using formula 4.5.

The quantification of the island density is done by the detailed analysis of reciprocal space methods. To show that the employed method quantifies correct length scales, a comparison of reciprocal and real space methods are presented in the following.

Equivalence of real-space and reciprocal-space methods Real-space images of the first layers using AFM are unfortunately not possible due to strong dewetting effects in the first monolayers for C_{60} on mica. Nevertheless, despite post-growth dewetting effects in the first layers, we could image the morphology of stable, thicker films with atomic force microscopy, as shown in Figure 4.9. In the kinematic approximation, the Fourier transform (FT) of the real-space structure corresponds to the diffusely scattered intensity in our x-ray experiments [167].

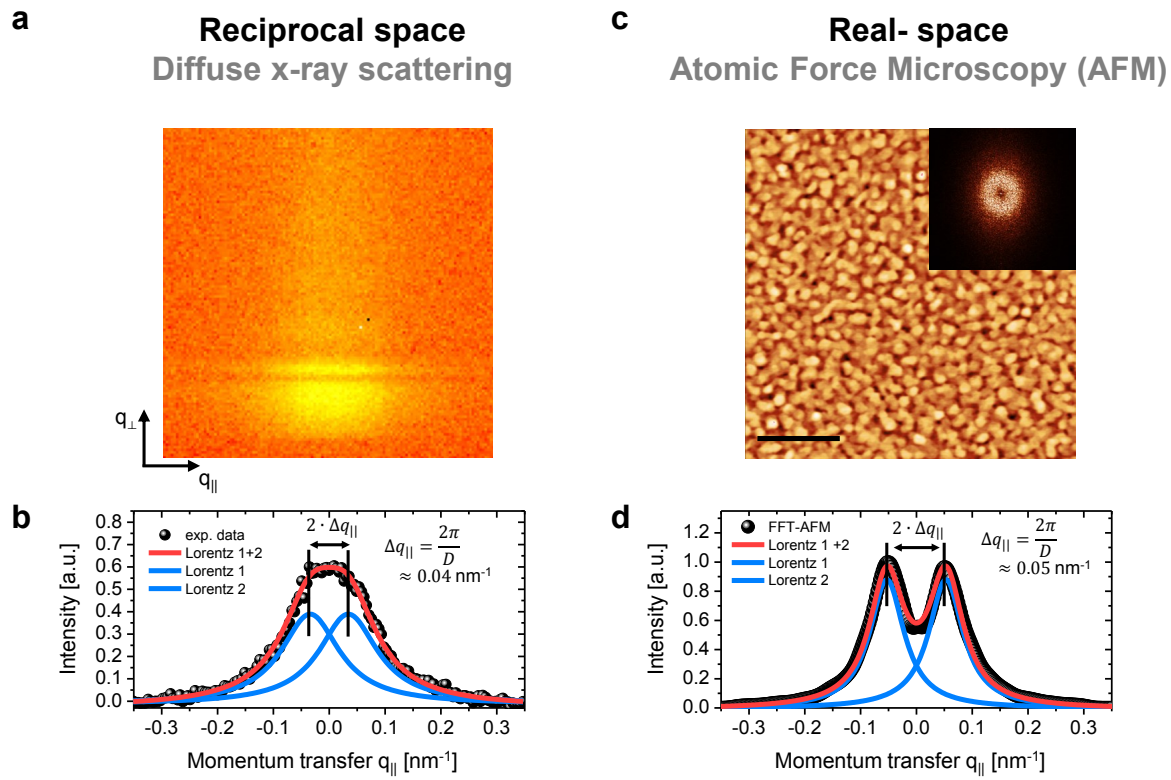

Figure 4.9: Comparison of reciprocal and real-space information. (a) Diffuse x-ray scattering (GISAXS) of a 14 ML thick C_{60} film, (b) line graph with Lorentz fits. (c) Corresponding AFM image of this film (scale bar: 500 nm) and its fast Fourier transform (FFT,inset). (d) Line graph of AFM Fourier transform. The good agreement between reciprocal- and real-space experiments confirms that our analysis determines correct lateral length scales.

Comparing the diffuse x-ray scattering, which unfortunately for the thick films is close to the resolution limit and the FT of the corresponding AFM image for a 14 ML thick film ($T = 60$ °C, high deposition rate of 1.0 ML/ min) we find very similar peak splitting of $\Delta q_{||} \approx 0.04$ nm^{-1}, respective 0.05 nm^{-1}. The line graph of the FT was convoluted with the resolution function of the experiment (normalized Gaussian function with a FWHM of 0.01 nm^{-1}). This good agreement between reciprocal- and real-space experiments confirms that the analysis presented determines correct lateral length scales.

Influence of temperature and deposition rate on the lateral structure: tailoring the nanostructure In Figure 4.10 the island density N during growth is shown for different growth conditions. Figure 4.10a shows the island density for 40 °C, 60 °C and 80 °C for a constant deposition rate 0.1 ML/ min as a function of the molecular exposure.

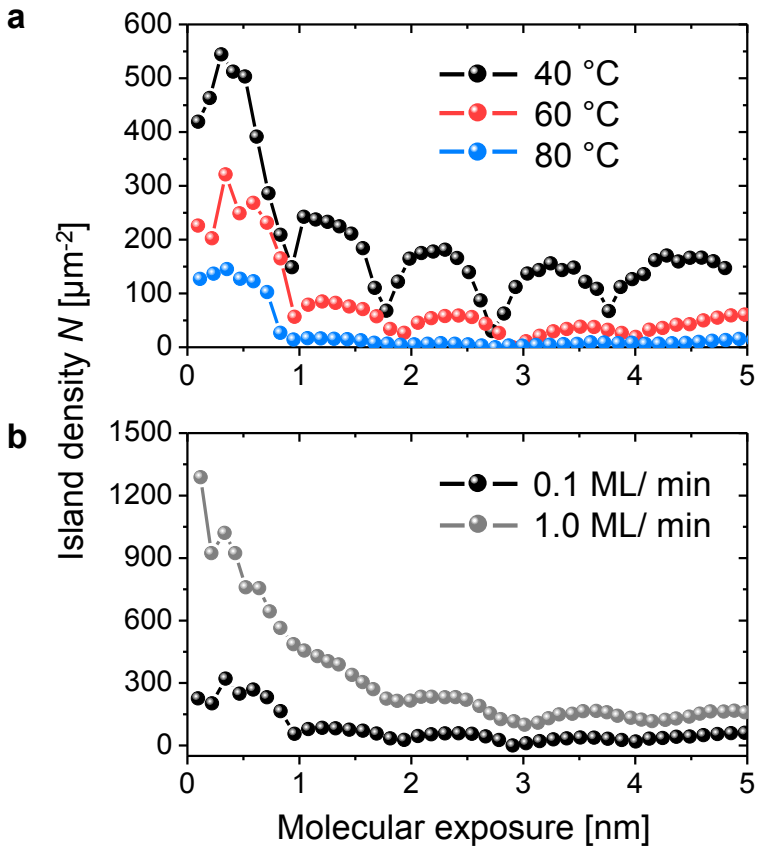

Figure 4.10: Tailoring the nanostructure with temperature and deposition rate. (a) The island density for 40 °C, 60 °C and 80 °C for a constant deposition rate 0.1 ML/ min and (b) island density for deposition rates of 0.1 ML/ min and 1.0 ML/ min at a constant temperature of 60 °C. It can be clearly seen that the nanostructure in terms of island density can be tailored by temperature and deposition rate.

In Figure 4.10b the island density for the two employed deposition rates of 0.1 ML/ min and 1.0 ML/ min at a constant temperature of 60 °C can be seen. Generally, the thin film nanostructure in terms of island density can be tailored by varying the growth conditions. In particular, an increase of temperature of 40 K from 40 °C to 80 °C leads to 20-times smaller island density. Furthermore, a 10-times larger deposition rate results in a *four*-times larger island density. This growth characteristic as a function of growth conditions follows established growth theories, in which the island density N can be described by

$$N \propto \left(\frac{f}{D(T)}\right)^{\frac{i^*}{i^*+2}} \tag{4.7}$$

with the deposition rate f and the diffusion coefficient/hopping rate $D(T)$. The pa-

rameter i^* denotes the critical island size (see section 2.1.1.1 for the origin of this scaling law). The diffusion coefficient/hopping rate is quantified by an Arrhenius behavior

$$D(T) = \nu_0 e^{-\frac{E_D}{k_B \cdot T}} \tag{4.8}$$

with the attempt frequency of the system ν_0, the diffusion energy E_D, the Boltzmann constant k_B and the temperature T. Unfortunately, there is not enough data for deducing the critical island size i^* quantitatively. An estimation based on equation 4.7 gives that a $four$-times larger island density for a 10-times larger deposition rate is observed if the critical island size i^* is 3.

Smaller island density with increasing layer number An additional growth feature observed is the decrease of island density for an increasing film thickness, that is an increase of island size for an increasing layer number. This phenomenon has also been observed for the homoepitaxy of $SrTiO_3$ $\langle 001 \rangle$ during pulsed laser deposition [49]. This has been explained by a surface's "memory" effect of the underlying layers. During the nucleation of a new layer on top of a uncompleted layer the remaining holes function as adatom sinks, which lead to a reduction of the adatom density and therefore to a smaller nucleation/ island density. This effect can also account for the reduction of island density for C_{60} from the second layer onwards, where homoepitaxy of C_{60} on C_{60} takes place. In contrast, the different island size in the second layer is not due to these "adatom sinks" as we know, that the first layer is almost completely filled before the second layer nucleates. The change in island density from the first to the second layer can be explained by a different diffusion characteristics in the respective layer as found by Frank et. al for diindenoperylene (DIP) on SiO_2 [99]. To this end, stacking faults and/ or grain boundaries of mica and/ or even heterogeneous nucleation could be reasons for an different diffusive behavior for C_{60} on mica.

Nucleation, lateral growth and coalescence during layer growth One more significant feature during the layer-by-layer growth of C_{60} is the oscillating behavior of the island density as a function of the molecular exposure in Figure 4.10. The growth of one specific layer follows a periodic *three-regime* pattern.

1. *Nucleation:* Initially, as the first islands nucleate on the surface, the island density increases.

2. *Lateral island growth:* Then lateral growth sets in, where the island density stays constant, as nucleation of new islands is suppressed.

3. *Coalescence:* Finally, the island density drops again as islands merge in the coalescence regime.

The sequence of growth regimes is observed for the first five layers at each temperature and deposition rate employed.

4.2.2 Summary: lateral and vertical film morphology of C_{60} on mica

- Real-time and *in-situ* specular x-ray reflectivity and diffuse GISAXS oscillations are powerful tools for non-invasive real-time studies of the morphological evolution during molecular growth,
- C_{60} molecules grow in layer-by-layer mode on mica,
- from the diffuse x-ray scattering three growth regimes within one monolayer have been deduced: nucleation, lateral island growth and coalescence regime.

4.3 Nanoscopic understanding of molecular growth: Revealing the surface diffusion, lateral binding energy and step-edge barrier

To understand the morphological evolution during C_{60} growth on a molecular level KMC simulations have been applied to our data in collaboration with *Prof. Sabine H.L. Klapp* and *Nicola Kleppmann* from the *Technische Universität Berlin*, who have implemented and performed the simulations. The work presented here has been published in Nature Communications [112] and has been prepared in close collaboration with N. Kleppmann and S.H.L. Klapp from TU Berlin.

4.3.1 Details on the KMC simulations

KMC simulations are capable of describing the entire growth process of (coarse-grained) C_{60} molecules into an fcc lattice. KMC models the growth as a stochastic process, in which the molecules adsorb with a constant net adsorption rate $f = f_{adsorb} - f_{desorb}$. The molecules are treated on a coarse-grained level in this simulations, that is, any internal (rotational, or vibrational) degrees of freedom are not taken into account. This coarse-graining approach is supported by the fact that for the temperatures studied here, C_{60} rotates freely both in bulk crystals [130] and in one-dimensional confinement [183]. Once adsorbed, a particle at site i then can diffuse to a neighboring fcc site j via an activated process with Arrhenius-type rate $r_{i,j}$. We follow the Clarke-Vvedensky bond-counting approach [114, 115], where the rate is defined as

$$r_{i,j} = \frac{2k_BT}{h} \cdot exp\left(-\frac{E_D + n_iE_B + s_{i,j}E_{ES}}{k_BT}\right). \tag{4.9}$$

The prefactor $\nu_0 = 2k_BT/h$ is chosen in accordance with previous KMC studies for atomic systems [116–118], consistent with our coarse-grained description of C_{60} as a sphere. The total energy barrier for molecular hopping consists of a barrier for free diffusion, E_D, and contributions determined through the local neighborhood of the particle (see Figure 4.11 for an illustration of the energy barriers). The neighbor binding energy E_B contributes with the number of lateral neighbors n_i. The sum of E_D and n_iE_B then determines the lateral diffusion ($s_{i,j} = 0$) and thus, the growth of islands. Other pre-factors to the neighbor binding energy have been suggested in literature [43,48], which increase the diffusion rate of particles along island edges. As a consequence the islands become more compact.

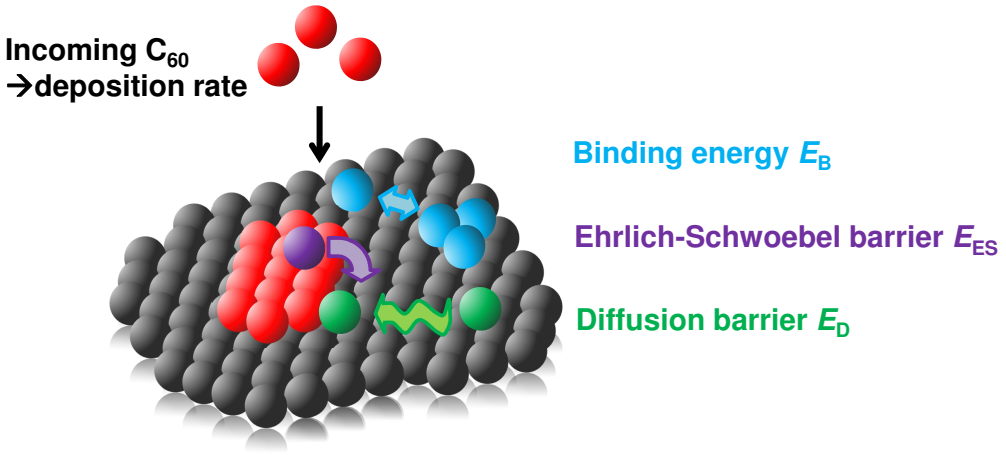

Figure 4.11: Surface processes during the growth of the fullerene C_{60}. The lateral binding characterized by the lateral binding energy E_B, the interlayer diffusion across a step-edge (Ehrlich-Schwoebel barrier E_{ES}) and the diffusion barrier (E_D) are the major processes on the surface during growth.

In our C_{60} system, however, the islands are quite compact from the very onset of the growth (see the inset in Figure 4.12b). Therefore, the details of the pre-factor of E_B do not significantly influence the results at the parameters considered. If a particle at site i crosses an up- or downward step to reach site j, an additional Ehrlich-Schwoebel contribution E_{ES} is added to the total energy barrier ($s_{i,j} = 1$). As a result, a particle diffusing onto an island from an edge site with two neighbors has to overcome the activation energy $\Delta E = E_D + 2E_B + E_{ES}$, while a particle on the island has to overcome only $\Delta E = E_D + E_{ES}$ to diffuse downwards over the island edge. The step-edge energy barrier used in our simulations is, by construction, an average energy barrier. For this we recall that the energy barriers are exclusively gained by comparison to the x-ray scattering experiment, and that the experimental data are intrinsically averaged in lateral direction. Therefore, we did not take into account the orientation of the step-edge in this study. The KMC input parameters T (substrate temperature) and f (adsorption rate) are taken directly from experiment. Additionally, in the KMC simulations, which otherwise assume complete condensation, we have accounted for the changing sticking coefficient deduced from the change of oscillations period during growth (see Section 4.2.1.1) by scaling the molecular exposure axis accordingly. The KMC simulations have been performed from the second layer onwards as we concentrate on the C_{60}-C_{60} interactions and do not model C_{60}-mica interactions.

This strategy is justified, as we know from the experiment that the first C_{60} layer is completely filled and that there is no significant lattice strain; thus, we can assume a

smooth C_{60}(111)-surface as initial surface in simulations. Furthermore we assume defect-free growth without cavities or overhangs. Note, we do not take collective diffusion mechanisms into account. Different concepts for collective diffusion have been suggested in the literature, one example being dimer shearing [184]. More recently, approaches have been suggested for shearing, reptation and concerted gliding of islands [185]. These phenomena are certainly worth studying in more detail, however, it would not have been possible to simulate the time and length scale required in our study possible if these effects were included.

4.3.2 Energy barriers for the surface processes during the C_{60} growth

For the comparison of experiment and simulations, the time dependent layer coverages from KMC simulations have been used to calculate anti-Bragg oscillations with formula 4.1 in kinematic scattering theory [100]. The energy barriers E_D, E_B and E_{ES} (see equation 4.9) are then adjusted until both the simulated anti-Bragg oscillations and island densities fit the experiment. Figures 4.12a, 4.12b, 4.12c and 4.12d show experimental (black dots) and KMC simulation data (red solid line) for the island density and the anti-Bragg intensity for the temperatures $T = 40$ °C and $T = 60$ °C. Both the experiment and the simulation predict that the island density changes markedly during the deposition of each monolayer. Initially, in the nucleation regime, the island density increases. Then lateral island growth sets in, where the island density stays constant. Finally, the island density drops again as islands merge in the coalescence regime.

The inset in Figure 4.12b shows the corresponding KMC simulation snapshots for the three growth regimes. As it is clearly seen from the comparison, there is excellent agreement between the experimental and simulated data regarding the island density and anti-Bragg growth oscillations. The minima and the maxima in the island density, as well as the trend of decreasing density for the different layers (increase of island size), are clearly reproduced. The apparent increase of the island density in the fifth layer, which starts to differ slightly from the true island density, indicates the limits of our data analysis due to the simultaneous growth of C_{60} layers. The vertical layer filling and roughening are also highly consistent, as can be seen from the good agreement between experimental and simulated evolution of anti-Bragg intensity in Figure 4.12c and 4.12d.

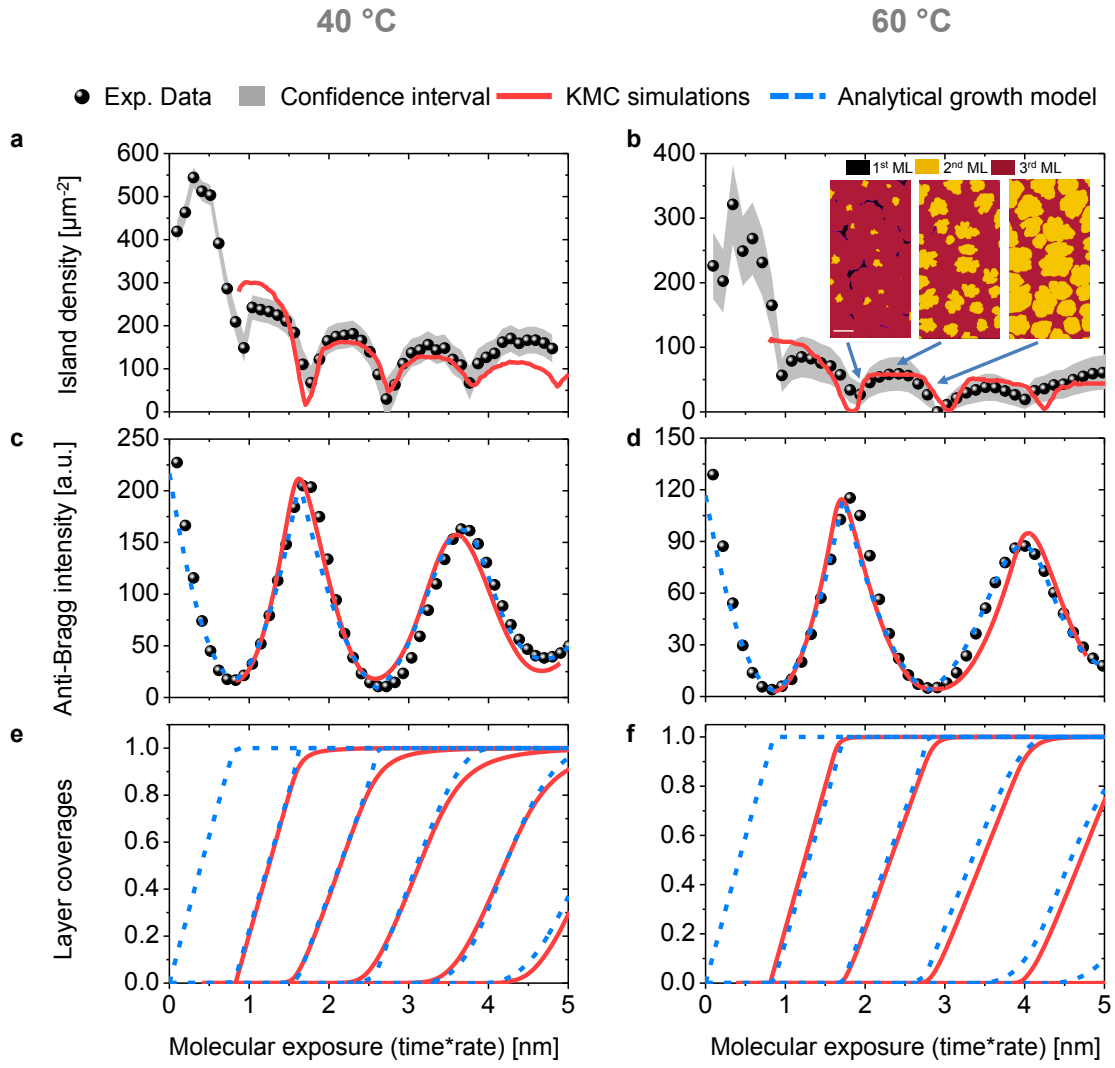

Figure 4.12: Excellent agreement between experimental and simulated measures of surface morphology. (a)+(b) Island density (inset in (b): 2D island growth regimes as simulated by KMC (created by N. Kleppmann); scale bar: 100 nm), (c)+(d) anti-Bragg growth oscillations and (e)+(f) layer coverages are shown as a function of the molecular exposure for C_{60} films grown at $T = 40$ °C $T = 60$ °C and $f = 0.10$ ML/ min. The anti-Bragg growth oscillations and the layer coverages include data from an analytical growth model. The KMC simulations have been performed from the second layer onwards. The confidence interval in (a) and (b) are calculated from the experimental uncertainties. KMC data simulated by N.Kleppmann(TUB).

As an independent confirmation of the KMC results the mean-field analytical model for thin film growth of Trofimov et al. and Woll et al.(see [108, 110, 111]) has been used,

the results of which agree with the layer coverages of the KMC simulations, as can be seen in Figure 4.12e and 4.12f.

Island shapes in experiment and simulation In all cases, compact island shapes have been observed in the simulations (see the inset in Figure 4.12b) as well as in the experiments. In general, the island shape can be obtained from the shape of the diffuse x-ray scattering (GISAXS) as the scattered intensity is composed of the structure factor (average island distance) and the form factor (island shape) of the thin film morphology.

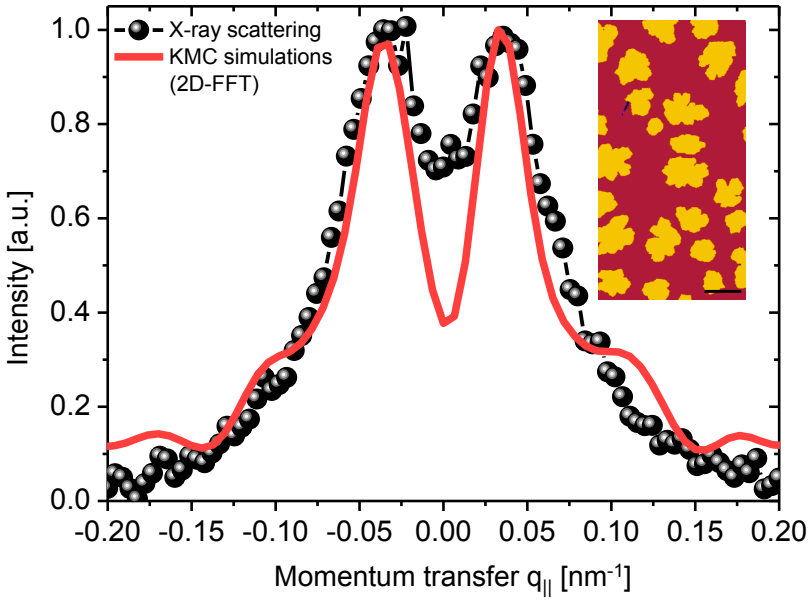

Figure 4.13: Island shapes in experiment and KMC simulations. Comparison of profile line graphs of the diffuse x-ray scattering and the fast Fourier transform (FFT) of the KMC simulated real-space morphology for a 3.5 ML C_{60}-film. Good agreement of the line graphs regarding the shape and the peak positions demonstrate agreement between island shapes in experiment and simulation. Inset: Corresponding KMC morphology (scale bar: 100 nm).

By assuming a certain island shape and (size) distribution of islands one can calculate the diffusely scattered intensity from this film morphology using dedicated programs like IsGISAXS [58, 164]. Here no island shapes have to be assumed, but the KMC data can directly be used to calculate the expected shape of the diffusely scattered intensity. In Figure 4.13 line graphs of the diffuse x-ray scattering and the Fourier transform of the real-space morphology for a 3.5 ML thin C_{60} film (60 °C, low deposition rate) are compared. The line graph of the FT was convoluted with the resolution function of the experiment (normalized Gaussian function with a FWHM of 0.01 nm^{-1}). There is

good agreement between the simulation and measurement, with only slight deviations due to experimental resolution limits. This finding supports the assumption that there are similar island shapes in experiment and simulation.

Even beyond the specific experimental parameters chosen in Figures 4.12a-f, KMC simulations show a good agreement with the experimental findings for all studied rates (0.1 ML/ min and 1 ML/ min) and the full experimental temperature range of 40 °C - 80 °C. This is seen in Figure 4.14, where we compare the experimental and simulated values for the maximum island density in the third monolayer.

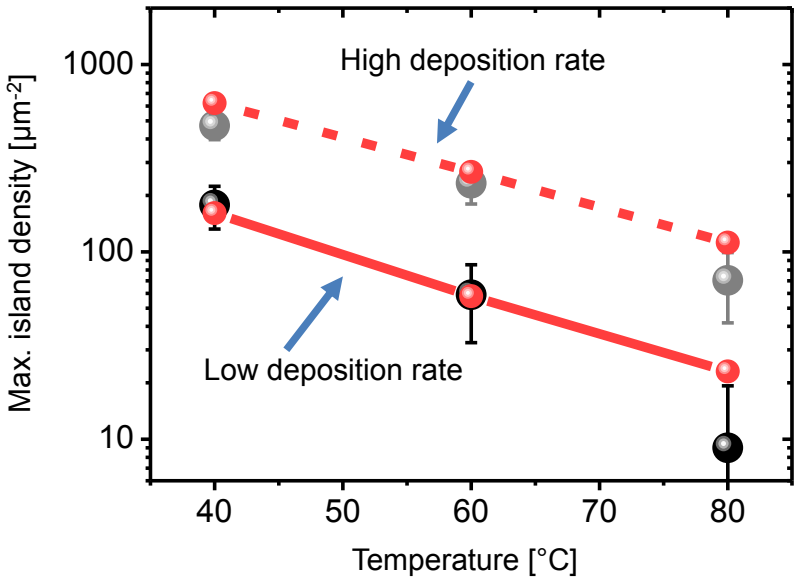

Figure 4.14: Good agreement between experiment and simulation for all studied growth conditions. Maximal island density for the third layer for both a low deposition rate of 0.1 ML/ min and a high deposition rate of 1 ML/ min as a function of temperature.

In accordance with growth theories predicting a scaling of island density with deposition rate/diffusivity [33, 47] (see equation 4.7), we find that the simulated and experimental island density decreases for higher substrate temperature and lower deposition rate by an order of magnitude. Furthermore, KMC simulations correctly predict the change in island density by almost two orders of magnitude when changing deposition rate and temperature. Notably, this comprehensive agreement of temperature-, rate- and time-dependent data has been achieved with a physical model of surface processes that contains only three parameters for the nanoscopic energy barriers for diffusion, nucleation and step-edge crossing. The resulting values are

- $E_D = (540 \pm 40)$ meV for the diffusion energy,

- $E_B = (130 \pm 20)$ meV for the lateral binding energy, and
- $E_{ES} = (110 \pm 20)$ meV for the step-edge/ Ehrlich-Schwoebel barrier.

Discussion on the mutual correlations of energy barriers and their error margins To adjust the parameters E_D, E_B and E_{ES} appearing in the energy barrier ($\Delta E_{i,j} = E_D + n_i E_B + s_{i,j} E_{ES}$) (see equation 4.9) we start from initial values suggested in the literature [35,40]. We then optimize the parameter set to match, as accurately as possible, the experimental data for the island density and the filling fraction at $T = 40$ °C/ $T = 60$ °C and $f = 0.1$ ML/ min. This experimental data set has the best lateral and temporal resolution. In performing such an optimization, we have to note that the influences of the different energy barrier contributions on our observables are strongly correlated. For example, E_D determines the free diffusion time and is therefore of prime importance for the calculated island density. The latter, however, is also influenced by E_B: If the neighbor energy is sufficiently small, island nuclei can dissociate, which effectively reduces the island density. Therefore the influence of E_D and E_B on the island is correlated. Another example occurs during step-edge crossing: The energy barrier of this process is given by E_{ES}. However, the effective crossing rate is also influenced by the island morphology (which determines the probability of reaching a step), and thus, by E_B. Due to this mutual influence it is clear that optimization of the energy parameters is rather challenging, one danger being that the resulting set may not be completely unique. We note, however, that the final parameter set selected in our study yields a satisfying match of the experimental data not only for the case $T = 40$ °C/ $T = 60$ °C and $f = 0.1$ ML/ min, but also at the other temperatures and adsorption rates considered. This "robustness" strongly supports our predictions. For the estimation of the error bars of the extracted energies their mutual correlation as well as the experimental confidence interval was taken into account. Notably, even a small alteration of one of the energy contributions (changes of the order of 20 meV) results in significant changes of the calculated morphology, i.e., in a deviation from experimental results. The confidence interval of the experimental island density data shown in 4.12a,b and in Figure 4.7 is calculated from the experimental uncertainties of x-ray wavelength, sample-to-detector distance as well as the fit uncertainty of the double peak distance in the diffuse x-ray scattering experiments. When we take the experimental confidence interval of the island density and anti-Bragg intensity into account, the error bar of the diffusion barrier increases to 40 meV. Please note, that the sensitivity of the binding energy E_B and the Ehrlich-Schwoebel barrier E_{ES} on the experimental measures is larger than for the diffusion energy. Therefore, the error bar for these energies already includes and covers the experimental confidence interval.

Comparison with reported C_{60} energy values It is instructive to compare the self-consistent parameter set obtained in this study to individual energy values reported earlier (no self-consistent set of all three energy parameters has been reported so far). The height of the C_{60} Ehrlich-Schwoebel barrier (110 meV) is comparable to atomic systems, such as Pt/Pt(111) (80 meV) [48] and is close to the value of 100 meV for C_{60} from recent DFT calculations by Goose et al. [40]. Our value for the binding energy, $E_B = 130$ meV, is smaller than that related to the minimum of the pair interaction potential of two C_{60} molecules, in particular the Girifalco potential, $E_{C_{60}-C_{60}} = 270$ meV, which has been derived theoretically [140,186] and has recently been measured in AFM experiments [187]. There are several factors contributing to this difference: First, we are considering molecules close to a substrate, which has not been taken into account in [140,186] but has already been shown to weaken the interaction [187]. Second, we are considering dense, and thus strongly correlated systems [66, 67], not two molecules in vacuum as assumed in [140, 186]. Third, and maybe most importantly, our value for the binding energy has been obtained such that experimental data are fitted over a range of temperatures. It is well known that effective potentials (and thus binding energies) can strongly depend on the temperature [188]; thus our value has to be considered as a temperature average. Finally, we stress that our value for E_B is very close to an estimate gained from the cohesion energy per neighbor of C_{60} in its bulk fcc crystal, $E_C = 133$ meV (This is the total cohesion energy 1.6 eV [189,190] divided by the 12 bulk lattice neighbors). Regarding our value for the diffusion barrier ($E_D = 540$ meV), we note that this is significantly larger than the corresponding value derived from a potential landscape analysis, $E_{pot} = 168$ meV [191]. This is likely due to the fact that in our KMC simulations we do not consider all energy minima as lattice sites. Thus, the travelled distances across several minima are larger, leading effectively to a larger barrier.

Körner et al. [37] and Liu et al. [35] report a free diffusion energy of $E_2 \approx 0.178$ eV; however,they also use an attempt frequency of $\nu_0 = 2 \cdot 10^{11}$ Hz. Moreover, both studies have been performed on a hexagonal lattice and consider the interstitial sites. In our simulations, we neglect these interstitial sites and only take into account fcc lattice sites. Without that coarse-grained approach it would not be possible to simulate such a large system for minutes to hours of experimental time. In the performed KMC simulations a particle overcomes the barrier $E_2 \approx 0.178$ eV twice in one diffusion step. Notably, there are three diffusion options from the interstitial site, but only one option leads to our coarse-grained destination site. Consequently, an additional geometric factor of 1/3 needs to be included in the diffusion rate. In addition, taking the difference in the attempt frequency ν_0 into account, the following estimate of a coarse-grained free diffusion barrier

from the values reported in [35, 37] can be made

$$E_D \approx -ln\left(\frac{1.4 \cdot 10^{13}}{2 \cdot 10^{11}}\right) k_B T - ln\left(\frac{1}{3}\right) k_B T + 2 \cdot 0.178 \text{ eV} \approx 0.51 \text{ eV}. \tag{4.10}$$

This value lies within the error margins of our value E_D. This estimate was obtained using $T = 60$ °C.

Additionally, we cannot exclude stacking faults and domains in the epitaxial C_{60} adlayers, which could contribute to a larger effective diffusion barrier in our calculation as transport across domain boundaries is hindered. Furthermore, the coarse-grained strategy is used in simulations of metallic growth [48, 192, 193] enabling a comparison with these studies.

4.3.3 Nanoscopic understanding of molecular growth: summary

- Comparison of vertical and lateral information on the multilayer growth of the fullerene C_{60} with kinetic Monte-Carlo (KMC) simulations,
- first quantification of the surface processes such as diffusion, lateral binding and step-edge crossing during multilayer growth of the fullerene C_{60},
  - $E_D = (540 \pm 40)$ meV for the diffusion energy,
  - $E_B = (130 \pm 20)$ meV for the lateral binding energy, and
  - $E_{ES} = (110 \pm 20)$ meV for the step-edge/ Ehrlich-Schwoebel barrier.
- Predictive simulations of C_{60} nanomaterials possible.

4.4 Particle-resolved dynamics reveal impact of short-range interactions on diffusion and step-edge crossing

In addition to the quantities discussed so far, KMC simulations allow us to extract single-particle trajectories and, thus, to study the dynamics on a particle level, which is not yet possible with current experimental techniques.

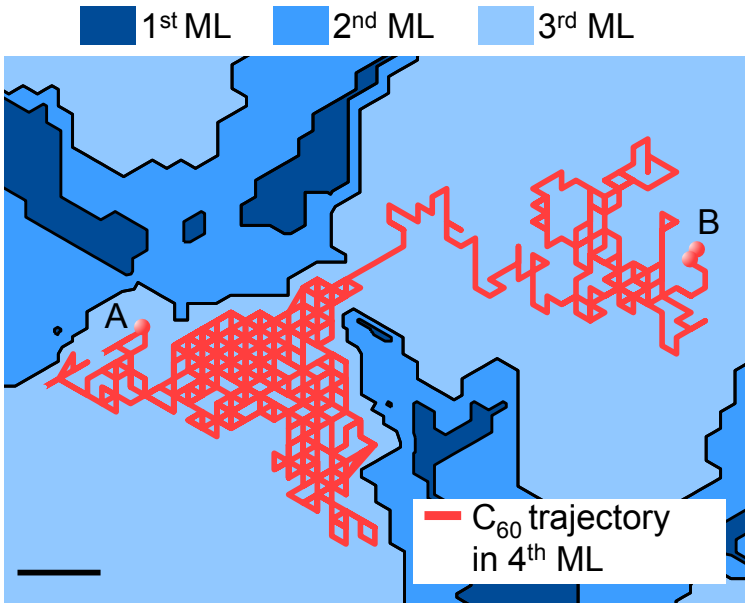

Figure 4.15: Particle-resolved dynamics during C_{60} growth. Trajectory of a single molecule in the 4^{th} ML ($T = 40$ °C and $f = 1$ ML/ min; scale bar: 5 nm). The influence of the Ehrlich-Schwoebel barrier can be clearly seen as a caging of the single C_{60}-molecule on the island. The letters A and B denote the adsorption of one molecule on the surface (A) and the formation of a dimer (B). Data simulated by N. Kleppmann.

An example of a single C_{60} particle trajectory (red) on top of a 3^{rd} monolayer island (light blue) is shown in Figure 4.15. Clearly, the Ehrlich-Schwoebel barrier leads to a "caging" of the C_{60} molecule close to the borders of the island, i.e. the standard random walk behavior is restricted by the step-edge of the island.

4.4.1 C_{60} surface diffusion resembles colloidal systems

Importantly, the particle-resolved dynamics reveal crucial differences in the diffusion behavior of C_{60} and atomic systems. For C_{60} on $C_{60}(111)$ the diffusion barrier E_D is relatively large compared to the binding energy E_B. Specifically, the ratio

$$R = \frac{E_D}{E_D + E_B} \tag{4.11}$$

is R=0.83. This is significantly larger than in typical atomic systems, such as Pt on Pt(111), where $R \approx 0.29 - 0.34$, or Ag on Ag(111) with $R \approx 0.29 - 0.39$ [47, 48]. Note, that we compare a coarse-grained diffusion energy E_D with KMC studies of metals where also coarse-grained approach was chosen. We suggest that this pronounced difference is related to the relatively short attractive interaction range of C_{60}, as compared to the attraction range of atoms, if normalized to their respective size (see Section 2.3.1 for details on the interaction range of C_{60}). The comparatively large ratio R for C_{60} has a profound impact on the mobility of the particles. This is shown in Figure 4.16, where the mean-squared displacement

$$MSD = |\boldsymbol{r}(t) - \boldsymbol{r}(0)|^2 \tag{4.12}$$

has been plotted for particles arriving between islands after the growth of 1.5 monolayers for C_{60} and for a system with an atom-like ratio $R = 0.34$.

Calculation of MSD for atomic-like systems The isolation of the role of neighbor interactions on the growth of representative atomic systems relative to C_{60} growth within the performed KMC simulations has been done in the following way: The KMC simulations for atom-like systems has been performed with the values of the diffusion energy E_D, the Ehrlich-Schwoebel barrier E_{ES} for C_{60} , with the same lattice configuration and the experimental deposition rate and temperature.

However, the value for the lateral binding energy E_B of the atomic system has been varied in a way that the ratio $R = \frac{E_D}{E_D+E_B}$ fulfills the literature values of $R \approx 0.34$ for elemental atomic systems like Pt ($R \approx 0.29 - 0.34$) or Ag ($R \approx 0.29 - 0.39$) [48]. Analyzing systems that are identical in all parameters except the ratio R allows us to directly compare the single-particle dynamics despite the smaller time- and length scales of growth in atomic systems relative to C_{60}. Clearly, this strategy is not suited to make predictive simulations of the growth of the atomic systems, but it does enable us to determine the influence of the difference in range of attractive interactions.

The linear increase with time of the C_{60}-MSD in the very beginning corresponds to free

diffusion, depicted in grey, as the molecules perform a random walk on the underlying fcc(111)-surface. After a time of about 0.1 ms, encountering an upward island edge as well as interactions with neighbors hinder the diffusion of the molecules, the MSD saturates. Similar sub-diffusive behavior also occurs in the atom-like system, but at much shorter times. This is because atoms can form new bonds more quickly due to the longer range of atomic interactions and the stronger binding energy.

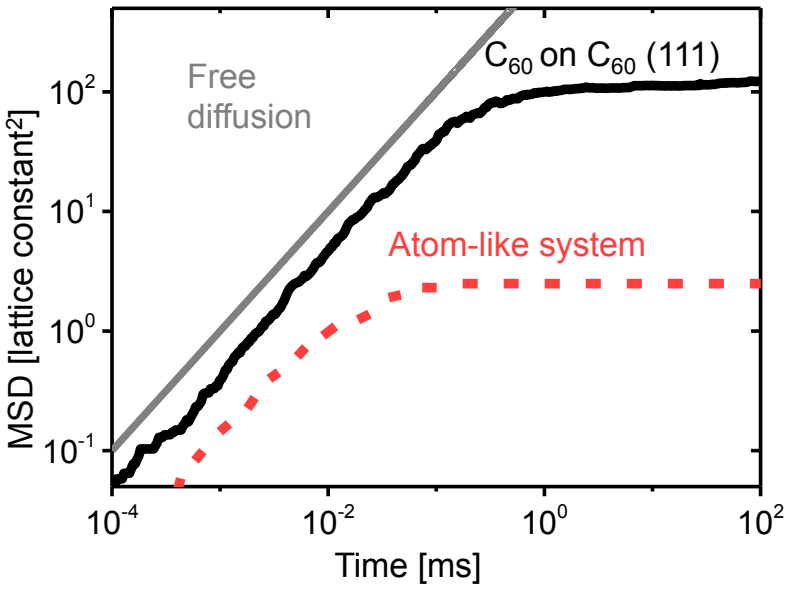

Figure 4.16: Larger free diffusion times for C_{60} compared to atom-like systems. Mean-Square displacement $MSD = |\boldsymbol{r}(t) - \boldsymbol{r}(0)|^2$ of C_{60} on $C_{60}(111)$, for $T = 60$ °C and $f = 0.1$ ML/ min as a function of time spent on the surface. Results are averaged over 500 realizations. The particles considered arrive in the 2^{nd} ML after the growth of 1.5 monolayers. For comparison, we show data for a system with atom-like ratio $\frac{E_D}{E_D+E_B} = 0.34$. Note that the quasi-free diffusion of C_{60} extends substantially further than for atom-like systems, even if scaled by the lattice parameter, signifying the qualitatively different behavior of C_{60}.

As a result, a C_{60} molecule is able to explore an area that is nearly two orders of magnitude larger than in the atom-like system before it is immobilized. This specific behavior of surface diffusion resembles colloidal systems. The shorter range of attractive interactions for colloids lead to a better surface diffusion and a weaker lateral binding.

4.4.2 Real energetic step-edge barrier for C_{60}

The different diffusion behavior of C_{60} prompts the question on the nature of the Ehrlich-Schwoebel barrier in comparison to atomic and colloidal growth. Indeed, regarding their narrow interaction range, C_{60} "nano-colloids" are more similar to colloids than atoms. In colloids the range of attractive interactions is so small that the reduced coordination associated with an edge is not "sensed". This effectively leads to the vanishing of an energetic barrier at the edge. Instead, one observes a purely diffusive Ehrlich-Schwoebel barrier in colloids arising from a lower diffusion probability along the geometrically longer path across the step-edge [50]. In contrast, for atoms crossing an island edge is associated with an energetic Ehrlich-Schwoebel barrier, as bonds are missing at a step-edge.

For C_{60} we can estimate an upper bound for a diffusive barrier based on the waiting time of a typical hopping process. The subsequent argumentation closely follows that given by Ganapathy et al. [50] for colloidal systems. We consider a C_{60} particle moving on a surface formed by other C_{60} particles. As a consequence of the short range of interactions the traveling particle tries to be in constant contact with two other particles. This effectively reduces local transport to a one-dimensional (1D) motion along a straight path, along which the potential landscape can be assumed to be constant. We note that the length of the 1D path between binding sites (d_{island}) on an island is smaller than that of a path crossing the step-edge (d_{step}), see Figure 4.17 for an illustration of such paths.

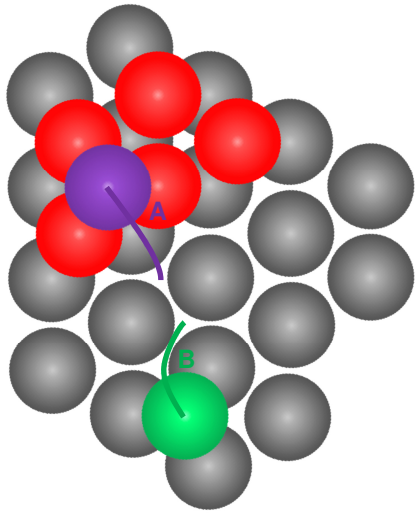

Figure 4.17: Sketch of diffusion paths. Diffusion paths during (A) step-edge crossing processes and (B) between neighboring sites.

Therefore, the travel time for a step-edge jump can be up to a factor of $\frac{<t_{step}>}{<t_{island}>}$ =

$\left(\frac{d_{step}}{d_{island}}\right)^2$ longer, where $< t >= 1/r$ with r as the Arrhenius-type rate describing the surface processes [194] in equation 4.9. Associated with this increase in diffusion time along the 1D potential is an increase of the probability to return to the original site [195]. As a consequence, the step-edge crossing probability effectively decreases. This consideration leads to an effective, geometrical Ehrlich-Schwoebel barrier $E_{ES,geo}$ determined by

$$E_{ES,geo} = ln\left(\left(\frac{d_{step}}{d_{island}}\right)^2\right) \cdot k_B \cdot T. \tag{4.13}$$

To quantify this geometry-induced energy contribution, we recall that our KMC simulations are based on a triangular lattice. The value for $\frac{d_{step}}{d_{island}}$ is based on the considerations made in the supplemental material of Ganapathy et al. [50], where they found for a hexagonal lattice that the path-length of local motion in a 1D potential along the path crossing a step-edge (see A in Figure 4.17) is 2.8 times as long as the path-length involving diffusion between neighboring sites (see B in Figure 4.17). Since our simulation is restricted to a triangular lattice, an in-plane diffusion process involves two nearest-neighbor steps. This results in the ratio $\frac{d_{step}}{d_{island}} = \frac{b}{2a} = \frac{2.8a}{2a} = 1.4$. Combining this result with equation 4.13 we obtain a diffusive pseudo-barrier of

$$E_{ES,geo} = ln(F) \cdot k_B \cdot T < 50 \text{ meV}. \tag{4.14}$$

This is markedly smaller than the value of 110 meV obtained from the KMC simulations. We thus conclude that the Ehrlich-Schwoebel barrier in C_{60} surface growth is, at least partially, of energetic character, consistent with the intermediate range of the C_{60}-interactions (which lies between the range of colloidal and atomic interactions). This is schematically shown in the energy landscapes for atoms, colloids and C_{60} in Figure 4.18.

4.4.3 Summary: particle-resolved dynamics for the fullerene C_{60}

- Longer surface diffusion times before immobilization at existing islands compared to atomic systems due to colloid-like, short-ranged character of C_{60}-interactions,
- real energetic step-edge barrier for C_{60} similar to atoms but in contrast to colloidal systems with their purely diffusive barrier.

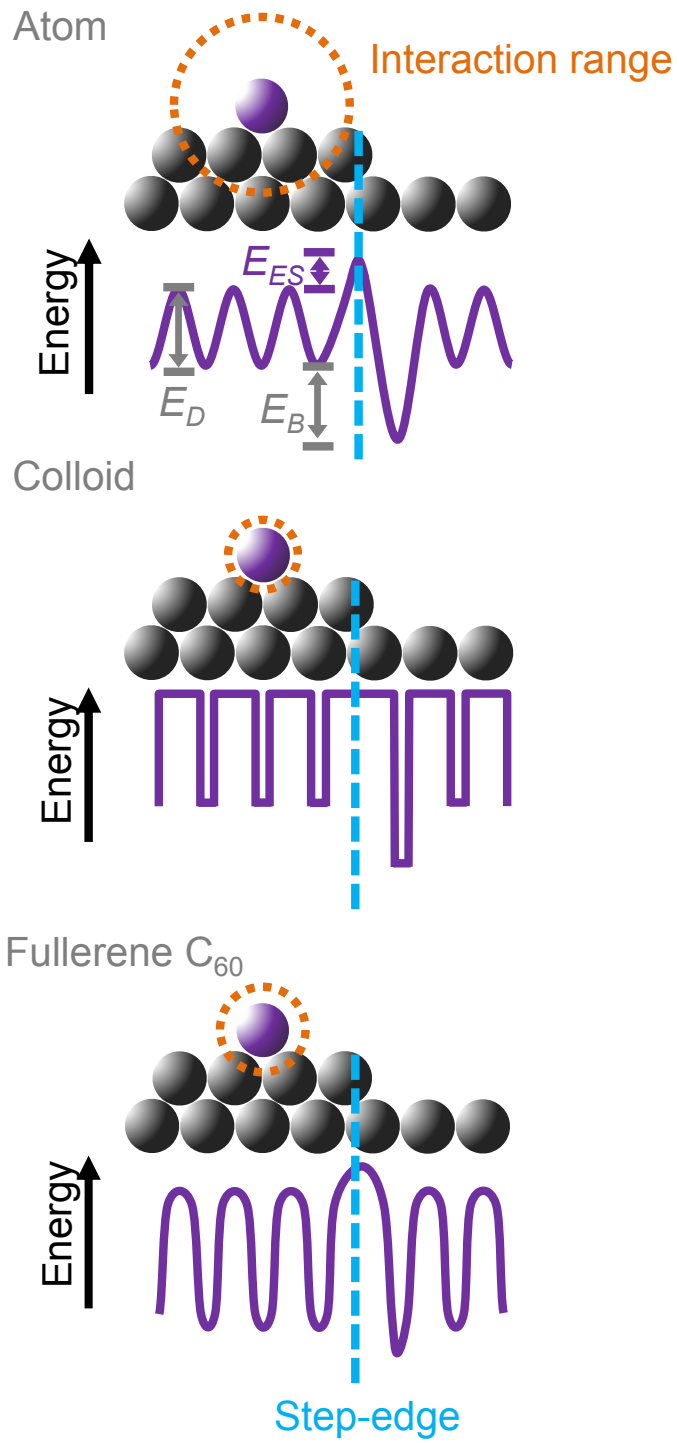

Figure 4.18: Schematic illustration of energy landscape for atoms, colloids and the fullerene C_{60} near an island step-edge. The interaction range of the different materials clearly affects the character of step-edge barrier as one can distinguish between real and a diffusion-mediated pseudo-barrier [50].

4.5 Post-growth reorganization of C_{60} films on mica

In the last sections the growth of the fullerene C_{60} has been followed in real-time and *in situ* with x-ray scattering methods in reciprocal space. Real-space information has been obtained by using KMC simulations. The route of using scanning probe microscopy to image the growth is not suited for C_{60} on mica as post-growth dewetting appears, which is discussed in this section.

4.5.1 Upward mass transport in the post-growth regime

In section 4.2.1.1 the fitting of the anti-Bragg growth oscillations with the analytical growth model [109, 110] has been discussed. In Figure 4.19 the fitting of the anti-Bragg intensity as a function growth time for a substrate temperature of 60 °C and a deposition rate of 1 Å/min, is shown.

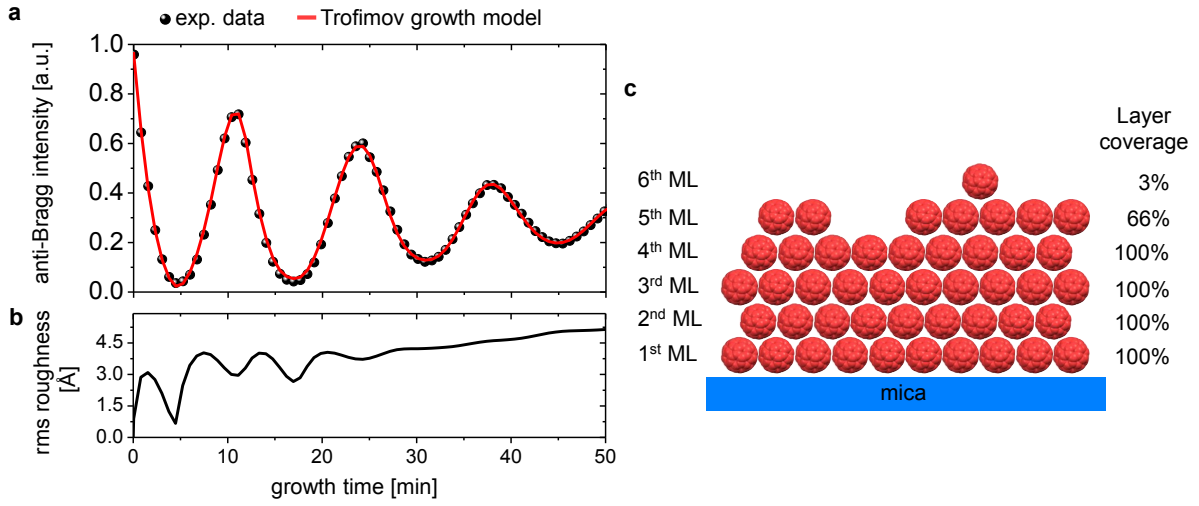

Figure 4.19: Smooth layer-by-layer growth of C_{60} on mica. (a) *In situ* x-ray scattering shows smooth layer-by-layer growth of C_{60} on mica, (b) rms thin film roughness and (c) illustration of layer coverage.

Information not only about the layer coverages but also about the root-mean-square(rms) roughness σ_{rms} for each layer and at each time [111] can be derived:

$$\sigma_{rms}(t) = \sqrt{\sum_{n=0}^{\infty}(\theta_n(t) - \theta_{n+1}(t)) \cdot (d \cdot n - \bar{d}(t))^2}. \tag{4.15}$$

In Figure 4.19b the film roughness in nm as a function of time is shown. The first three monolayers grow in a nearly perfect layer-by-layer fashion, indicated by the distinct

oscillating behavior in the film roughness. The film gets rougher until the monolayer is half-filled and then the roughness decreases when coalescence fills any remaining holes in the ML. Once layer-by-layer growth breaks down and more than one ML grow simultaneously the film roughness increases. Such a roughness increase is observed after three monolayers as indicated by the damped growth oscillations. However, the absolute film roughness of approx. 4.5 Å (approx. 1/2 ML) for the 8^{th} ML shows that the molecular thin film nevertheless is extraordinarily smooth. The extracted layer coverages give quantitative information on the nucleation of different layers. The layer coverage for a later growth stage is illustrated in Figure 4.19c. At a nominal thickness of 4.5 ML (28 min) only the 5^{th} and the 6^{th} monolayer grow simultaneously.

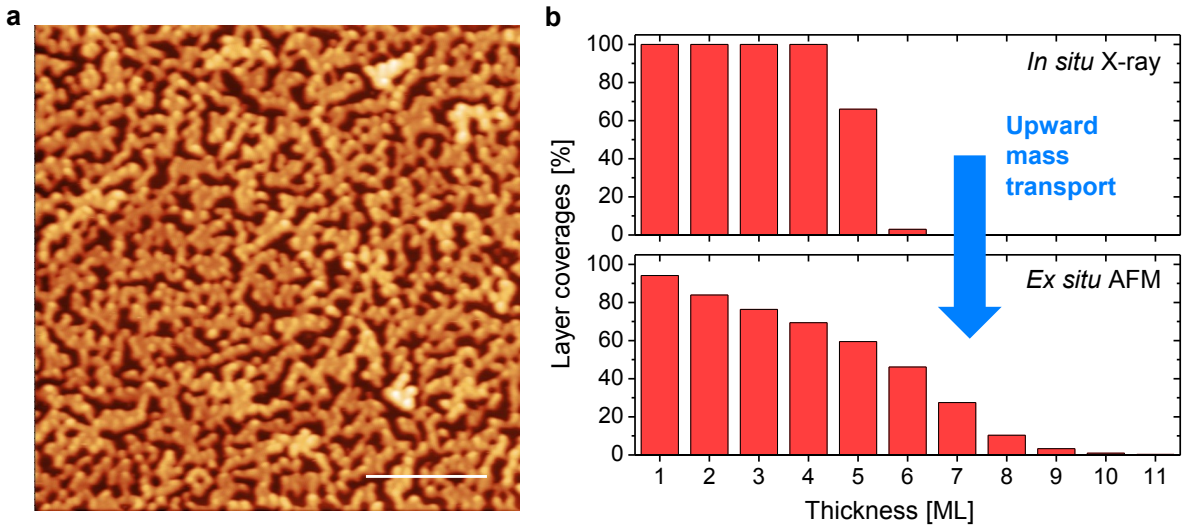

Figure 4.20: Post-growth upward mass transport. (a) *Ex situ* AFM image, which was taken 12 h after the growth, shows a rough film (rms roughness of the AFM topography: 2.4 nm) being contrary to the results of the *in situ* x-ray scattering. (b) compares histograms of the layer coverages from the *in situ* and *ex situ* experiments showing that upward mass transport have to be occurred.

Beside the real-time x-ray scattering we apply real-space methods to get information on the thin film morphology ex situ. In Figure 4.20a a room temperature AFM image of a 4.5 ML C_{60} film on mica made 12 h after the deposition at 60 °C with 1 Å/min is shown. Surprisingly, instead of a smooth molecular film with only 5^{th} and the 6^{th} layer exposed as expected from the anti-Bragg growth oscillations a rough film full of islands and grooves in between is observed. The rms-roughness of the AFM topography is 2.4 nm and, hence, is six times larger than the rms-roughness identified with the anti-Bragg growth oscillations. Figure 4.20b depicts histograms of the layer coverages of the *ex situ* AFM image compared with the layer coverage derived from the *in situ* x-ray experiments. The

histogram of the AFM image shows the formation of island with up to 10 ML thickness and a clear discrepancy between the *in situ* real-time growth experiment and the *ex situ* AFM image. Therefore upward mass transport of molecules onto islands has to occur after the deposition. In particular, the break-up of a smooth molecular film into crystallites or islands accompanied by an increase in roughness is observed.

4.5.2 Monitoring the post-growth dewetting in real-time: temperature-dependent upward mass transport

To answer questions regarding time-scales of post-growth reorganization/ dewetting and mechanisms driving the temperature-dependent post-growth dewetting behavior of C_{60} on mica has been investigated by monitoring the anti-Bragg intensity during and after the growth of the first monolayer. Figure 4.21 shows the anti-Bragg intensity (grey dots) for the temperatures of 40 °C, 60 °C and 80 °C during growth of the first monolayer and the post-growth dewetting. The anti-Bragg intensity drops down as the first molecules are deposited on the substrate. After the deposition of the first monolayer the growth was stopped. For all temperatures an increase of the anti-Bragg intensity after the deposition of one monolayer is observed. Due to post-growth dewetting a mass transport of molecules from the first monolayer into the second layer occurs, leading to an increase of the second layer coverage and, subsequently, of the scattered anti-Bragg intensity.

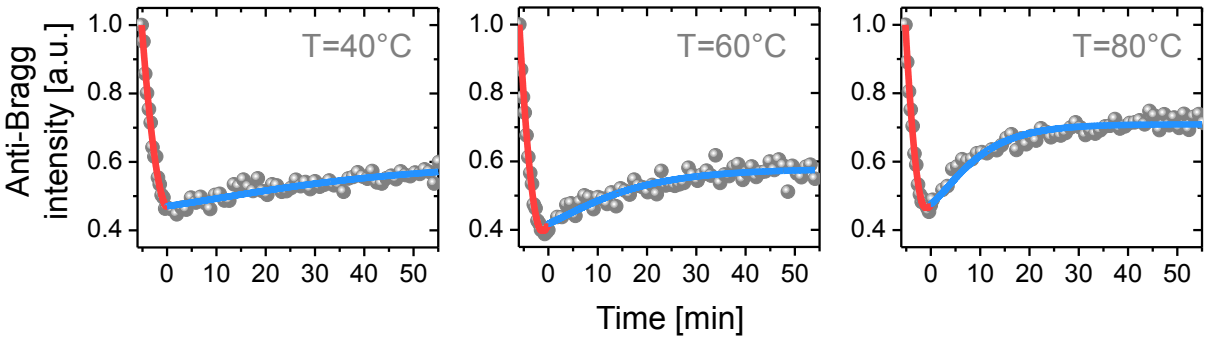

Figure 4.21: Temperature-dependent upward mass transport. The anti-Bragg intensity (grey dots) for the temperatures of 40 °C, 60 °C and 80 °C during growth of the first monolayer and the post-growth dewetting is shown. In red and blue the fits of the growth and the post-growth dewetting can be seen.

The growth is fitted by the analytical growth model. As we are only concerned with the first two monolayers, just the layer coverages θ_1 and θ_2 are considered and we assume a constant amount of molecules during and after the growth ($\theta_0 = \theta_1(t) + \theta_2(t)$) neglecting

desorption processes [196]. The temporal evolution of the dewetting process is assumed to be described by an exponential expression with a rate ν as it was already predicted by detailed theoretical considerations [197]. As the dewetting process is the driving force the second layer coverage can be written as

$$\theta_2(t) = \theta_2(\infty) - (\theta_2(\infty) - \theta_2(0)) \cdot exp(-\nu t) \tag{4.16}$$

with $\theta_2(\infty)$ being the saturation coverage of the second layer after the dewetting and $\theta_2(t = 0)$ being the value for the initial coverage before dewetting. Importantly, the scattered anti-Bragg intensity of the post-growth dewetting phase can be fitted using

$$I_{ab}^{dewetting}(t) = |A_{sub}\, exp(i\phi_{sub}) - F_{mol} \cdot [\theta_1(t) - \theta_2(t)]|^2 \tag{4.17}$$

The substrate amplitude A_{sub} , the substrate phase ϕ_{sub}, the molecular form factor F_{mol} as well as the overall amount of molecules θ_0 and the initial coverage of the second monolayer before dewetting $\theta_2(0)$ can be easily taken from the fitting of the first-layer growth. Thus, the rate ν and the saturation second layer coverage $\theta_2(\infty)$ remain as fitting parameters for dewetting. In Figure 4.21 the fitting of the growth (red) and the dewetting (blue) is shown for three temperatures. We can directly calculate the upward mass transport rate, which is maximal at $t = 0$. The different upward transport rates are summarized for the three applied temperatures in Table 4.1 and ranging from 0.007 ML/min for 40 °C to 0.033 ML/ min for 80 °C. An increase of 40 K leads to an almost five times larger upward mass transport from the first into the second layer.

Temperature T	Upward transport [ML/ min]	Time-rate ν [1/min]
40 °C	0.007	0.03
60 °C	0.014	0.08
80 °C	0.033	0.13

Table 4.1: Parameters for C $_{60}$ dewetting

This result is also confirmed by the temperature-dependent rate ν, which mirrors the dewetting kinetics and shows that dewetting occurs on a time-scale of 8 min (80 °C) to 33 min (40 °C) in this temperature-range and for the applied deposition rate.

Therefore, a thermally-activated mass transport from the first into the second monolayer occurs, which can be described by an Arrhenius type behavior (see Figure 4.22b)

$$\nu = \nu_0 exp\left(-\frac{E_{act,eff}^{dewetting}}{k_B T}\right) \tag{4.18}$$

From fitting the rate ν as a function of the inverse temperature, we estimate an effective activation barrier $E_{act,eff}^{dewett}$ for C_{60}-dewetting to (0.33 $\pm$ 0.14) eV.

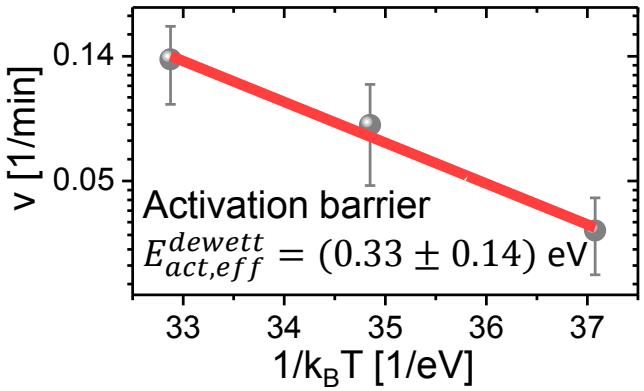

Figure 4.22: Effective activation barrier for C_{60} dewetting. From fitting the rate ν as a function of the inverse temperature, an effective activation barrier $E_{act,eff}^{dewett}$ for C_{60}-dewetting has been quantified to (0.33 $\pm$ 0.14) eV.

4.5.3 Nanoscopic processes activating post-growth dewetting

Generally, two competing nanoscopic (and thermally-activated) processes with opposing trend occur during post-growth dewetting, the downward transport of molecules from a C_{60} island to the mica and the upward transport of molecules from mica to the top of a C_{60} island. These processes are characterized by a downward energy barrier $E_{downward}^{C_{60},C_{60}}$ and by an upward energy barrier $E_{upward}^{C_{60},mica}$, which molecules have to overcome for descending or ascending the step-edge as illustrated in the energy landscape in Figure 4.23. Therefore, the expression for the rate ν could be rewritten in the framework of the transition state theory [198, 199]

$$\nu = \nu_0 \left(exp\left(\frac{E_{C_{60},mica}^{upward}}{k_B T} \right) - exp\left(\frac{E_{C_{60},C_{60}}^{downward}}{k_B T} \right) \right) \tag{4.19}$$

The transition state theory does not allow a descended molecule to ascend back. The downward energy barrier $E_{C_{60},C_{60}}^{downward} = 0.29$ eV arises from the diffusion barrier of 0.18 eV [35] and the Ehrlich-Schwoebel barrier of 0.11 eV [112] for C_{60} on C_{60}. Importantly, this enables us to deduce the upward transport barrier for C_{60} molecules to ascend from mica on top of a C_{60} island to 0.28 eV. Regarding a single molecule C_{60} this energy results in a very low energy per C atom of 5 meV, which is only 1/6 of $k_B T$ for the applied

temperatures, demonstrates the high temperature sensitivity of the involved molecular processes. Note, C_{60} molecules ascending a step-edge have to spend (most likely) no energy in breaking lateral bonds. Due to their short-interaction range [65] the single C_{60} molecule tends to be in constant contact with their nearest neighbors at all times, even during upward transport. Consequently, the observed upward transport barrier could be a measure for the sum of the diffusion energy of C_{60} on mica and the additional step-edge crossing barrier a molecule has to overcome for ascending the step-edge.

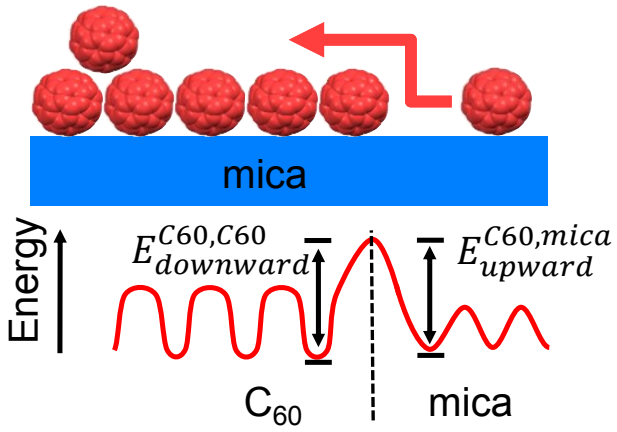

Figure 4.23: Energy landscape for descending and ascending a step-edge. Two competing nanoscopic (and thermally-activated) processes with opposing trend occur during post-growth dewetting, the downward transport of molecules from a C_{60} island on the mica and the upward transport of molecules from mica on top of a C_{60} island.

Importantly, for discussing the reason for post-growth dewetting to appear the non-equilibrium character of growth, which is due to the continuous molecular exposure impinging the surface (even at our low deposition rate), has to be considered. Therefore, it is possible that the favored film structure changes from layered film during growth to islands in the equilibrium, which could have different reasons. First, this could be attributed to the appearance of lattice strain. Molecules tend to form islands in the thermal equilibrium as island structures are often energetically more favorable than closed layers. This could also be a reason for post-growth dewetting of C_{60} on mica, as a lateral lattice mismatch of 3.8 % has been observed between C_{60} and mica lattice planes (see section 4.1.2 or reference [200]). Second, a change in surface energy after the growth due to the absence of molecular exposure could initiate a transition from layer to island growth. This spontaneous dewetting after growth was proposed by S. Burke et al. [70, 71] for C_{60} on alkali halides surfaces. Our results, in which smooth multi-layer films of C_{60} are built up in a layer-by-layer fashion during growth and, once the growth is stopped, the thin film

morphology changes completely, could eventually be an evidence for such an anomalous growth behavior.

4.5.4 Summary: Temperature-dependent post-growth dewetting for C_{60} on mica

- Thermally activated post-growth dewetting behavior for the first monolayer,
- an increase of 40 K of the substrate temperature leads to a five-times faster upward mass transport,
- from temperature-dependent measurements an effective activation barrier for upward interlayer transport of (0.33 ± 0.14) eV has been derived.

4.6 Summary: Unravelling the multilayer growth of the fullerene C_{60}

- **First determination of energy barriers for molecular surface processes during growth (see Figure 4.24)**

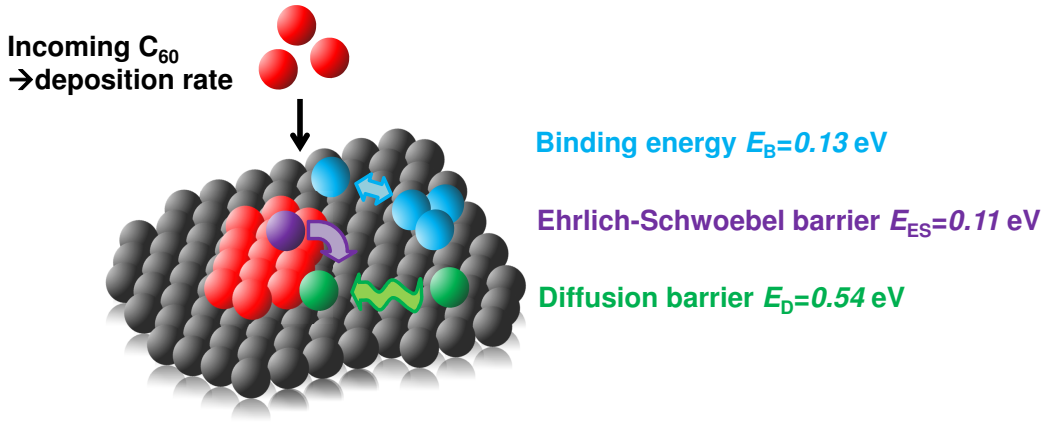

Figure 4.24: Surface processes during the growth of the fullerene C_{60}. The lateral binding characterized by the lateral binding energy E_B, the interlayer diffusion across a step-edge (Ehrlich-Schwoebel barrier E_{ES} and the diffusion barrier (E_D) are the major processes on the surface during growth.

- **Various dynamical aspects accompany the growth**
  - The colloid-like, short-ranged character of C_{60}-interactions leads to relatively long surface diffusion times before immobilization occurs at existing islands,
  - nevertheless, the step-edge crossing barrier of C_{60} differs from colloids in that it is not a pseudo-step-edge barrier arising from lower diffusion probability at a step-edge, but a true energetic barrier as observed for atoms,
  - the findings will help to gain insight into island nucleation and surface growth processes for van-der-Waals bound molecules between the scales of atomic and colloidal systems.
- **This quantitative, scale-bridging understanding enables predictive simulations and a rational choice of growth conditions ultimately leads to optimized design of functional materials**
- **Temperature-dependent post-growth dewetting of the fullerene C_{60} on mica**

- An increase of 40 K of the substrate temperature lead to a five-times faster upward mass transport,
- from temperature-dependent measurements an effective activation barrier for upward interlayer transport of (0.33 ± 0.14) eV has been derived.

5 Negative thermal expansion and temperature-controlled cooperative rotational motions of PTCDI-C_8

Mechanoresponsive supra-molecular assemblies have attracted increasing attention because of their potential in data storage [73], bio-nanotechnology [74] and molecular scale mechanics [75–80]. These materials show the ability to respond to the external stimuli like heat or irradiation of light by mechanoresponsive processes on the molecular and/or supra-molecular level. To translate molecular motions to macroscopic levels many molecular building blocks within a highly crystalline material must be able to alter cooperatively. These cooperative mechanical motions on the nanoscale can be found in materials with large positive and, especially, negative thermal expansion (NTE) [82–84].

NTE materials, for which the interatomic/ intermolecular distances contract upon heating, can be found for liquids like water in the temperature range of $0-4$ °C, for inorganic materials like metal oxides [85–87] and metal-organic frameworks (MOFs) [88, 89]. For metal oxides and MOFs (correlated) translational-rotational motions [87,88] of compound-subgroups as a function of temperature, which are caused by transverse vibrations [82], lead to a NTE within the crystalline material. Only a few purely organic NTE materials such as polymers [75] and organic single crystals [90–93] are reported. In pentacene crystals negative thermal expansion is accompanied with a change in herringbone angle [93]. For dumbbell-shaped organic molecules it has been found that the molecular tilt (angle between long molecular axis and a crystal plane) decreases with temperature. This temperature-dependent behavior causes the a-axis to expand and the b- and c-axis to shorten with increasing temperature [91].

As organic crystalline materials are held together by weaker van-der-Waals, electrostatic and/or hydrogen-bonding forces [94, 95], which easily expand upon heating, the mechanisms giving rise to the NTE in organic materials are challenging. For molecules with asymmetric dimensions the additional vibrational and rotational degrees of freedom, but also the entropy of the entire system have to be considered for describing the thermally-activated cooperative molecular processes on the nanoscale.

In this chapter Grazing Incidence X-ray Diffraction (GIXD) is used to quantify the temperature-dependent surface crystal structure and the molecular packing of the asymmetric organic semiconductor PTCDI-C_8 [81] in a temperature range from −60 °C to 140 °C. The unit cell parameters as a function of temperature are deduced from the positions of the Bragg reflections. An advanced analysis of the the Bragg reflection intensities give rise to the molecular packing within the crystalline structure. From our analysis, a strong reversible impact of temperature on the unit cell parameters has been found. That results in extraordinary large thermal expansion coefficients of up to 140 parts per million (ppm)/K. Surprisingly, a negative thermal expansion for organic thin film structures has been observed. The a-axis of the unit cell contracts upon annealing with a negative thermal expansion coefficient of −135 ppm/K. The negative thermal expansion for PTCDI-C_8 on SiO_2 can be understood by the continuous change of the rotational degrees of freedom of PTCDI-C_8 as a function of temperature. The molecules stand more up-right for larger temperatures resulting in a lowered a-axis and a increased c-axis length of the unit cell. From the perspective of thermodynamics, the interplay between increasing influence of molecular interactions for low temperatures leading to an ordered minimum energy crystal, on the one hand, and the rising impact of entropy with increasing temperature, on the other hand, may give rise to the reversibility of the structural properties.

The chapter is organized as follows: In the first section the temperature-dependent unit cell will be discussed. The second section deals with the 3D molecular orientations of PTCDI-C_8 deduced from molecular structure factor calculations. Finally, the observed results are discussed according to the intermolecular interactions and the impact of thermodynamics.

5.1 Temperature-dependent crystal structure of PTCDI-C_8 thin films

To determine the crystal structure of PTCDI-C_8 film on SiO_2 Grazing Incidence X-ray Diffraction (GIXD) was performed at the MiNaXS beamline/ PETRA III (DESY) [169]. To reveal the impact of temperature on the molecular arrangement the thin film temperature has been varied between −60 °C to 140 °C during the experiments. In a first run the temperature has been decreased from 140 °C to −60 °C and in a second run increased again up to 140 °C afterwards with a step size of 20 °C. In Figure 5.1 the corresponding GIXD measurements for the starting temperature of 140 °C (1^{st}) (Figure 5.1a), −60 °C (Figure 5.1b) and the final temperature of 140 °C (2^{nd}) (Figure 5.1c) as a function of the of the vertical and lateral momentum transfer $q_\perp$ and $q_{||}$ are shown for a 15 nm thin PTCDI-C_8 film on SiO_2.

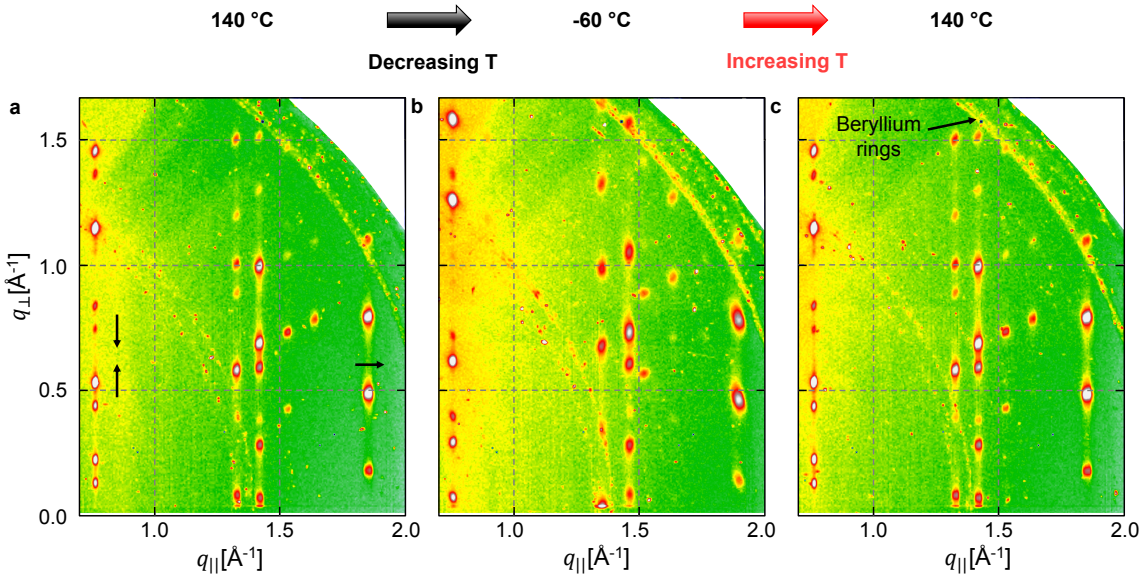

Figure 5.1: Temperature-dependent Grazing Incidence X-ray Diffraction (GIXD) measurements. GIXD for a) 140 °C, b) for -60 °C and c) for 140 °C again. A clear dependence of the positions of Bragg reflections on the temperature can be seen. Interestingly, the change of Bragg reflection positions is reversible.

The reciprocal space images have been obtained from the raw data detector images using the transformation mechanism described in Section 3.1.4.2. The ring-like intensity in the diffraction image stems from the diffraction on the beryllium window, which is part of the portable UHV sample environment used in the experiments.

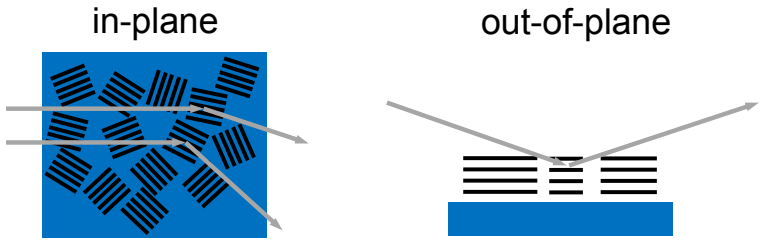

Figure 5.2: Illustration of 2D powder growth of PTCDI-C_8 on SiO_2. A random distribution of in-plane orientations, but a layered out-of-plane film structure has been observed.

For all employed temperatures six Bragg rods with up to 35 Bragg reflections have been observed indicating a highly crystalline organic thin film. Note, that not only a highly crystalline but also a smooth organic thin film indicated by distinct x-ray growth oscillations has been observed (see appendix A.1 for details).

The PTCDI-C_8 film on SiO_2 exhibits a random distribution of lateral orientations ("2D powder") as it is depicted in Figure 5.2. Nevertheless, a layered and textured vertical film structure has been observed indicated by Bragg reflections up to the 5^{th} order.

5.1.1 Reversible change of Bragg reflection position with temperature

In Figure 5.1 a reversible change of peak positions of Bragg reflections with temperature in the temperature range from −60 °C to 140 °C can be clearly seen.

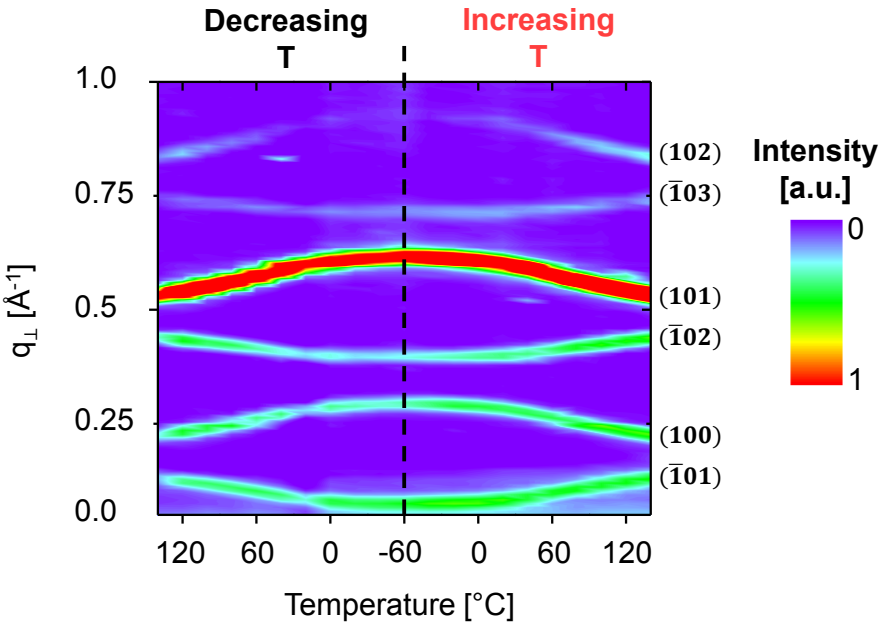

Figure 5.3: Reversible change of Bragg reflection position with temperature. 2D color plot of the Bragg reflections ($\bar{1}01$), (100), ($\bar{1}02$), (101), ($\bar{1}03$) and (102) as a function of the out-of-plane momentum transfer $q_\perp$ and all employed temperatures.

The in-plane as well as the out-of-plane momentum transfer $q_{||}$ and $q_\perp$ of several Bragg reflections change with temperature (see the arrows in Figure 5.1a). Interestingly, the change in Bragg reflection position is reversible as can be seen comparing Figure 5.1a and Figure 5.1c. For a more quantitative analysis the first Bragg rod at $q_{||} = 0.26$ Å^{-1} has been integrated from $q_{||} = 0.2$ Å^{-1} to $q_{||} = 0.3$ Å^{-1} and is plotted as 2D color plot. In Figure 5.3 the intensity of the six Bragg reflections ($\bar{1}01$), (100), ($\bar{1}02$), (101), ($\bar{1}03$) and (102) as a function of the out-of-plane momentum transfer $q_\perp$ can be seen for all applied temperatures. Figure 5.3 shows that the positions of all displayed Bragg reflections strongly depend on temperature. The position of Bragg reflection can reversibly

and continuously be tuned with temperature. For example, the position of the (101)-reflection, e.g., changes from $q_\perp = 0.53$ Å^{-1} at 140 °C to $q_\perp = 0.62$ Å^{-1} at −60 °C and returns to 0.53 Å^{-1} when increasing the temperature to 140 °C again. Interestingly, the Bragg reflection intensity also changes reversibly as can be clearly seen for the (102) reflection.

5.1.2 Anomalous thermal expansion: Reversible and continuous control of unit cell parameters

The change of the Bragg reflection positions as a function of temperature is caused by a change of crystal structure, in particular a change of the thin film unit cell (see equation 3.8). The unit cell parameters are deduced from the observed GIXD measurements using a formalism implemented by L. Pithan at the Humboldt-Universität zu Berlin [163].

Generally, the PTCDI-C_8 crystallizes in a triclinic crystal structure with one molecule per unit cell. In Table 5.1 the obtained unit cell parameters a, b, c, α, β and γ are displayed for the temperatures 140 °C (1^{st}), −60 °C and 140 °C (2^{nd}). From the dimensions of the unit cell of PTCDI-C_8 on SiO_2 with a large c-axis of 20.9 Å we deduce, that the PTCDI-C_8 molecule stands almost upright on the surface. In Figure 5.4 the Bragg reflection assignments based on the PTCDI-C_8 unit cell are shown. The unit cell is similar to the unit cell deduced by Krauss et al. [81] for PTCDI-C_8 thin films on sapphire.

UC parameter	140 °C (1^{st})	−60 °C	140 °C (2^{nd})
a	(8.9 ± 0.1) Å	(9.1 ± 0.1) Å	(8.9 ± 0.1) Å
b	(4.80 ± 0.03) Å	(4.70 ± 0.04) Å	(4.81 ± 0.04) Å
c	(20.9 ± 0.2) Å	(20.3 ± 0.5) Å	(20.9 ± 0.5) Å
α	(85.0 ± 0.4) °	(88.2 ± 0.4) °	(85.3 ± 0.4) °
β	(101.6 ± 0.3) °	(107.5 ± 0.4) °	(102.0 ± 0.4) °
γ	(67.1 ± 0.6) °	(66.4 ± 0.8) °	(67.2 ± 0.8) °

Table 5.1: Temperature-dependent unit cell parameters

However, the PTCDI-C_8 thin film unit cell differs from the bulk crystal unit cell ($a = 8.5$ Å, $b = 4.68$ Å, $c = 19.72$ Å, $\alpha = 91.57$ °, $\beta = 94.01$ °and $\gamma = 82.79$ °) [16]. The largest differences between bulk and thin film unit cell occur for the c-axis and the γ-angle. The differences could be attributed to the different energetics within thin film growth compared to single crystal growth as additional surface energies appear.

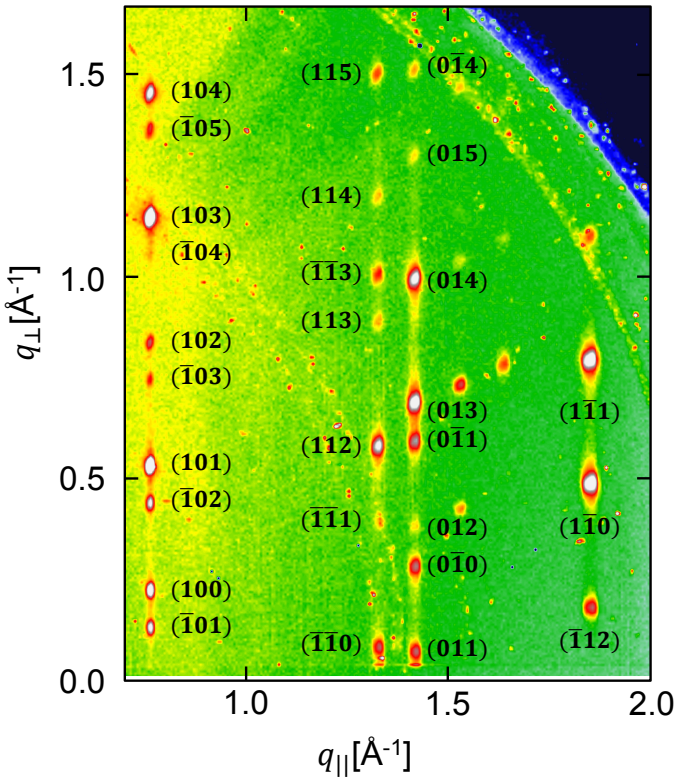

Figure 5.4: Bragg reflection assignments based on the presented PTCDI-C_8 unit cell. Please note, that only the most important assignments are displayed.

In Figure 5.5 the detailed evolution of all unit cell parameters as a function of decreasing (black) and increasing (red) temperature is shown. From the temperature-dependent unit cell parameters in Table 5.1 and Figure 5.5 a continuous and reversible change of the PTCDI-C_8 thin film structure with temperature is observed. To quantify the expansion with temperature the corresponding linear thermal expansion coefficient α has been estimated for the unit cell parameters a, b and c by

$$\alpha^{\{a,b,c\}} = \frac{\Delta\{a,b,c\}}{\Delta T}\frac{1}{\{a,b,c\}}. \tag{5.1}$$

The a-axis exhibits a large anomalous (negative) thermal expansion of $-(46 \pm 21)$ parts per million (ppm)/K for temperatures ranging from -60 °C to 20 °C and an even larger coefficient of $-(135 \pm 21)$ ppm/K from 20 °C to 140 °C. In contrast, the b- and c-axis shows an extraordinary large positive thermal expansion characterized by coefficients of 139 ppm/K and 136 ppm/K.

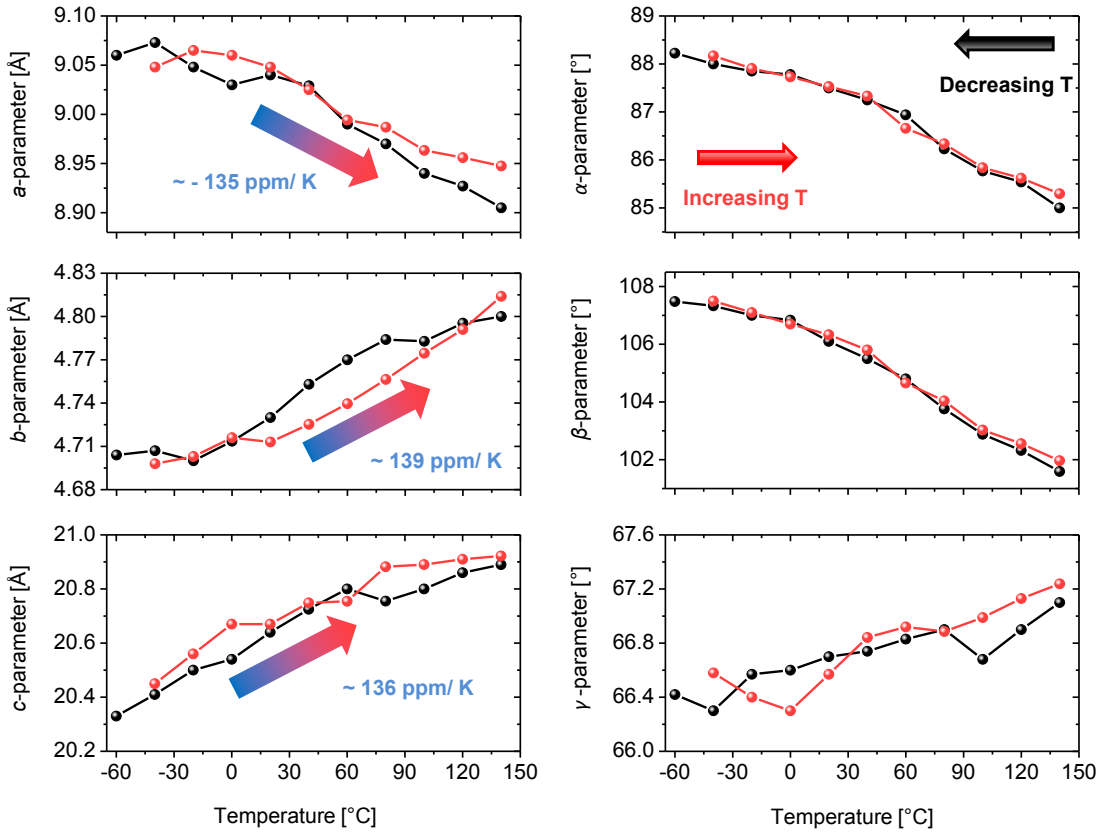

Figure 5.5: Reversible and continuous change of unit cell parameters with temperature. Unit cell parameters a, b, c, α, β and γ as a function of decreasing (black) and increasing (red) temperature are shown.

Moreover, the unit cell volume

$$V_{UC} = a \cdot b \cdot c\sqrt{1 + 2cos(\alpha)cos(\beta)cos(\gamma) - cos^2(\alpha) - cos^2(\beta) - cos^2(\gamma)} \tag{5.2}$$

is shown in Figure 5.6. The unit cell volume increases with increasing temperature with a volume thermal expansion coefficient of 309 ppm/K.

Generally, an increase of temperature cause an increase of the anharmonic vibrations of the involved atoms about their equilibrium positions. For molecules this lead to small temperature-dependent changes in the size of the molecular footprint. Consequently, while changing the temperature the molecular packing is not affected significantly, which usually leads to a small positive thermal expansion coefficient of $< 20 \cdot 10^{-6}$ 1/K [201]. In contrast, there are a few materials, for which the interatomic/intermolecular distances contract upon heating.

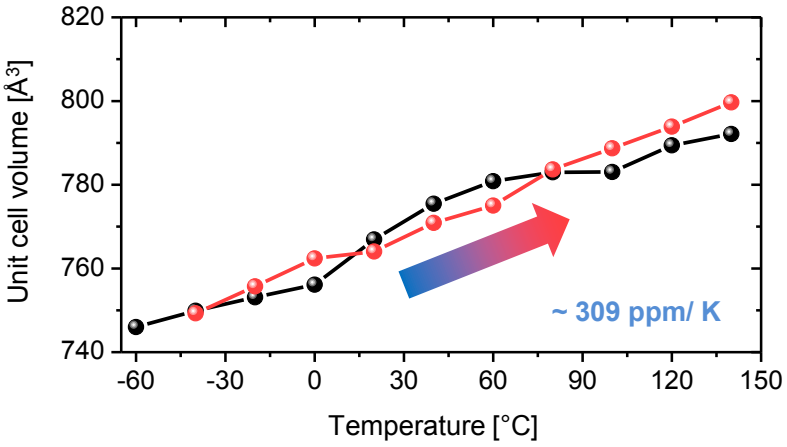

Figure 5.6: Increasing unit cell volume for PTCDI-C_8 with increasing temperature. The unit cell volume for PTCDI-C_8 increase with a volume thermal expansion coefficient of 309 ppm/ K.

This negative thermal expansion (NTE) was observed in metal oxides [82,85–87], metal-organic frameworks (MOFs) [88, 89], polymers [75] and organic crystals [91–93]. In all cases the NTE is accompanied by structural changes, in particular the change of molecular orientations within the molecular solid. More detailed information on NTE can be found in recent reviews [82–84] of this research topic. In table 5.2 the observed thermal expansion coefficient of PTCDI-C_8 is compared to other materials. PTCDI-C_8 exhibits an extraordinary large thermal expansion coefficients. For metal oxides and MOFs compound-subgroups exhibit (correlated) translational-rotational motions within the structure [87,88] resulting in NTE coefficients of up to -130 ppm/K [75]. For porous polyarylamide (PAAM) polymer films containing s-dibenzocyclooctadiene (DBCOD) a giant NTE of -1200 ppm/K was observed attributed to a submolecular conformational change for DBCOD, which alters from a 3D- to a (almost) planar conformation with temperature. Now the question arises, what is the origin of the anomalous thermal expansion for PTCDI-C_8. In this regard, a closer inspection of the 3D molecular orientations can help. The β-angle changes reversibly from 108°(-60 °C) to 102°(140 °C). The change of angle can be associated with a change of the molecular orientations of the PTCDI-C_8 molecule within the molecular ensemble. For the investigation of the impact of temperature on the molecular orientations of PTCDI-C_8 a method introduced by Krauss et al. [81, 202] is used, which will be discussed in the following sections.

Material	ΔT in K	max. α^a in ppm/K	max. α^b in ppm/K	max. α^c in ppm/K
$Ag_3Co(CN)_6$ [201]	10-400	150	150	−130
ZrW_2O_8 [85]	0.4-430	−9.1		
DBCOD polymer [75]	290-315			−1200
(S,S)-octa-3.5-diyn-2,7-diol [91]	225-330	515	−85	−204
Pentacene [93]	295-425	−35		
PTCDI-C_8 (this work)	213-413	−135	139	136

Table 5.2: Linear thermal expansion coefficient for different materials. PTCDI-C_8 exhibits an extraordinary large thermal expansion coefficients.

5.1.3 Summary: Temperature-dependent crystal structure of PTCDI-C_8 thin films

- Quantification of the crystal structure unit cell of PTCDI-C_8 thin films as a function of temperature,
- large impact of temperature on unit cell parameters: extraordinary large thermal expansion coefficient for organic thin films,
- uniaxial negative thermal expansion for PTCDI-C_8.

5.2 Temperature-dependent molecular orientations of PTCDI-C_8 on SiO_2

5.2.1 Calculation of molecular orientations

The anisotropic dimensions of the molecule result in a strongly modulated molecular structure factor and therefore in strongly modulated Bragg reflection intensities. For example, that behavior can be seen in the first Bragg rod of PTCDI-C_8 (see Figure 5.1). In the following we present a method to compare the experimentally observed Bragg reflection intensities with intensities obtained from a dedicated theoretical least-square model for the molecular structure factor. This enables us to quantify the molecular orientations regarding the surface plane. To extract the experimentally observed intensity $I^{exp}((h,k,l))$ the individual Bragg reflection has been integrated in the in-plane direction ($q_{||}$) with ± 0.05 Å^{-1} around peak position.

The resulting (h,k,l)-reflections have been fitted as a function of $q_\perp$ individually using a Gaussian function $G_{(h,k,l)}(q_\perp)$:

$$G_{(h,k,l)}(q_\perp) = \frac{I^{exp}((h,k,l))}{\sqrt{2\pi\omega_{q_\perp}^2}} \cdot exp\left(-\frac{(q_\perp - q_{\perp,(h,k,l)})^2}{2\omega_{q_\perp}^2}\right) + background \tag{5.3}$$

$q_{\perp,(h,k,l)}$	Peak position of the Bragg reflection
$\omega_{q_\perp}$	Full width at half maximum (FWHM) of the reflection

Furthermore, the experimentally observed intensity I_{exp}^{raw} has been corrected using standard correction factors for the polarization and for the transformation from angular to q-space for Grazing Incidence X-ray Diffraction [203] before comparing with theoretical intensity. The comparison of theoretical and (corrected) experimentally observed intensities has been performed for all experimentally acquired temperatures. Accounting for the impact of temperature T on the molecular vibrations and therefore on the Bragg reflection intensities the Debye-Waller factor DWF has been used for corrections [23]

$$DWF = exp\left(-\frac{k_B \cdot T \cdot q^2}{M_{PTCDI-C_8} \cdot \omega^2}\right) \tag{5.4}$$

with k_B the Boltzmann constant, q the momentum transfer, $M_{PTCDI-C_8}$ the molecular mass of PTCDI-C_8 of $1.01924 \cdot 10^{-24}$ kg and ω the average oscillations frequency of the molecule. In the considered temperature range from -60 °C to 140 °C the oscillation frequency ω is approximately 10^{13} Hz according to the equation $\omega = 2k_BT/h$ used in the

KMC simulations in section 4.3.

To quantify the molecular orientations the corresponding intensity of the molecular structure factor $I_{mol} \propto |F_{mol}|^2$ of one PTCDI-C_8 molecule has to be calculated. As we have seen in Section 3.1.1 the structure factor of a molecule can be calculated (in kinematic approximation) by summing up all individual atomic form factors f_{Atom} of the single atoms within a molecule (see equation 3.5). The resulting molecular structure factor for PTCDI-C_8 $F_{PTCDI-C_8}$ looks as follows:

$$F_{PTCDI-C_8}(h,k,l) = \sum_{j=1}^{42} f_H \cdot e^{i\boldsymbol{q}(h,k,l)\cdot \boldsymbol{r_j^H}} + \sum_{j=1}^{40} f_C \cdot e^{i\boldsymbol{q}(h,k,l)\cdot \boldsymbol{r_j^C}} + \\ + \sum_{j=1}^{4} f_O \cdot e^{i\boldsymbol{q}(h,k,l)\cdot \boldsymbol{r_j^O}} + \sum_{j=1}^{2} f_N \cdot e^{i\boldsymbol{q}(h,k,l)\cdot \boldsymbol{r_j^N}} \tag{5.5}$$

f_j	Form factor of the atom j
r_j^m	Position of the atom m within the molecule
$q(h,k,l)$	Momentum transfer $\boldsymbol{q}(h,k,l) = h \cdot \boldsymbol{a}^* + k \cdot \boldsymbol{b}^* + l \cdot \boldsymbol{c}^*$

The atomic form factors f_j have been calculated using equations 3.3 and 3.4. The exact values for f_0, f' and f'' are tabled in appendix A.2. The individual position of the PTCDI molecule backbone and the C_8 akyl chains are varied until the observed experimental intensities are properly described in order to find the optimal molecular arrangement. Six angles have been introduced, three angles for the PTCDI backbone (θ_x^{PTCDI}, θ_y^{PTCDI} and θ_z^{PTCDI}) describing the relative orientation within the crystal structure and three angles for the relative position of the alkyl chains ($\theta_x^{C_8}$, $\theta_y^{C_8}$ and $\theta_z^{C_8}$) regarding the PTCDI backbone (see Figure 5.7 for an illustration of the angles). The same procedure has been used by Krauss et al. to quantify the molecular orientation of PTCDI-C_8 on sapphire [81, 202]. A *Genetic Algorithm* is used to find the best six angles, for which the theoretical intensity of the molecular structure factor $I^{theo}_{PTCDI-C_8} \propto |F_{PTCDI-C_8}|^2$ fits the experimentally observed ones I^{exp} best. This is done by optimizing least-square values χ^2 for all employed temperatures

$$\chi^2(T) = \sum_{i}^{N(T)} (I^{theo}_{PTCDI-C_8}(\{h,k,l\}_i) - I_{exp}(\{h,k,l\}_i))^2 \tag{5.6}$$

with $N(T)$ being the number of observed Bragg reflection for a certain temperature T and $\{h,k,l\}$ being the Bragg reflection assignment.

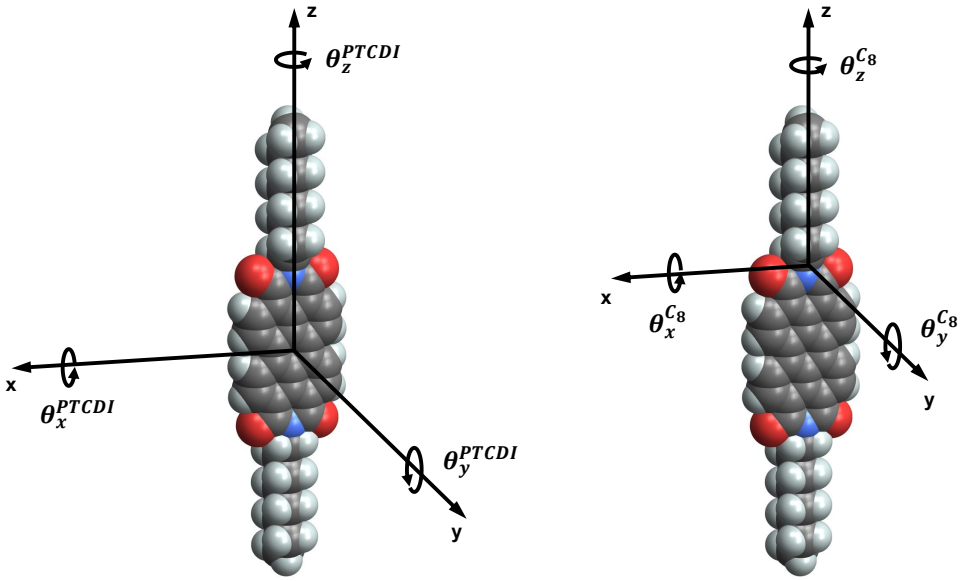

Figure 5.7: Description of PTCDI backbone and alkyl chain C_8 for calculation of molecular structure factor. Three angles for the PTCDI backbone (θ_x^{PTCDI}, θ_y^{PTCDI} and θ_z^{PTCDI}) describing the relative orientation within the crystal structure and three angles for the relative position of the alkyl chains ($\theta_x^{C_8}$, $\theta_y^{C_8}$ and $\theta_z^{C_8}$) regarding the PTCDI backbone have been defined. The a-b plane spanned by the a- and b-axis of the unit cell is located in the x-y plane.

5.2.2 Molecular orientations for $T = 140$ °C

For the initial temperature of 140 °C the angles are $\theta_x^{C_8} = -55.8$ °, $\theta_y^{C_8} = 19.8°$, $\theta_z^{C_8} = -4.6°$, $\theta_x^{PTCDI} = -13.7°$, $\theta_y^{PTCDI} = 155.5°$ and $\theta_z^{PTCDI} = -71.3°$ describing the experimental intensities best. In PTCDI-C_8 single crystals similar values for the C_8 were found ($\theta_x^{C_8} = -45°$, $\theta_y^{C_8} = 11°$, $\theta_z^{C_8} = 0°$) [16]. The excellent agreement between calculated and experimentally observed intensities are shown in Figure 5.8. The Bragg reflection (103) has been used for normalization in the illustration. Especially, the intensities for the strongest reflections (101), (013), $(1\bar{1}0)$ and $(1\bar{1}1)$ nicely agree with the calculated ones. Slight derivations for the reflections closely located to the critical scattering vector for PTCDI-C_8 $q_C^{PTCDI-C_8} = 0.032$ Å^{-1}, such as $(\bar{1}01)$, $\bar{1}\bar{1}0$, (011) and $(\bar{1}12)$ can be explained by the fact that they have to be calculated rather in dynamical than kinematic theory. Furthermore, the strong modulations in the experimental intensity(see Figure 5.8b) due to the anisotropic molecule-dimensions are nicely reproduced in the calculations as can be seen in Figure 5.9. The 2D color plot shows the calculated intensity $I_{PTCDI-C_8}^{theo}$ for the $(h0l)$ reflection as a function of the Miller indices h and l.

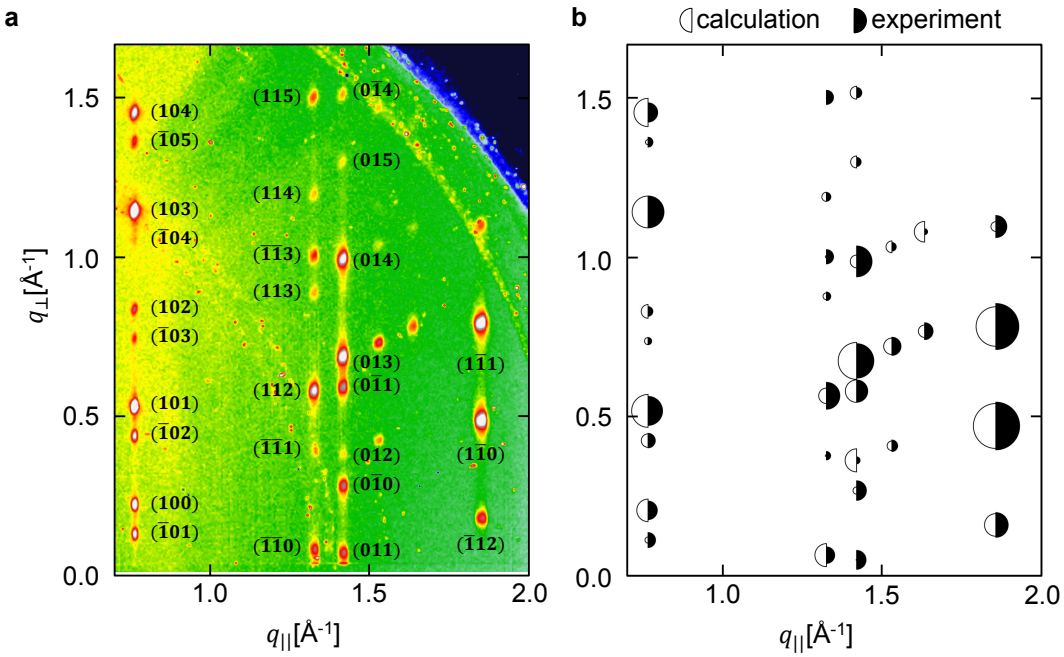

Figure 5.8: Excellent agreement between experiment and calculation for the Bragg reflection intensities. (a) GIXD measurement for $T = 140$ °C and (b) comparison of experimentally observed and calculated Bragg reflection intensities.

For clarification the calculated intensity for the first Bragg rod ($10l$) is shown in a line graph. The quantification of the aforementioned angles enables the determination of the molecular arrangement of the single molecules within the unit cell. In Figure 5.10 this arrangement is depicted. In Figure 5.10a and Figure 5.10b the a-c (shown from the direction of b vector) and the b-c plane (shown from the a vector) are given. PTCDI-C_8 on SiO_2 features a slipped π-π stacking in the [010]-direction. The slipped π-π stacking was also observed for the PTCDI-C_8 single crystals [16] and other perylene derivatives [28]. The smallest intermolecular distance of molecule planes is 3.45 Å and agrees with typical stacking distances for perylene crystal structures [204]. In Figure 5.10c the resulting unit cell in three dimensions can be seen. Importantly, the directional stacking lead to the predominant overlap of π-orbitals in the b-direction. Furthermore, the molecular tilt φ, which is the angle between the molecular backbone (PTCDI) and the a-b plane (see Figure 5.10d), can be quantified. For $T = 140$ °C a molecular tilt of 77.5° has been found. For the PTCDI-C_8 single crystals a molecular tilt of 69° was determined.

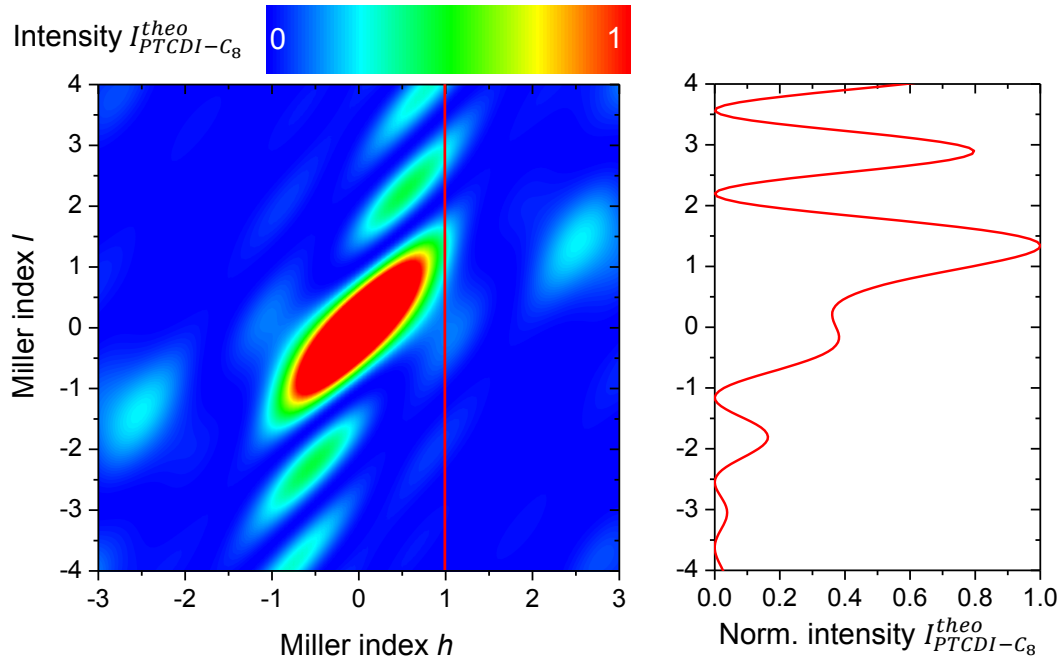

Figure 5.9: Oscillating behavior for the Bragg rod $(10l)$**.** (a) The calculated intensity $I^{theo}_{mol} \propto |F_{mol}|^2$ for the $(h0l)$ reflection as a function of the Miller indices h and l and (b) line graph for the Bragg rod $(10l)$. In agreement to the experimental data an oscillating behavior for the calculated intensity has been observed.

The more dominate role of the surface energy within thin film compared to single crystal can lead to different favored equilibrium structure in thin films compared to crystals and could be accounted for the difference in molecular tilt of 8°. For PTCDI-C_8 on sapphire a molecular tilt of 67° and slight different 3D molecular arrangement were observed [81]. This differences could be traced back to the stronger effective interaction of the substrate with molecules as it was also observed for DIP on SiO_2 and sapphire [56]. Such surface induced phases (SIP) of organic materials are of interest in current research and were observed for different organic materials such as caffeine on mica and silica [205] or paracetamol [206].

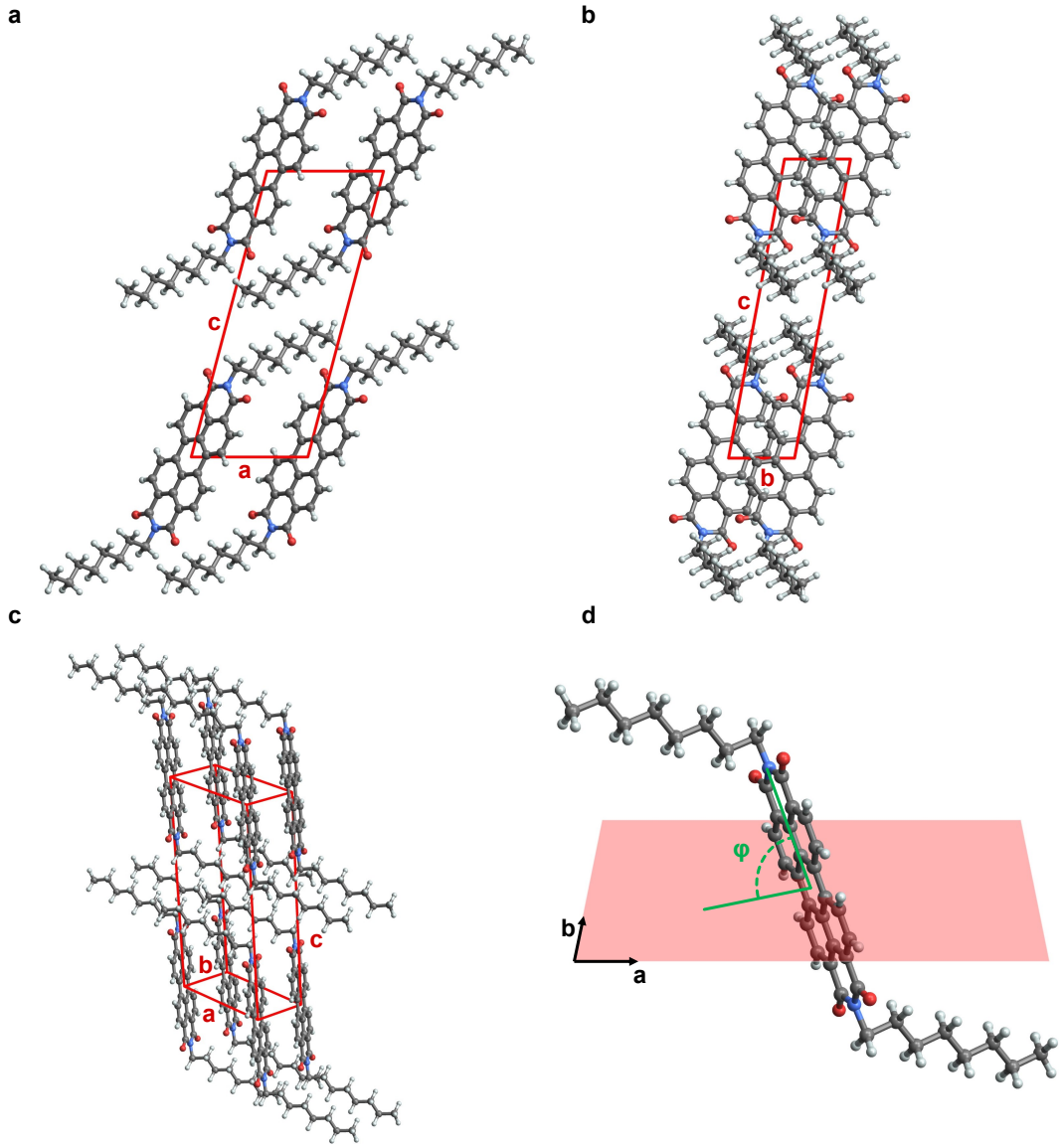

Figure 5.10: Molecular arrangement for PTCDI-C_8 on SiO_2. (a) a-c plane, (b) b-c plane and (c) 3D molecular arrangement within the unit cell for $T = 140$ °C. A intermolecular distance of 3.45 Å has been found. (d) From the arrangement of the molecule within the unit cell the molecular tilt φ has been quantified to 77.5°.

5.2.3 Control of molecular orientations with temperature

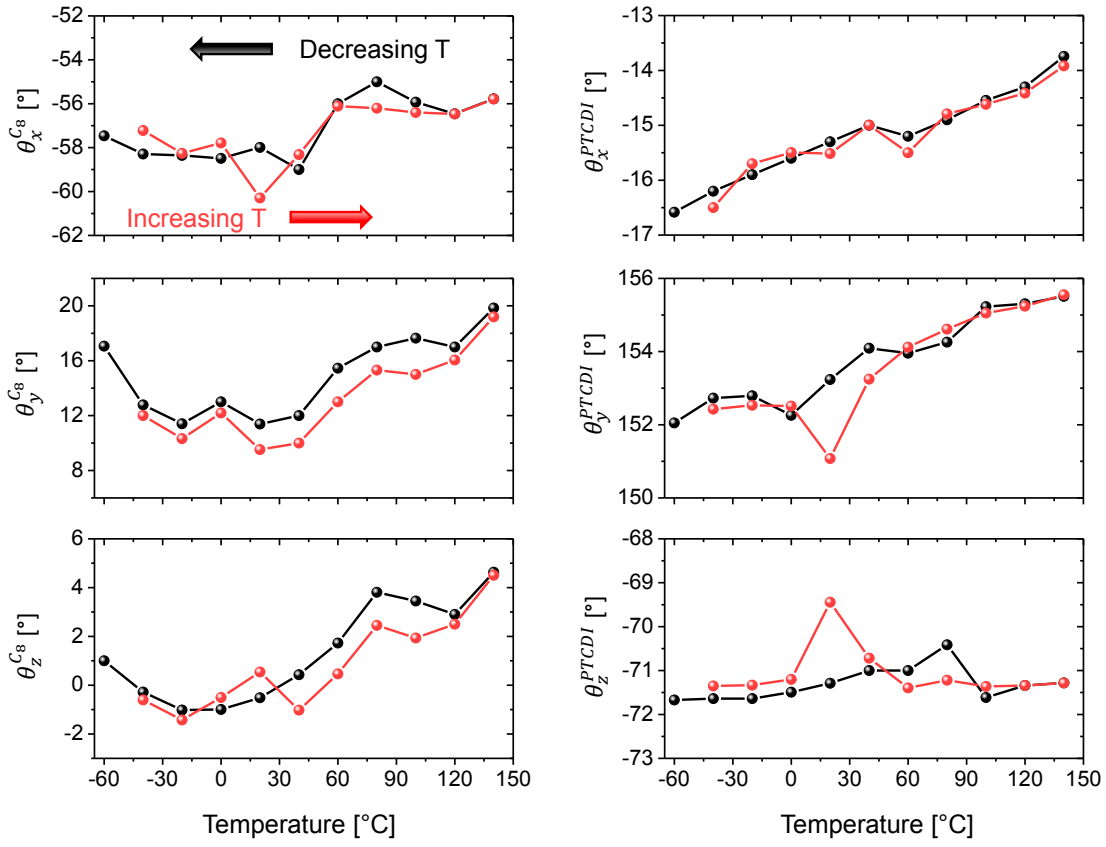

Figure 5.11: Optimized angles $\theta_x^{C_8}$, $\theta_y^{C_8}$, $\theta_z^{C_8}$, θ_x^{PTCDI}, θ_y^{PTCDI} and θ_z^{PTCDI} describing the molecular arrangement for all employed temperatures. A significant change as a function of temperature has been observed for the angles θ_x^{PTCDI} and θ_y^{PTCDI}.

The analysis presented in detail for the initial temperature of 140 °C has been repeated for all temperatures studied in the experiment. In Figure 5.11 the angles $\theta_x^{C_8}$, $\theta_y^{C_8}$, $\theta_z^{C_8}$, θ_x^{PTCDI}, θ_y^{PTCDI} and θ_z^{PTCDI} are shown as a function of temperature. Importantly, the temperature controls the angles. There is also a slight temperature influence on the angles characterizing the relative position of the alkly chains with respect to the molecular core. However, the most interesting feature is the large impact of temperature on the angles θ_x^{PTCDI} and θ_y^{PTCDI}, which define the relative position of the molecular core regarding the a-b plane. Both angles increase by three and four degrees, respectively, in the temperature range from −60 °C to 140 °C. The corresponding comparison between calculated and experimentally observed Bragg intensities for these angles is shown in the appendix A.3 for 140 °C (1^{st}), 40 °C (1^{st}), −60 °C, 40 °C (2^{nd}) and 40 °C (1^{st}) . An excellent

agreement for all employed temperatures has been observed. Figure 5.12 illustrates the different arrangements of the molecule for the temperatures of 140 °C (dark molecule) and of −60 °C (light molecule). The change of the angle pivoting on the small molecular axis (θ_x^{PTCDI}) by three degree can clearly be seen. Furthermore, one can distinguish the four-degree rotation about the axis perpendicular to the molecular plane (described by θ_y^{PTCDI}) increasing the temperature from −60 °C to 140 °C. The change of the aforementioned angles is accompanied by a change of the molecular tilt φ (see Figure 5.10d for an illustration of the angle).

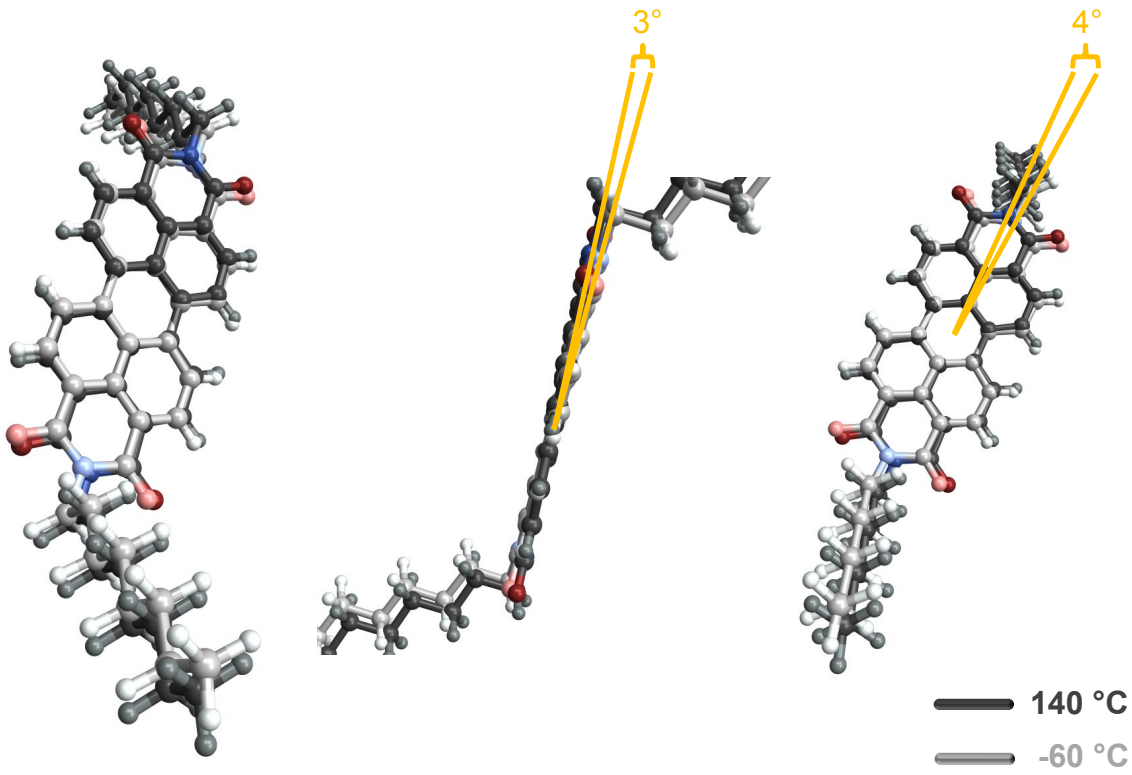

Figure 5.12: Temperature-dependent molecular arrangement for PTCDI-C_8 on SiO_2. The molecular arrangement of PTCDI-C_8 is illustrated in three different views for the temperatures of −60 °C (light molecule) and 140 °C (dark molecule).

In Figure 5.13 the extracted molecular tilt for a temperature range from −60 °C to 140 °C is shown. The graph in black illustrates the observed orientation when decreasing the temperature, whereas the red graph shows the orientation during the increase of temperature. The molecular tilt φ increases continuously from 75.4° for −60 °C to 77.5° for 140 °C exhibiting a rising rate of 0.01°/K. Importantly, the tilt of the molecule can be controlled with temperature in a reversible way as the measurements clearly demonstrate.

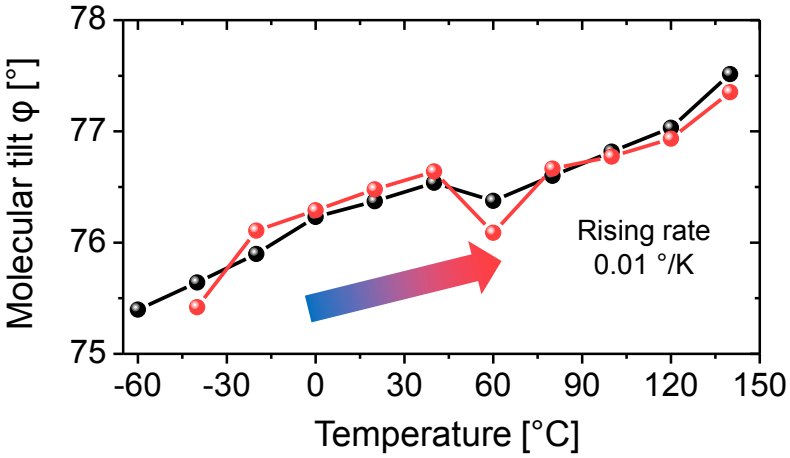

Figure 5.13: Control of molecular tilt with temperature. The molecular tilt for PTCDI-C_8 on SiO_2 for decreasing (black) and increasing (red) temperature is shown. The molecular tilt as a function of temperature exhibits a rising rate of 0.01°/K.

5.2.4 Summary: Temperature-dependent molecular orientations

- Determination of the molecular packing of PTCDI-C_8,
- reversible and continuous control of the molecular orientations PTCDI-C_8 as a function of temperature,
- temperature-controlled molecular tilt φ (angle between a-b plane and the long molecular axis) from 75.5° to 77.5° for increasing temperature from −60 °C to 140 °C.

5.3 Discussion on the change of molecular orientations with temperature

The experimental results in combination with the computational efforts demonstrate that the unit cell parameters, the rotational degrees of freedom and the tilt angle of the molecule related to the surface plane, can continuously and reversibly be controlled with temperature. The experimental observations go beyond the normal thermal expansion as the negative thermal expansion of the *a*-axis and the change of molecular orientations show. For organic materials it is challenging to identify the driving force for NTE's to appear. The molecular packing in organic crystals is attributed to complex intermolecular interactions from van-der-Waals and electrostatic forces such as hydrogen-bonding [91], which easily expand upon heating.

The NTE in organic crystalline materials can be related to a change of the molecular orientations. In pentacene crystals negative thermal expansion of a-axis was found due to libration along the long molecular axis, which was accompanied with a change in herringbone angle within the molecular packing [93]. For a dumbbell-shaped organic molecules ((S,S)-octa-3,5-diyn-2,7-diol) the molecular tilt (angle between long molecular axis and a crystal plane) decreases from 54.2° for 225 K to 51.0° for 330 K, which causes the *a*-axis to expand and the *b*- and *c*-axis to become shorter with increasing temperature [91].

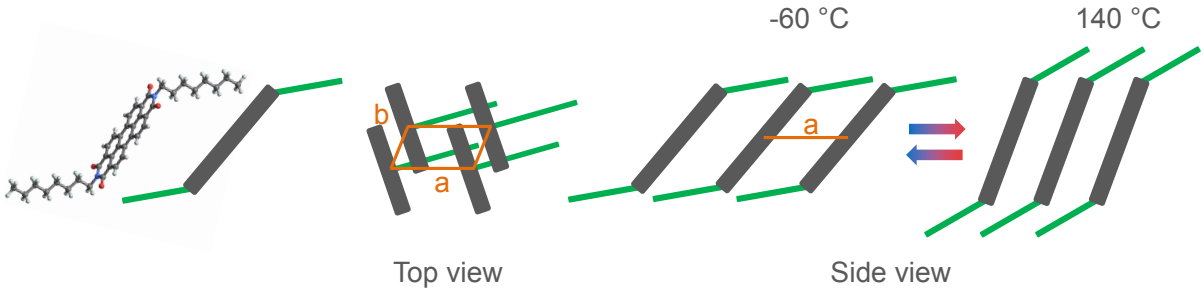

Figure 5.14: Impact of temperature on the molecular structure. The change of orientations mostly influences the a-axis as the molecule is arranged almost perpendicular to the a-direction. The more upright standing molecules for larger temperatures lead to a smaller a- and a larger c-axis. The change of molecular orientations is increased by a factor of 10.

The negative thermal expansion for PTCDI-C_8 on SiO_2 can be understood by the thermally-induced change of molecular orientations of PTCDI-C_8 within the supra-molecular assembly. Especially, the shrinking of the *a*-axis with increasing temperature arises from the increasing value for θ_x^{PTCDI} as shown in Figure 5.14. The in-plane unit cell (top view) shows that the change of orientations mostly influences the a-axis as the molecule

is arranged almost perpendicular to the a-axis. Consequently, the more upright standing molecules for larger temperatures lead to a smaller a-axis and a larger c-axis. Thereby the alkyl chain plays a key role for the molecular rearrangement. The alkyl chains act as spacers within the molecular ensemble providing space for the molecule to arrange in response of temperature changes.

Furthermore, the interaction of the PTCDI-C_8 molecules could not only be attributed to van-der-Waals forces but also to stronger hydrogen-bonded forces [95]. Hydrogen forces between a hydrogen atom of alkyl chains and the oxygen atom [95] of neighboring PTCDI backbones can potentially result in a more stable molecular packing, but also enhance the flexibility as it was observed for the dumbbell-shape molecule [91]. Therefore, a flexible molecular network is built up allowing hinge-like motions to occur between the PTCDI-core and the alkyl chain. This can enable concerted motions of all the molecules as enough space is left for a cooperative thermomechanical response of the molecules to the variation of temperature. This molecular rearrangement is connected with an optimization of the intermolecular interactions in the molecular ensemble for a certain temperature including van-der-Waals and electrostatic interactions. These origin from the quadropole moment of the molecule as well as the hydrogen-bonding forces.

5.3.1 Thermodynamic impact on structure and molecular packing

The fascinating but also anomalous behavior of the temperature-dependent structural properties prompt the question of the thermodynamical origin. The structure of a (surface) crystal is the result of the minimization of the energy of the material system. Note, that for surface structures also the surface and interfacial energies have to be considered.

Two major characteristics appear when changing the temperature. Firstly, for temperatures approaching zero ($T \to 0$) the impact of the internal on the entire energy of the system strongly increases. For organic thin film structures this measure is identified with the *van-der-Waals* energy and the energy corresponding to electrostatic forces. Consequently, given the increasing impact of molecular interactions within the surface crystal structure with decreasing temperature the molecule tends to lay down more. A related behavior has been found during the growth of organic semiconductors such as diindenoperylene (DIP) on SiO_2 [99, 162] and DIP on gold [207]. A transition towards a more tilted structural phase was observed with increasing thickness, which is associated with the rising impact of molecular interactions within the developing bulk structure. For very thin films the surface energy of the adsorbate on the substrate plays the decisive role for structure formation [208]. Secondly, when increasing the temperature the entropy of the system plays a more distinct role within the entire energy. A rise of entropy influence could cause a energy minimum at higher temperatures directly associated with the formation of

a different thin film structure. Note, that the internal energy also changes with temperature, as the unit cell parameter differs for each temperature. The competing interplay of the impact of the internal energy and entropy in our temperature-dependent experiments could explain the observation of the reversible and continuous change of structural properties of PTCDI-C_8 thin films. At low temperatures the thin film structure of PTCDI-C_8 (almost) exclusively arise from the molecular interactions, which is in contrast to higher temperatures, for which the entropy have to be considered.

5.4 Summary: Negative thermal expansion and temperature-controlled rotational motions of PTCDI-C_8

- **Large positive and negative thermal expansion in PTCDI-C_8 thin films**
  - Highly crystalline molecular thin film,
  - reversible and continuous change of all unit cell axes with an exceptionally large thermal expansion coefficient of up to 140 ppm/ K,
  - negative thermal expansion of the a-axis of the crystalline structure of PTCDI-C_8.
- **Temperature-controlled rotational motions of PTCDI-C_8**
  - Reversible and continuous cooperative rotational motions upon heating or cooling of PTCDI-C_8 including a temperature-controlled molecular tilt lead to large positive and negative thermal expansion,
  - the molecules within the molecular ensemble perform cooperative thermomechanical motions as enough space is left for molecular rearrangement due to the variation of temperature,
  - from the perspective of thermodynamics, the interplay between the increasing influence of molecular interactions for low temperatures, on the one hand, and the rising impact of entropy with increasing temperature, on the other hand, influence the structure evolution and can give rise to the reversibility of the structural properties.

6 Summary: Molecular processes in organic thin films

This thesis uses *in situ* and real-time experiments with atomic resolution to gain fundamental understanding of surface processes during molecular self-assembly and thermally-activated processes such as post-growth dewetting and cooperative rotational motions associated with large positive and negative thermal expansion.

Unravelling the multilayer growth of the prototypical molecular semiconductor C_{60}

For the rational design of complex nanomaterials from molecular building blocks the understanding of molecular self-assembly on the nanoscale is essential. For molecular growth, there exist theoretical studies based on scaling laws to describe large scale and crystal growth. A few studies exist, which shed light on the atomic and molecular scale of diffusion, nucleation and the Ehrlich-Schwoebel barrier for interlayer transport across a molecular step-edge. However, there is no single organic compound for which a set of the three major parameters during molecular self-assembly, the diffusion barrier, lateral binding energy and Ehrlich-Schwoebel barrier have been simultaneously and consistently quantified in a single experiment to describe multilayer molecular growth.

- *Result 1: First quantification of a consistent set of energy barriers describing multilayer growth of C_{60} .*

In this thesis an innovative scattering technique combining real-time and *in situ* anti-Bragg oscillations and diffuse x-ray scattering was used to study the lateral and vertical length scales during C_{60} nucleation and multilayer growth for different temperatures and deposition rates. Distinctly different growth oscillations in the specular and diffuse x-ray scattering during growth were found for all employed growth conditions indicating layer-by-layer growth for C_{60} on mica. From the oscillating behavior of the island density three regimes within the growth of one monolayer were deduced: the nucleation, lateral growth and coalescence regime. The temperature-, rate- and time-dependent island density and layer coverage data have been compared with kinetic Monte Carlo simulations and a self-consistent set of energy parameters, which describe both intra- and interlayer diffusion

processes in C_{60} growth, was quantified for the first time. This approach yields an effective Ehrlich-Schwoebel barrier of $E_{ES} = 110$ meV, diffusion barrier of $E_D = 540$ meV and a lateral binding energy of $E_B = 130$ meV. Through this work predictive simulations of C_{60} nanostructures can be performed, which opens the possibility of rational design of C_{60} nanomaterials.

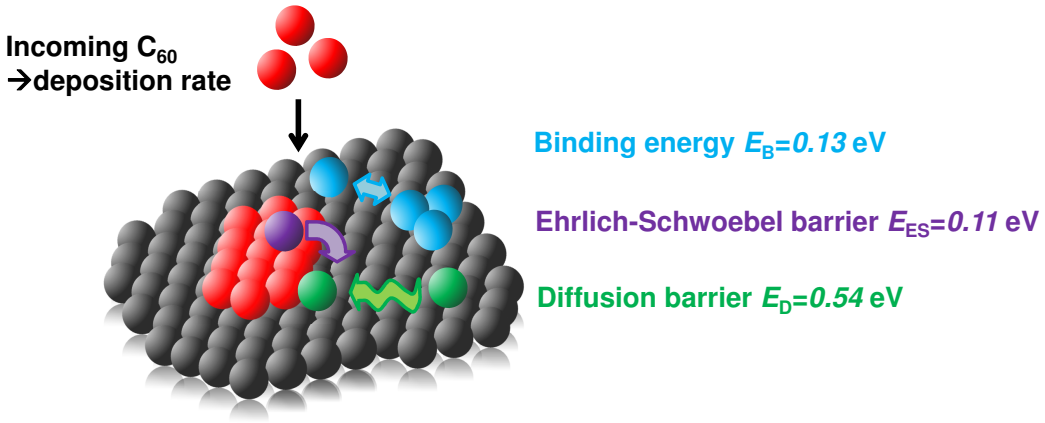

Figure 6.1: Surface processes during the growth of the fullerene C_{60}. The lateral binding characterized by the lateral binding energy E_B, the interlayer diffusion across a step-edge (Ehrlich-Schwoebel barrier E_{ES}) and the diffusion barrier (E_D) quantify the major processes on the surface during growth.

- *Result 2: The intermediate range of interactions of C_{60} , in between those of atoms and colloids, leads to an E_{ES} of energetic origin as in atoms, while the lateral diffusion is similar to colloids.*

Interestingly, the fullerene C_{60} exhibits properties in between those of atoms and colloids. On the one hand, the van-der-Waals diameter of C_{60} of 1 nm is closer to the atomic than to the colloidal length scale. On the other hand the attractive interactions with respect to particle radius is of short ranged nature, which resembles colloids rather than atoms. Such intermediate properties of the fullerene C_{60} between atoms and colloids influence the growth dynamics on a single-particle level. The short-range nature of the attractive interactions leads to larger free diffusion times of C_{60} compared to atoms, thereby resembling colloidal diffusion (see Figure 6.2 for an illustration of the corresponding energy landscape). This is due to the fact that atoms can form new bonds more quickly because of the longer range of atomic interactions (with respect to their size) and the stronger binding energy. However, C_{60} exhibits a real energetic step-edge barrier like atoms, which is qualitatively different from colloidal systems. For C_{60}, and especially for

atoms, descending a step-edge is connected with a transition state of lower coordination, which is directly connected to weaker bonding and thus a higher energy. For colloids one observes a purely diffusive Ehrlich-Schwoebel barrier, arising from a lower diffusion probability along the geometrically longer path across the step edge.

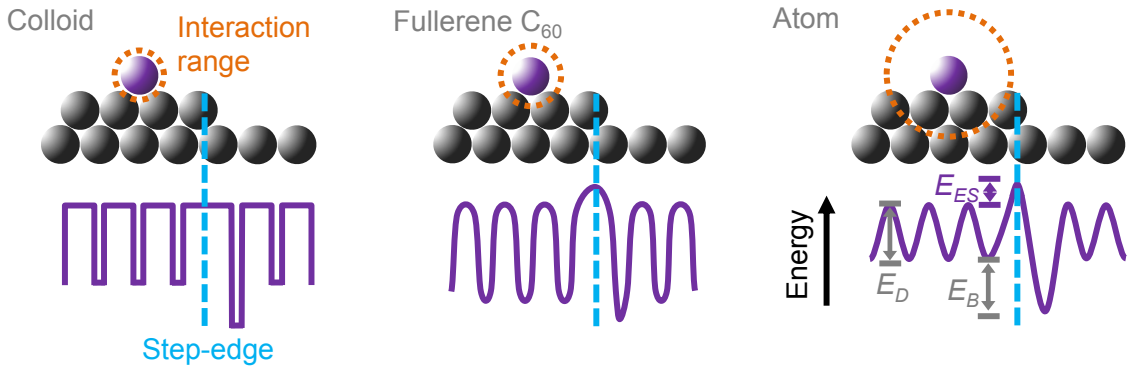

Figure 6.2: Schematic illustration of energy landscape for atoms, colloids and the fullerene C. The interaction range of the different materials clearly affects the shape of the energy landscape and, therefore, influences the surface diffusion, the lateral binding and the character of step-edge barrier.

The quantified energy barriers for C_{60} are not only important for the surface processes during the growth, but also after the growth is stopped. As growth is a non-equilibrium process, which means that the structure during growth does not necessarily have to be the most stable one, post-growth reorganization can occur. The kinetic paths of the molecules during the reorganization process are influenced by these energy barriers.

- *Result 3: Thermally-activated post-growth dewetting for C_{60}.*

To unravel the post-growth dewetting for C_{60} x-ray growth oscillations were monitored during the growth of the first monolayer and after stopping the growth once the first monolayer was finished for different temperatures. A thermally-activated post-growth dewetting behavior for the first monolayer was found. An increase of the substrate temperature of 40 K leads to a five-times faster upward mass transport during dewetting. From these temperature-dependent measurements an effective activation barrier for upward interlayer transport of (0.33 ± 0.14) eV has been found.

- *Methodical advances: following the lateral and vertical thin film growth in real-time.*

Besides answering the pure scientific questions of growth, the methods necessary to observe the molecular self-assembly were advanced. The high brilliance and low emittance of third generation synchrotron radiation sources such as PETRA III in Hamburg enable us to measure x-ray growth oscillations and diffuse x-ray scattering (GISAXS) simultaneously during the growth (see Figure 6.3 for the x-ray scattering geometry).

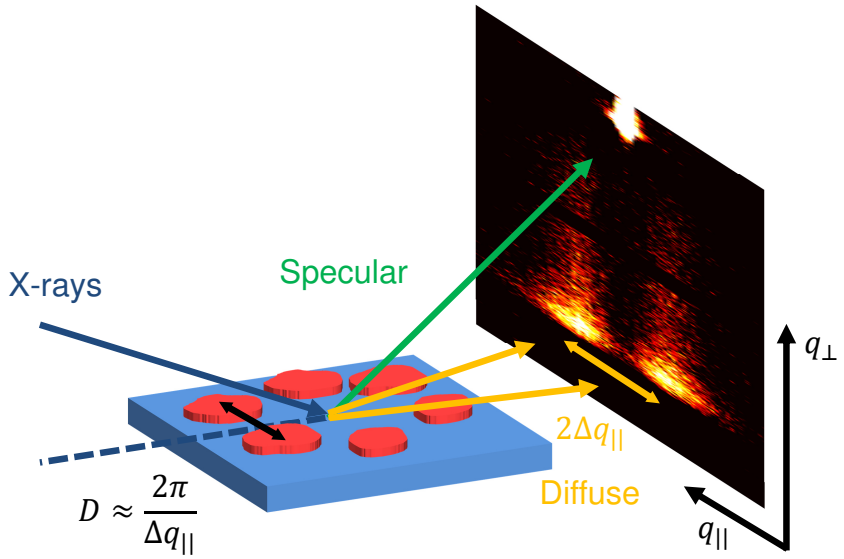

Figure 6.3: Simultaneous measurement of x-ray growth oscillations and diffuse x-ray scattering (GISAXS) during the growth. The high brilliance and low emittance of third generation synchrotron radiation sources such as PETRA III in Hamburg enable us to measure x-ray growth oscillations and diffuse x-ray scattering (GISAXS) simultaneously during the growth. Therefore, the lateral and vertical thin film growth can be followed in real-time.

This gives us vertical and lateral film information following the multilayer growth on the nanoscale with a few second time resolution. Previously no complete diffuse x-ray scattering (GISAXS) pattern, but only the diffuse scattering near the anti-Bragg point was used by Fleet et al. [209] for getting information on the lateral length scale during growth of $SrTiO_3$ on $SrTiO_3$(001). The lateral film information enables us to distinguish between the nucleation, lateral growth and coalescence regime on a short timescale.

Negative thermal expansion connected with cooperative rotational motions of PTCDI-C_8

The molecular scale understanding of the movement of single ad-molecules during growth and a rational choice of growth conditions ultimately leads to an optimized design of functional nanomaterials. Going one step further to a mechanical functionality of supra-molecular assemblies the subsequent challenge is to address and control the internal and rotational degrees of freedom of the molecular building blocks with external stimuli. Such responsive materials show the ability to respond to external stimuli like heat or irradiation of light by mechanoresponsive processes on the molecular and/or supra-molecular level. Cooperative mechanical motions on the nanoscale can be found for materials with large positive and, especially, negative thermal expansion (NTE) [82–84]. These molecular materials, for which the interatomic/ intermolecular distances contract upon heating, can be primarily found for inorganic but rarely for organic materials.

- *Result 4: Large positive and negative thermal expansion in organic thin films of PTCDI-C_8.*

To explore the influence of temperature on the surface crystal structure of the organic semiconductor PTCDI-C_8 Grazing Incidence X-ray Diffraction (GIXD) as a function of temperature from -60 °C to 140 °C were performed. High structural order was found in the thin film with up to 35 Bragg reflections. From the evaluation of the Bragg reflection positions the unit cell parameters were derived and a large impact of temperature on the unit cell parameters has been found. All unit cell axes reversibly change with an exceptionally large thermal expansion coefficient. The b- and c-axis exhibit a positive thermal expansion coefficient of 139 ppm/K and 136 ppm/K. Surprisingly, the a-axis of the crystalline structure of PTCDI-C_8 reversibly contracts with increasing temperature. The negative thermal expansion coefficient for the a-axis is -135 ppm/K. The appearance of NTE goes beyond the normal thermal expansion. Organic crystals are held together by weak van-der-Waals, electrostatic and/ or hydrogen-bonding forces, which easily expand upon heating. For molecules with asymmetric dimensions the additional vibrational and rotational degrees of freedom have to be considered for describing the cooperative molecular processes during annealing.

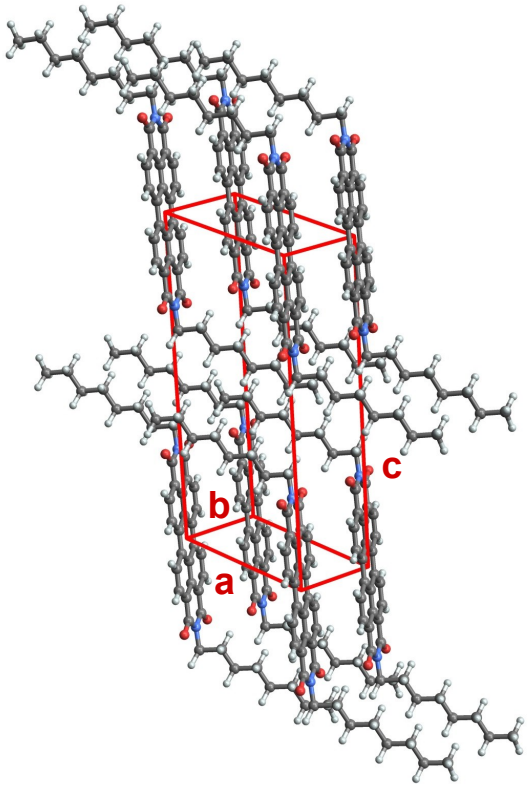

Figure 6.4: Unit cell and molecular packing of the organic semiconductor PTCDI-C_8 . Unit cell and molecular packing of PTCDI-C_8 for a temperature of 140 °C. PTCDI-C_8 on SiO_2 features a slipped π-π stacking in the [010]-direction.

- *Result 5: Cooperative molecular rotational motions during annealing.*

For information on these molecular orientations the molecular structure factor was modeled following the approach introduced by Krauss et al. [81]. From the comparison of the experimentally observed Bragg reflection intensities and the calculated molecular structure factor the mechanism of the large positive and negative thermal expansion has been unraveled. It was found, that the negative thermal expansion of the PTCDI-C_8 thin film structure can be understood by thermally-induced cooperative rotational motions of the molecule upon heating or cooling. The explanation for the appearance of this anomalous behavior is rather challenging because the intermolecular interactions are complex. Firstly, the usual van-der-Waals interactions between the molecules contribute.

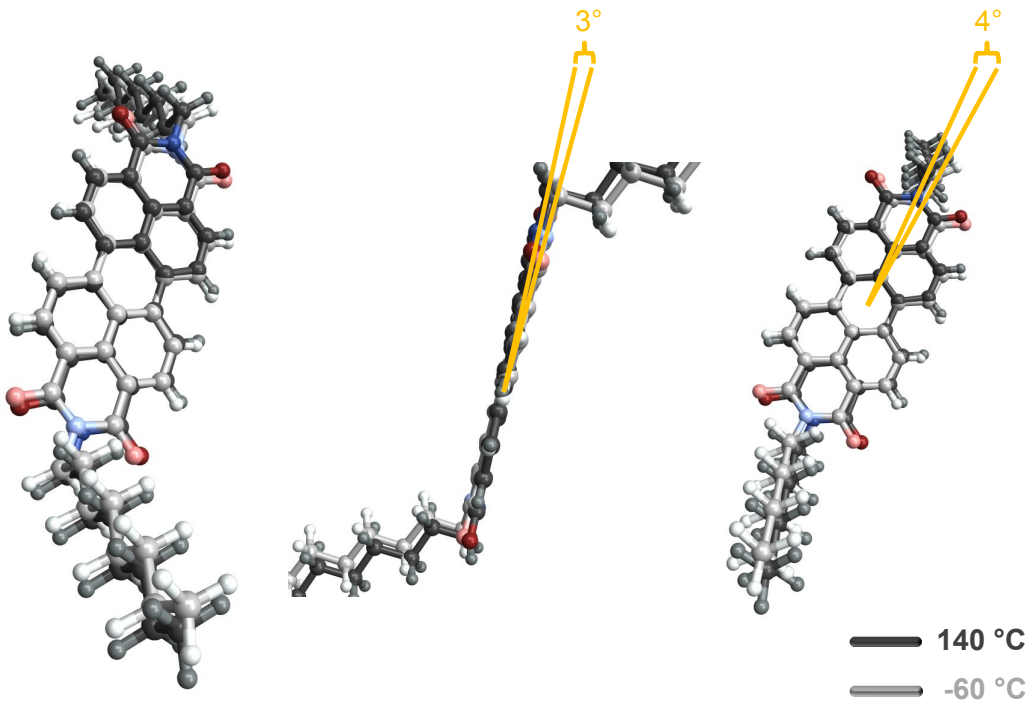

Figure 6.5: Temperature-dependent molecular orientations for PTCDI-C_8 on SiO_2. Molecular arrangement of PTCDI-C_8 for the temperatures of −60 °C (light molecule) and 140 °C (dark molecule).

Secondly, electrostatic forces stemming from the quadrupole moment of the PTCDI-C_8 molecule and possible hydrogen-bonding forces between a hydrogen atom of an alkyl chain and an oxygen atom of a neighboring PTCDI backbone influence the interactions. The molecules within the molecular ensemble perform cooperative motions as enough space is left for molecular rearrangement and to optimize the intermolecular interactions due to the variation of temperature. Additionally, the temperature itself plays an important role. The interplay between the increasing influence of molecular interactions for low temperatures, on the one hand, and the rising impact of entropy with increasing temperature, on the other hand, influence the structure evolution and can give rise to the reversibility of the structural properties.

In summary, analyzing molecular processes, such as the movement of single ad-molecules on the surface as a function of growth conditions for the prototypical molecular semiconductor C_{60} and cooperative mechanical motions of molecules within supra-molecular and crystalline ensembles of PTCDI-C_8, yields a broader fundamental understanding of molecular scale dynamics. This molecular scale understanding helps to make one step further to the rational design of molecular functional nanomaterials.

List of Figures

Bibliography

[1] Brütting, Wolfgang (Hrsg.) ; Adachi, Chihaya (Hrsg.): *Physics of Organic Semiconductors*. 2nd. Weinheim : Wiley-VCH, 2012

[2] Yersin, Hartmut: *Highly Efficient OLEDs with Phosphorescent Materials*. Weinheim : Wiley-VCH Verlag, 2007

[3] Müllen, Klaus ; Scherf, Ullrich: *Organic Light Emitting Devices: Synthesis, Properties and Applications*. Weinheim : Wiley-VCH Verlag, 2005

[4] Forrest, SR: The path to ubiquitous and low-cost organic electronic appliances on plastic. In: *Nature* 428 (2004), S. 911–918

[5] Schreiber, F.: Organic molecular beam deposition: Growth studies beyond the first monolayer. In: *Physica Status Solidi (a)* 201 (2004), Mai, Nr. 6, S. 1037–1054. – ISSN 0031–8965

[6] Witte, Gregor ; Wöll, Christof: Growth of aromatic molecules on solid substrates for applications in organic electronics. In: *Journal of Materials Research* 19 (2004), März, Nr. 07, S. 1889–1916. – ISSN 0884–2914

[7] Forrest, SR: Ultrathin organic films grown by organic molecular beam deposition and related techniques. In: *Chemical Reviews* 97 (1997), S. 1793–1896

[8] Krebs, Frederik C.: Fabrication and processing of polymer solar cells: A review of printing and coating techniques. In: *Solar Energy Materials and Solar Cells* 93 (2009), April, Nr. 4, S. 394–412. – ISSN 09270248

[9] Opitz, A ; Wagner, J ; Brütting, W ; Salzmann, I ; Koch, N ; Manara, J ; Pflaum, J ; Hinderhofer, A ; Schreiber, F: Charge Separation at Molecular Donor-Acceptor Interfaces: Correlation Between Morphology and Solar Cell Performance. In: *IEEE Journal of Selected Topics in Quantum Electronics* 16 (2010), Nr. 6, S. 1707–1717. – ISSN 1077260X

[10] Verreet, Bregt ; Heremans, Paul ; Stesmans, Andre ; Rand, Barry P.: Microcrystalline organic thin-film solar cells. In: *Advanced materials (Deerfield Beach, Fla.)* 25 (2013), Oktober, Nr. 38, S. 5504–7. – ISSN 1521–4095

[11] Gruber, M. ; Rawolle, M. ; Wagner, J. ; Magerl, D. ; Hörmann, U. ; Perlich, J. ; Roth, S. V. ; Opitz, A. ; Schreiber, F. ; Müller-Buschbaum, P. ; Brütting, W.: Correlating Structure and Morphology to Device Performance of Molecular Organic Donor-Acceptor Photovoltaic Cells Based on Diindenoperylene (DIP) and C 60. In: *Advanced Energy Materials* 3 (2013), August, Nr. 8, S. 1075–1083. – ISSN 16146832

[12] Dimitrakopoulos, CD ; Malenfant, PRL: Organic thin film transistors for large area electronics. In: *Advanced Materials* 14 (2002), Nr. 2, S. 99–117

[13] Sirringhaus, H.: Device Physics of Solution-Processed Organic Field-Effect Transistors. In: *Advanced Materials* 17 (2005), Oktober, Nr. 20, S. 2411–2425. – ISSN 0935–9648

[14] Sirringhaus, Henning: 25Th Anniversary Article: Organic Field-Effect Transistors: the Path Beyond Amorphous Silicon. In: *Advanced Materials* 26 (2014), März, Nr. 9, S. 1319–35. – ISSN 1521–4095

[15] Braga, Daniele ; Horowitz, Gilles: High-Performance Organic Field-Effect Transistors. In: *Advanced Materials* 21 (2009), April, Nr. 14-15, S. 1473–1486. – ISSN 09359648

[16] Briseno, AL ; Mannsfeld, SCB ; Reese, Colin ; Hancock, JM ; Xiong, Yujie ; Jenekhe, SA ; Bao, Zhenan ; Xia, Younan: Perylenediimide nanowires and their use in fabricating field-effect transistors and complementary inverters. In: *Nano Letters* 7 (2007), Nr. 9, S. 2847–2853

[17] Opitz, Andreas ; Horlet, Matthias ; Kiwull, Marc ; Wagner, Julia ; Kraus, Michael ; Brütting, Wolfgang: Bipolar charge transport in organic field-effect transistors: Enabling high mobilities and transport of photo-generated charge carriers by a molecular passivation layer. In: *Organic Electronics* 13 (2012), Nr. 9, S. 1614–1622

[18] Uoyama, Hiroki ; Goushi, Kenichi ; Shizu, Katsuyuki ; Nomura, Hiroko ; Adachi, Chihaya: Highly efficient organic light-emitting diodes from delayed fluorescence. In: *Nature* 492 (2012), Dezember, Nr. 7428, S. 234–8. – ISSN 1476–4687

[19] Liao, L. S. ; Klubek, K. P. ; Tang, C. W.: High-efficiency tandem organic light-emitting diodes. In: *Applied Physics Letters* 84 (2004), Nr. 2, S. 167. – ISSN 00036951

[20] Han, Tae-Hee ; Lee, Youngbin ; Choi, Mi-Ri ; Woo, Seong-Hoon ; Bae, Sang-Hoon ; Hong, Byung H. ; Ahn, Jong-Hyun ; Lee, Tae-Woo: Extremely efficient flexible organic light-emitting diodes with modified graphene anode. In: *Nature Photonics* 6 (2012), Januar, Nr. 2, S. 105–110. – ISSN 1749–4885

[21] Reineke, Sebastian ; Lindner, Frank ; Schwartz, Gregor ; Seidler, Nico ; Walzer, Karsten ; Lüssem, Björn ; Leo, Karl: White organic light-emitting diodes with fluorescent tube efficiency. In: *Nature* 459 (2009), Mai, Nr. 7244, S. 234–8. – ISSN 1476–4687

[22] Wagner, Julia ; Gruber, Mark ; Hinderhofer, Alexander ; Wilke, Andreas ; Bröker, Benjamin ; Frisch, Johannes ; Amsalem, Patrick ; Vollmer, Antje ; Opitz, Andreas ; Koch, Norbert ; Schreiber, Frank ; Brütting, Wolfgang: High Fill Factor and Open Circuit Voltage in Organic Photovoltaic Cells with Diindenoperylene as Donor Material. In: *Advanced Functional Materials* 20 (2010), Dezember, Nr. 24, S. 4295–4303. – ISSN 1616301X

[23] Rivnay, Jonathan ; Mannsfeld, SCB ; Miller, CE ; Salleo, Alberto ; Toney, MF: Quantitative determination of organic semiconductor microstructure from the molecular to device scale. In: *Chemical Reviews* 112 (2012), S. 5488–5519

[24] Hörmann, Ulrich ; Lorch, Christopher ; Hinderhofer, Alexander ; Gerlach, Alexander ; Gruber, Mark ; Kraus, Julia ; Sykora, Benedikt ; Grob, Stefan ; Linderl, Theresa ; Wilke, Andreas ; Opitz, Andreas ; Hansson, Rickard ; Anselmo, Ana S. ; Ozawa, Yusuke ; Nakayama, Yasuo ; Ishii, Hisao ; Koch, Norbert ; Moons, Ellen ; Schreiber, Frank ; Brütting, Wolfgang: Voc from a Morphology Point of View: the Influence of Molecular Orientation on the Open Circuit Voltage of Organic Planar Heterojunction Solar Cells. In: *The Journal of Physical Chemistry C* 118 (2014), S. 26462–26470

[25] Hansson, Rickard ; Ericsson, Leif K. E. ; Holmes, Natalie P. ; Rysz, Jakub ; Opitz, Andreas ; Campoy-Quiles, Mariano ; Wang, Ergang ; Barr, Matthew G. ; Kilcoyne, a. L. D. ; Zhou, Xiaojing ; Dastoor, Paul ; Moons, Ellen: Vertical and lateral morphology effects on solar cell performance for a thiophene–quinoxaline copolymer:PC 70 BM blend. In: *J. Mater. Chem. A* 00 (2015), S. 1–10. – ISSN 2050–7488

[26] Kulkarni, AP ; Jenekhe, SA: Blue light-emitting diodes with good spectral stability based on blends of poly (9, 9-dioctylfluorene): interplay between morphology, photophysics, and device. In: *Macromolecules* 36 (2003), S. 5285–5296

[27] Qin, D. S. ; Li, D. C. ; Wang, Y. ; Zhang, J. D. ; Xie, Z. Y. ; Wang, G. ; Wang, L. X. ; Yan, D. H.: Effects of the morphologies and structures of light-emitting layers on the performance of organic electroluminescent devices. In: *Applied Physics Letters* 78 (2001), Nr. 4, S. 437. – ISSN 00036951

[28] Rivnay, Jonathan ; Jimison, Leslie H. ; Northrup, John E. ; Toney, Michael F. ; Noriega, Rodrigo ; Lu, Shaofeng ; Marks, Tobin J. ; Facchetti, Antonio ; Salleo, Alberto: Large modulation of carrier transport by grain-boundary molecular packing and microstructure in organic thin films. In: *Nature materials* 8 (2009), Dezember, Nr. 12, S. 952–8. – ISSN 1476–1122

[29] Duhm, Steffen ; Heimel, Georg ; Salzmann, Ingo ; Glowatzki, Hendrik ; Johnson, Robert L. ; Vollmer, Antje ; Rabe, Jürgen P ; Koch, Norbert: Orientation-dependent ionization energies and interface dipoles in ordered molecular assemblies. In: *Nature materials* 7 (2008), April, Nr. 4, S. 326–32. – ISSN 1476–1122

[30] Chesterfield, RJ ; McKeen, JC: Organic thin film transistors based on N-alkyl perylene diimides: Charge transport kinetics as a function of gate voltage and temperature. In: *The Journal of Physical Chemistry B* 108 (2004), S. 19281–19292

[31] Anthony, John E.: Organic electronics: addressing challenges. In: *Nature materials* 13 (2014), August, Nr. 8, S. 773–5. – ISSN 1476–1122

[32] Dürr, A. ; Schreiber, F. ; Ritley, K. ; Kruppa, V. ; Krug, J. ; Dosch, H. ; Struth, B.: Rapid roughening in thin film growth of an organic semiconductor (diindenoperylene). In: *Physical Review Letters* 90 (2003), Januar, Nr. 1, S. 016104. – ISSN 0031–9007

[33] Ruiz, Ricardo ; Nickel, Bert ; Koch, Norbert ; Feldman, Leonard ; Haglund, Richard ; Kahn, Antoine ; Family, Fereydoon ; Scoles, Giacinto: Dynamic scaling, island size distribution, and morphology in the aggregation regime of submonolayer pentacene films. In: *Physical Review Letters* 91 (2003), September, Nr. 13, S. 136102. – ISSN 0031–9007

[34] Hlawacek, Gregor ; Puschnig, Peter ; Frank, Paul ; Winkler, Adolf ; Ambrosch-Draxl, Claudia ; Teichert, Christian: Characterization of step-edge barriers in organic thin-film growth. In: *Science (New York, N.Y.)* 321 (2008), Juli, Nr. 5885, S. 108–111. – ISSN 1095–9203

[35] Liu, H. ; Lin, Z. ; Zhigilei, L.V. ; Reinke, P.: Fractal structures in fullerene layers: simulation of the growth process. In: *Journal of Physical Chemistry C* 112 (2008), März, Nr. 12, S. 4687–4695. – ISSN 1932–7447

[36] Loske, Felix ; Lübbe, Jannis ; Schütte, Jens ; Reichling, Michael ; Kühnle, Angelika: Quantitative description of C60 diffusion on an insulating surface. In: *Physical Review B* 82 (2010), Oktober, Nr. 15, S. 155428. – ISSN 1098–0121

[37] Körner, Martin ; Loske, Felix ; Einax, Mario ; Kühnle, Angelika ; Reichling, Michael ; Maass, Philipp: Second-Layer Induced Island Morphologies in Thin-Film Growth of Fullerenes. In: *Physical Review Letters* 107 (2011), Juni, Nr. 1, S. 016101. – ISSN 0031–9007

[38] Einax, Mario ; Dieterich, Wolfgang ; Maass, Philipp: Colloquium: Cluster growth on surfaces: Densities, size distributions, and morphologies. In: *Reviews of Modern Physics* 85 (2013), Juli, Nr. 3, S. 921–939. – ISSN 0034–6861

[39] Krause, B ; Schreiber, F ; Dosch, H ; Pimpinelli, A ; Seeck, O. H.: Temperature dependence of the 2D-3D transition in the growth of PTCDA on Ag(111): a real-time X-ray and kinetic Monte Carlo study. In: *Europhysics Letters (EPL)* 65 (2004), Februar, Nr. 3, S. 372–378. – ISSN 0295–5075

[40] Goose, Joseph E. ; First, Eric L. ; Clancy, Paulette: Nature of step-edge barriers for small organic molecules. In: *Physical Review B* 81 (2010), Mai, Nr. 20, S. 205310. – ISSN 1098–0121

[41] Fendrich, M ; Krug, J: Ehrlich-Schwoebel effect for organic molecules: Direct calculation of the step-edge barrier using empirical potentials. In: *Physical Review B* 76 (2007), S. 121302

[42] Mayer, Alex ; Ruiz, Ricardo ; Zhou, Hua ; Headrick, Randall ; Kazimirov, Alexander ; Malliaras, George: Growth dynamics of pentacene thin films: Real-time synchrotron x-ray scattering study. In: *Physical Review B* 73 (2006), Mai, Nr. 20, S. 205307. – ISSN 1098–0121

[43] Voter, AF: Introduction to the kinetic Monte Carlo method. In: *Radiation Effects in Solids NATO Science Series Vol. 235*. Springer Netherlands, 2007, Kapitel 1, S. 1–23

[44] Teichert, Ch. ; Ammer, Ch. ; Klaua, M.: Step formation on the ion-bombarded Ag(100) surface studied by LEED and Monte Carlo simulations. In: *Physica Status Solidi (a)* 146 (1994), November, Nr. 1, S. 223–242. – ISSN 00318965

[45] Kürpick, U ; Rahman, TS: Diffusion processes relevant to homoepitaxial growth on Ag (100). In: *Physical Review B* 57 (1998), Nr. 4, S. 2482–2492

[46] Cox, Erik ; Li, Maozhi ; Chung, Po-Wen ; Ghosh, C. ; Rahman, T. ; Jenks, C. ; Evans, J. ; Thiel, P.: Temperature dependence of island growth shapes during submonolayer deposition of Ag on Ag(111). In: *Physical Review B* 71 (2005), März, Nr. 11, S. 115414. – ISSN 1098–0121

[47] Michely, Thomas ; Krug, Joachim: *Islands, Mounds, and Atoms: Patterns and Processes in Crystal Growth Far From Equilibrium (Springer Series in Surface Sciences)*. Springer Berlin Heidelberg, 2003

[48] Evans, J.W. ; Thiel, P.A. ; Bartelt, M.C.: Morphological evolution during epitaxial thin film growth: Formation of 2D islands and 3D mounds. In: *Surface Science Reports* 61 (2006), April, Nr. 1-2, S. 1–128. – ISSN 01675729

[49] Ferguson, J. D. ; Arikan, G. ; Dale, D. S. ; Woll, A. R. ; Brock, J. D.: Measurements of surface diffusivity and coarsening during pulsed laser deposition. In: *Physical Review Letters* 103 (2009), Dezember, Nr. 25, S. 256103. – ISSN 0031–9007

[50] Ganapathy, Rajesh ; Buckley, Mark R. ; Gerbode, Sharon J. ; Cohen, Itai: Direct measurements of island growth and step-edge barriers in colloidal epitaxy. In: *Science (New York, N.Y.)* 327 (2010), Januar, Nr. 5964, S. 445–448. – ISSN 1095–9203

[51] Bohlein, Thomas ; Mikhael, Jules ; Bechinger, Clemens: Observation of kinks and antikinks in colloidal monolayers driven across ordered surfaces. In: *Nature Materials* 11 (2012), Februar, Nr. 2, S. 126–130. – ISSN 1476–1122

[52] Frenkel, Daan ; Wales, David J.: Colloidal self-assembly: designed to yield. In: *Nature Materials* 10 (2011), Juli, Nr. 6, S. 410–411. – ISSN 1476–1122

[53] Heath, Jim ; O'Brien, Sean ; Curl, Robert: 25 years of C60. In: *Nature Nanotechnology* 5 (2010), Oktober, Nr. 10, S. 691. – ISSN 1748–3395

[54] Kroto, HW ; Heath, JR ; O'Brien, SC ; Curl, RF ; Smalley, RE: C60: Buckminsterfullerene. In: *Nature* 318 (1985), S. 162–163

[55] Kroto, Harry ; Heath, Jim ; O'Brien, Sean ; Curl, Robert ; Smalley, Richard: Awesome allotropy. In: *Nature Materials* 9 (2010), November, Nr. 11, S. 867. – ISSN 1476–1122

[56] Kowarik, S. ; Gerlach, A. ; Sellner, S. ; Schreiber, F. ; Cavalcanti, L. ; Konovalov, O.: Real-time observation of structural and orientational transitions during growth of organic thin films. In: *Physical Review Letters* 96 (2006), März, Nr. 12, S. 125504. – ISSN 0031–9007

[57] Renaud, Gilles ; Lazzari, Rémi ; Revenant, Christine ; Barbier, Antoine ; Noblet, Marion ; Ulrich, Olivier ; Leroy, Frédéric ; Jupille, Jacques ; Borensztein, Yves ; Henry, Claude R. ; Deville, Jean-Paul ; Scheurer, Fabrice ; Mane-Mane, Jeannot ; Fruchart, Olivier: Real-time monitoring of growing nanoparticles. In: *Science (New York, N.Y.)* 300 (2003), Mai, Nr. 5624, S. 1416–1419. – ISSN 1095–9203

[58] Schwartzkopf, Matthias ; Buffet, Adeline ; Körstgens, Volker ; Metwalli, Ezzeldin ; Schlage, Kai ; Benecke, Gunthard ; Perlich, Jan ; Rawolle, Monika ; Rothkirch, André ; Heidmann, Berit ; Herzog, Gerd ; Müller-Buschbaum, Peter ; Röhlsberger, Ralf ; Gehrke, Rainer ; Stribeck, Norbert ; Roth, Stephan V.: From atoms to layers: in situ gold cluster growth kinetics during sputter deposition. In: *Nanoscale* 5 (2013), Juni, Nr. 11, S. 5053–5062. – ISSN 2040–3372

[59] Nolte, Philipp ; Stierle, Andreas ; Kasper, Nikolai: Reversible shape changes of Pd nanoparticles on MgO (100). In: *Nano Letters* 11 (2011), S. 4697–4700

[60] Gustafson, J ; Shipilin, M ; Zhang, C ; Stierle, A ; Hejral, U ; Ruett, U ; Gutowski, O ; Carlsson, PA ; Skoglundh, M ; Lundgren, E: High-Energy Surface X-ray Diffraction for Fast Surface Structure Determination. In: *Science* 343 (2014), S. 758–761

[61] Clancy, Paulette: Application of Molecular Simulation Techniques to the Study of Factors Affecting the Thin-Film Morphology of Small-Molecule Organic Semiconductors. In: *Chemistry of Materials* 23 (2011), Februar, Nr. 3, S. 522–543. – ISSN 0897–4756

[62] Kleppmann, Nicola ; Klapp, Sabine H. L.: Particle-resolved dynamics during multilayer growth of C60. In: *Physical Review B* 91 (2015), Januar, Nr. 4, S. 045436. – ISSN 1098–0121

[63] Khlobystov, Andrei ; Britz, David ; Ardavan, Arzhang ; Briggs, G.: Observation of ordered phases of fullerenes in carbon nanotubes. In: *Physical Review Letters* 92 (2004), Juni, Nr. 24, S. 245507. – ISSN 0031–9007

[64] Hagen, M.H.J. ; Meijer, E.J. ; Mooij, G.C.A.M. ; Frenkel, D. ; Lekkerkerker, H.N.W.: Does C60 have a liquid phase? In: *Nature* 365 (1993), S. 425–426

[65] Tewari, S. P. ; Dhingra, Grima ; Silotia, Poonam: Collective Dynamics of a Nano-Fluid: Fullerene, C60. In: *International Journal of Modern Physics B* 24 (2010), September, Nr. 22, S. 4281–4292. – ISSN 0217–9792

[66] DiStasio, Robert A. ; Lilienfeld, O. A. ; Tkatchenko, Alexandre: Collective many-body van der Waals interactions in molecular systems. In: *Proceedings of the National Academy of Sciences of the United States of America* 109 (2012), September, Nr. 37, S. 14791–5. – ISSN 1091–6490

[67] Tkatchenko, Alexandre ; DiStasio, Robert A. ; Car, Roberto ; Scheffler, Matthias: Accurate and Efficient Method for Many-Body van der Waals Interactions. In: *Physical Review Letters* 108 (2012), Juni, Nr. 23, S. 236402. – ISSN 0031–9007

[68] Schmidle, Heiko ; Jäger, Sebastian ; Hall, Carol K. ; Velev, Orlin D. ; Klapp, Sabine H. L.: Two-dimensional colloidal networks induced by a uni-axial external field. In: *Soft Matter* 9 (2013), Nr. 8, S. 2518–2524. – ISSN 1744–683X

[69] Klapp, Sabine H. L. ; Grandner, Stefan ; Zeng, Yan ; Klitzing, Regine von: Charged silica suspensions as model materials for liquids in confined geometries. In: *Soft Matter* 6 (2010), Nr. 10, S. 2330–2336. – ISSN 1744–683X

[70] Burke, S. ; Mativetsky, J. ; Fostner, S. ; Grütter, P.: C60 on alkali halides: Epitaxy and morphology studied by noncontact AFM. In: *Physical Review B* 76 (2007), Juli, Nr. 3, S. 035419. – ISSN 1098–0121

[71] Burke, S A. ; Topple, J M. ; Grütter, P: Molecular dewetting on insulators. In: *Journal of physics. Condensed matter : an Institute of Physics journal* 21 (2009), Oktober, Nr. 42, S. 423101. – ISSN 1361–648X

[72] Lendlein, Andreas ; Shastri, V P.: Stimuli-sensitive polymers. In: *Advanced materials (Deerfield Beach, Fla.)* 22 (2010), August, Nr. 31, S. 3344–7. – ISSN 1521–4095

[73] Liu, ZF ; Hashimoto, K ; Fujishima, A: Photoelectrochemical information storage using an azobenzene derivative. In: *Nature* 347 (1990), S. 658–660

[74] Baughman, RH: Playing nature's game with artificial muscles. In: *Science* 308 (2005), Nr. April, S. 63–66

[75] Shen, Xingyuan ; Viney, Christopher ; Johnson, Erin R. ; Wang, Changchun ; Lu, Jennifer Q.: Large negative thermal expansion of a polymer driven by a submolecular conformational change. In: *Nature Chemistry* 5 (2013), Dezember, Nr. 12, S. 1035–41. – ISSN 1755–4349

[76] Browne, WR ; Feringa, BL: Making molecular machines work. In: *Nature nanotechnology* 1 (2006), S. 25–35

[77] Bléger, David ; Liebig, Tobias ; Thiermann, Raphael ; Maskos, Michael ; Rabe, Jürgen P ; Hecht, Stefan: Light-orchestrated macromolecular "accordions": reversible photoinduced shrinking of rigid-rod polymers. In: *Angewandte Chemie (International ed. in English)* 50 (2011), Dezember, Nr. 52, S. 12559–63. – ISSN 1521–3773

[78] Bléger, David ; Yu, Zhilin ; Hecht, Stefan: Toward optomechanics: maximizing the photodeformation of individual molecules. In: *Chemical communications (Cambridge, England)* 47 (2011), Dezember, Nr. 45, S. 12260–6. – ISSN 1364–548X

[79] Kudernac, Tibor ; Ruangsupapichat, Nopporn ; Parschau, Manfred ; Maciá, Beatriz ; Katsonis, Nathalie ; Harutyunyan, Syuzanna R. ; Ernst, Karl-Heinz ; Feringa, Ben L.: Electrically driven directional motion of a four-wheeled molecule on a metal surface. In: *Nature* 479 (2011), November, Nr. 7372, S. 208–11. – ISSN 1476–4687

[80] Behl, Marc ; Razzaq, Muhammad Y. ; Lendlein, Andreas: Multifunctional shape-memory polymers. In: *Advanced materials (Deerfield Beach, Fla.)* 22 (2010), August, Nr. 31, S. 3388–410. – ISSN 1521–4095

[81] Krauss, Tobias N. ; Barrena, Esther ; Zhang, Xue N. ; Oteyza, Dimas G. ; Major, János ; Dehm, Volker ; Würthner, Frank ; Cavalcanti, Leide P. ; Dosch, Helmut: Three-dimensional molecular packing of thin organic films of PTCDI-C8 determined by surface X-ray diffraction. In: *Langmuir : the ACS journal of surfaces and colloids* 24 (2008), November, Nr. 22, S. 12742–4. – ISSN 0743–7463

[82] Lind, Cora: Two Decades of Negative Thermal Expansion Research: Where Do We Stand? In: *Materials* 5 (2012), Juni, Nr. 12, S. 1125–1154. – ISSN 1996–1944

[83] Miller, W. ; Smith, C. W. ; Mackenzie, D. S. ; Evans, K. E.: Negative thermal expansion: a review. In: *Journal of Materials Science* 44 (2009), Juli, Nr. 20, S. 5441–5451. – ISSN 0022–2461

[84] Takenaka, Koshi: Negative thermal expansion materials: technological key for control of thermal expansion. In: *Science and Technology of Advanced Materials* 13 (2012), Februar, Nr. 1, S. 013001. – ISSN 1468–6996

[85] Mary, TA ; Evans, JSO ; Vogt, T ; Sleight, AW: Negative Thermal Expansion from 0.3 to 1050 Kelvin in ZrW208. In: *Science* 2272 (1994), S. 90–92

[86] Evans, JSO ; Mary, TA: Negative thermal expansion in ZrW2O8 and HfW2O8. In: *Chemistry of Materials* 4756 (1996), Nr. 6, S. 2809–2823

[87] Bridges, F. ; Keiber, T. ; Juhas, P. ; Billinge, SJL ; Sutton, L. ; Wilde, J. ; Kowach, GR: Local Vibrations and Negative Thermal Expansion in ZrW2O8. In: *Physical Review Letters* 112 (2014), Januar, Nr. 4, S. 045505. – ISSN 0031–9007

[88] Wu, Yue ; Kobayashi, Atsushi ; Halder, GJ ; Peterson, VK ; Chapman, KW ; Lock, Nina ; Southon, PD ; Kepert, CJ: Negative Thermal Expansion in the Metal-Organic Framework Material Cu 3 (1,3,5-benzenetricarboxylate) 2. In: *Angewandte Chemie* 120 (2008), November, Nr. 46, S. 9061–9064. – ISSN 00448249

[89] Han, SS ; Goddard, WA: Metal-organic frameworks provide large negative thermal expansion behavior. In: *The Journal of Physical Chemistry C* (2007), S. 15185–15191

[90] Birkedal, Henrik ; Schwarzenbach, Dieter ; Pattison, Philip: Observation of uniaxial negative thermal expansion in an organic crystal. In: *Angewandte Chemie International Edition* 41 (2002), Nr. 5, S. 1981–1983

[91] Das, Dinabandhu ; Jacobs, Tia ; Barbour, Leonard J.: Exceptionally large positive and negative anisotropic thermal expansion of an organic crystalline material. In: *Nature Materials* 9 (2010), Januar, Nr. 1, S. 36–9. – ISSN 1476–1122

[92] Das, Dinabandhu ; Jacobs, Tia ; Pietraszko, Adam ; Barbour, Leonard J.: Anomalous thermal expansion of an organic crystal–implications for elucidating the mechanism of an enantiotropic phase transformation. In: *Chemical Communications (Cambridge, England)* 47 (2011), Juni, Nr. 21, S. 6009–11. – ISSN 1364–548X

[93] Haas, S. ; Batlogg, B. ; Besnard, C. ; Schiltz, M. ; Kloc, C. ; Siegrist, T.: Large uniaxial negative thermal expansion in pentacene due to steric hindrance. In: *Physical Review B* 76 (2007), November, Nr. 20, S. 205203. – ISSN 1098–0121

[94] Schwoerer, M ; Wolf, Hans C.: *Organic Molecular Solids*. Weinheim : Wiley-VCH Verlag, 2007

[95] Bernstein, Joel ; Davis, RE ; Shimoni, L ; Chang, NL: Patterns in hydrogen bonding: functionality and graph set analysis in crystals. In: *Angewandte Chemie International Edition* 34 (1995), S. 1555–1573

[96] Ehrlich, Gert ; Hudda, F.G.: Atomic view of surface self-diffusion: tungsten on tungsten. In: *The Journal of Chemical Physics* 44 (1966), Nr. 3, S. 1039–1049. – ISSN 00219606

[97] Schwoebel, Richard L. ; Shipsey, Edward J.: Step motion on crystal surfaces. In: *Journal of Applied Physics* 37 (1966), Nr. 10, S. 3682–3686. – ISSN 00218979

[98] Krug, Joachim: Four lectures on the physics of crystal growth. In: *Physica A: Statistical Mechanics and its Applications* 313 (2002), S. 47–82

[99] Frank, C. ; Novák, J. ; Banerjee, R. ; Gerlach, A. ; Schreiber, F. ; Vorobiev, A. ; Kowarik, S.: Island size evolution and molecular diffusion during growth of organic thin films followed by time-resolved specular and off-specular scattering. In: *Physical Review B* 90 (2014), Juli, Nr. 4, S. 045410. – ISSN 1098–0121

[100] Kowarik, S. ; Gerlach, A. ; Skoda, M. W. A. ; Sellner, S. ; Schreiber, F.: Real-time studies of thin film growth: measurement and analysis of X-ray growth oscillations beyond the anti-Bragg point. In: *The European Physical Journal Special Topics* 167 (2009), März, Nr. 1, S. 11–18. – ISSN 1951–6355

[101] Tromp, RM ; Hannon, JB: Thermodynamics of nucleation and growth. In: *Surface Review and Letters* 9 (2002), S. 1565–1593

[102] Venables, J.A. ; Spiller, G.D.T. ; Hanbücken, M.: Nucleation and growth of thin films. In: *Rep. Prog. Phys* 47 (1984), S. 399–459

[103] Zinsmeister, G: Theory of thin film condensation. Part B: solution of the simplified condensation equation. In: *Thin Solid Films* 2 (1968), Nr. April, S. 497–507

[104] Zinsmeister, G: Theory of thin film condensation part C: Aggregate size distribution in island films. In: *Thin Solid Films* 4 (1969), S. 363–386

[105] Zinsmeister, G: Theory of thin film condensation Part D: Influence of a variable collision factor. In: *Thin Solid Films* 7 (1971), Nr. 1971, S. 51–75

[106] Stowell, MJ ; Hutchinson, TE: Nucleation kinetics in thin film growth III transient nucleation and nucleation on preferred substrate sites. In: *Thin Solid Films* 8 (1971), S. 411–425

[107] Venables, JA: Rate equation approaches to thin film nucleation kinetics. In: *Philosophical Magazine* (1973), Nr. August 2012, S. 37–41. ISBN 1478643730

[108] Trofimov, Vladimir I. ; Mokerov, Vladimir G.: Rate equations model for layer epitaxial growth kinetics. In: *Thin Solid Films* 428 (2003), S. 66–71. ISBN 7952033689

[109] Trofimov, V I. ; Mokerov, V G. ; Shumyankov, A G.: Kinetic model for molecular beam epitaxial growth on a singular surface. In: *Thin Solid Films* 306 (1997), Nr. 97, S. 105–111. ISBN 7952033689

[110] Woll, Arthur R. ; Desai, Tushar V. ; Engstrom, James R.: Quantitative modeling of in situ x-ray reflectivity during organic molecule thin film growth. In: *Physical Review B* 84 (2011), August, Nr. 7, S. 075479. – ISSN 1098–0121

[111] Weber, C ; Frank, C ; Bommel, S ; Rukat, T ; Leitenberger, W ; Schäfer, P ; Schreiber, F ; Kowarik, S: Chain-length dependent growth dynamics of n-alkanes on silica investigated by energy-dispersive x-ray reflectivity in situ and in real-time. In: *The Journal of Chemical Physics* 136 (2012), Mai, Nr. 20, S. 204709. – ISSN 1089–7690

[112] Bommel, S. ; Kleppmann, N. ; Weber, C. ; Spranger, H. ; Schäfer, P. ; Novak, J. ; Roth, S.V. ; Schreiber, F. ; Klapp, S.H.L. ; Kowarik, S.: Unravelling the multilayer growth of the fullerene C60 in real time. In: *Nature Communications* 5 (2014), November, S. 5388. – ISSN 2041–1723

[113] Sparenberg, M ; Zykov, A ; Beyer, P ; Pithan, L ; Weber, C ; Garmshausen, Y ; Carla, F ; Hecht, S ; Blumstengel, S ; Henneberger, F ; Kowarik, S: Controlling the growth mode of para-sexiphenyl (6P) on ZnO by partial fluorination. In: *Physical Chemistry Chemical Physics* 16 (2014), S. 26084–26093

[114] Clarke, Shaun ; Vvedensky, Dimitri D.: Growth kinetics and step density in reflection high-energy electron diffraction during molecular-beam epitaxy. In: *Journal of Applied Physics* 63 (1988), Nr. 7, S. 2272–2283. – ISSN 00218979

[115] Oliveira, T. J. ; Aarão Reis, F. D. A.: Scaling in reversible submonolayer deposition. In: *Physical Review B* 87 (2013), Juni, Nr. 23, S. 235430. – ISSN 1098–0121

[116] Gyure, Mark ; Zinck, Jennifer ; Ratsch, Christian ; Vvedensky, Dimitri: Unstable growth on rough surfaces. In: *Physical Review Letters* 81 (1998), November, Nr. 22, S. 4931–4934. – ISSN 0031–9007

[117] Jones, Aleksy ; Ballestad, Anders ; Li, Tian ; Whitwick, Michael ; Rottler, Jörg ; Tiedje, T.: Faceting at the step flow threshold in epitaxial growth on patterned surfaces. In: *Physical Review B* 79 (2009), Mai, Nr. 20, S. 205419. – ISSN 1098–0121

[118] Marmorkos, IK ; Sarma, SD: Atomistic numerical study of molecular-beam-epitaxial growth kinetics. In: *Physical Review B* 45 (1992), Nr. 19, S. 262–272

[119] Morse, PM: Diatomic molecules according to the wave mechanics. II. vibrational levels. In: *Physical Review* 457 (1929), Nr. 1927. `http://journals.aps.org/pr/abstract/10.1103/PhysRev.34.57`

[120] Kittel, C: *Einführung in die Festkörperphysik*. 14. München : Oldenbourg, 2005

[121] Meyer, EA ; Castellano, KC ; Diederich, F: Interactions with aromatic rings in chemical and biological recognition. In: *Angewandte Chemie International Edition* 42 (2003), Nr. 11, S. 1210–1250. ISBN 3528460296

[122] Dresselhaus, MS ; Dresselhaus, G ; Eklund, PC: *Science of Fullerenes and Carbon Nanotubes*. San Diego, USA : Academic Press, 1996

[123] Iijima, S: Helical microtubules of graphitic carbon. In: *Nature* 354 (1991), S. 56–58

[124] Iijima, S ; Ichihashi, T: Single-shell carbon nanotubes of 1-nm diameter. In: *Nature* 363 (1993), S. 603–605

[125] Novoselov, KS ; Geim, AK ; Morozov, SV: Electric field effect in atomically thin carbon films. In: *Science* 306 (2004), S. 666–669

[126] Geim, AK ; Novoselov, KS: The rise of graphene. In: *Nature Materials* 6 (2007), S. 183–191

[127] Krätschmer, W ; Lamb, Lowell D. ; Fostiropoulos, K ; Huffman, Donald R.: Solid C60: a new form of carbon. In: *Nature* 347 (1990), S. 354–358

[128] Boer, Jan L. ; Smaalen, Sander van ; Petricek, Vaclav ; Dusek, Michal ; Verheijen, Marcel A. ; Meijer, G: Hexagonal close-packed C60. In: *Chemical Physics Letters* 219 (1994), S. 469–472

[129] Kroto, HW ; Taylor, R ; Hare, JP ; Dennis, TJS: Crystal structure and bonding of ordered C 60. In: *Nature* 353 (1991), S. 147–149

[130] Heiney, P. A. ; Fischer, J.E. ; McGhie, A.R. ; Romanow, W.J. ; Denenstein, A.M. ; McCauley J.R. ; Smith, A.B. ; Cox, D.E.: Orientational ordering transition in solid C60. In: *Physical Review Letters* 66 (1991), Juni, Nr. 22, S. 2911–2914. – ISSN 1079–7114

[131] Schull, G. ; Berndt, R.: Orientationally Ordered (7×7) Superstructure of C60 on Au(111). In: *Physical Review Letters* 99 (2007), November, Nr. 22, S. 226105. – ISSN 0031–9007

[132] Arndt, M ; Nairz, O ; Vos-Andreae, J ; Keller, C ; Zouw, G van d. ; Zeilinger, A: Wave-particle duality of C60 molecules. In: *Nature* 401 (1999), Oktober, Nr. 6754, S. 680–2. – ISSN 0028–0836

[133] Park, H ; Park, Jiwoong ; Lim, AKL ; Anderson, EH: Nanomechanical oscillations in a single-C60 transistor. In: *Nature* 407 (2002), S. 57–60

[134] Winkelmann, Clemens B. ; Roch, Nicolas ; Wernsdorfer, Wolfgang ; Bouchiat, Vincent ; Balestro, Franck: Superconductivity in a single-C60 transistor. In: *Nature Physics* 5 (2009), Oktober, Nr. 12, S. 876–879. – ISSN 1745–2473

[135] Han, Sijin ; Yuan, Yanyan ; Lu, Zheng-Hong: Highly efficient organic light-emitting diodes with metal/fullerene anode. In: *Journal of Applied Physics* 100 (2006), Nr. 7, S. 074504. – ISSN 00218979

[136] Kanwal, Alokik ; Chhowalla, Manish: Stable, three layered organic memory devices from C[sub 60] molecules and insulating polymers. In: *Applied Physics Letters* 89 (2006), Nr. 20, S. 203103. – ISSN 00036951

[137] Peumans, P. ; Forrest, S. R.: Very-high-efficiency double-heterostructure copper phthalocyanine/C[sub 60] photovoltaic cells. In: *Applied Physics Letters* 79 (2001), Nr. 1, S. 126. – ISSN 00036951

[138] Wang, Z. B. ; Helander, M. G. ; Greiner, M. T. ; Qiu, J. ; Lu, Z. H.: Energy-level alignment and charge injection at metal/C60/organic interfaces. In: *Applied Physics Letters* 95 (2009), Nr. 4, S. 043302. – ISSN 00036951

[139] Lee, Jun Y.: Efficient hole injection in organic light-emitting diodes using C60 as a buffer layer for Al reflective anodes. In: *Applied Physics Letters* 88 (2006), Nr. 7, S. 073512. – ISSN 00036951

[140] Girifalco, LA: Interaction potential for C60 molecules. In: *The Journal of Physical Chemistry* 2 (1991), S. 5370–5371. ISBN 0022365419

[141] Likos, CN: Effective interactions in soft condensed matter physics. In: *Physics Reports* 348 (2001), S. 267–439. ISBN 4921181136

[142] Asakura, Sho ; Oosawa, Fumio: On Interaction between Two Bodies Immersed in a Solution of Macromolecules. In: *The Journal of Chemical Physics* 22 (1954), Nr. 7, S. 1255. – ISSN 00219606

[143] Lekkerkerker, Henk N. ; Tuinier, Remco: *Colloids and the depletion interaction*. Springer Netherlands, 2011

[144] Dhont, KG ; Möbius, D (Hrsg.) ; Miller, R (Hrsg.): *An introduction to dynamics of colloids*. Elsevier Science & Technology, 1996

[145] Tatemichi, Shuhei ; Ichikawa, Musubu ; Koyama, Toshiki ; Taniguchi, Yoshio: High mobility n-type thin-film transistors based on N,N'-ditridecyl perylene diimide with thermal treatments. In: *Applied Physics Letters* 89 (2006), Nr. 11, S. 112108. – ISSN 00036951

[146] Rolin, C. ; Vasseur, K. ; Schols, S. ; Jouk, M. ; Duhoux, G. ; Müller, R. ; Genoe, J. ; Heremans, P.: High mobility electron-conducting thin-film transistors by organic vapor phase deposition. In: *Applied Physics Letters* 93 (2008), Nr. 3, S. 033305. – ISSN 00036951

[147] Malenfant, Patrick R. L. ; Dimitrakopoulos, Christos D. ; Gelorme, Jeffrey D. ; Kosbar, Laura L. ; Graham, Teresita O. ; Curioni, Alessandro ; Andreoni, Wanda: N-type organic thin-film transistor with high field-effect mobility based on a N,N'-dialkyl-3,4,9,10-perylene tetracarboxylic diimide derivative. In: *Applied Physics Letters* 80 (2002), Nr. 14, S. 2517. – ISSN 00036951

[148] Karak, S ; Reddy, VS ; Ray, SK ; Dhar, A: Organic photovoltaic devices based on pentacene/ N, N'-dioctyl-3, 4, 9, 10-perylenedicarboximide heterojunctions. In: *Organic Electronics* 10 (2009), S. 1006–1010

[149] Krauss, Tobias N. ; Barrena, Esther ; Oteyza, Dimas G D. ; Zhang, Xue N. ; Dehm, Volker ; Wu, Frank ; Dosch, Helmut: X-ray / Atomic Force Microscopy Study of the Temperature-Dependent Multilayer Structure of PTCDI-C8 Films on SiO2. In: *The Journal of Physical Chemistry C* 113 (2009), Nr. 11, S. 4502–4506. – ISSN 19327447

[150] Ostendorf, F ; Schmitz, C ; Hirth, S ; Kühnle, A ; Kolodziej, J J. ; Reichling, M: How flat is an air-cleaved mica surface? In: *Nanotechnology* 19 (2008), Juli, Nr. 30, S. 305705. – ISSN 0957–4484

[151] Nolte, P ; Stierle, A ; Jin-Phillipp, NY ; Kasper, N ; Schulli, TU ; Dosch, H: Shape changes of supported Rh nanoparticles during oxidation and reduction cycles. In: *Science* 321 (2008), S. 1654–1659

[152] Banerjee, R. ; Novák, J. ; Frank, C. ; Lorch, C. ; Hinderhofer, A. ; Gerlach, A. ; Schreiber, F.: Evidence for Kinetically Limited Thickness Dependent Phase Separation in Organic Thin Film Blends. In: *Physical Review Letters* 110 (2013), Mai, Nr. 18, S. 185506. – ISSN 0031–9007

[153] Als-Nielsen, Jens ; McMorrow, Des: *Elements of Modern X-Ray Physics*. New York : Wiley, 2001

[154] Cromer, DT ; Mann, JB: X-RAY SCATTERING FACTORS COMPUTED FROM NUMERICAL HARTREE-FOCK WAVE FUNCTIONS. In: *Acta Crystallographica Section A - Crystal Physics Diffraction Theoretical and General Crystallography* A 24 (1968), S. 321

[155] Stewart, Robert F. ; Davidson, Ernest R. ; Simpson, William T.: Coherent X-Ray Scattering for the Hydrogen Atom in the Hydrogen Molecule. In: *The Journal of Chemical Physics* 42 (1965), Nr. 9, S. 3175. – ISSN 00219606

[156] Muhammad, Wazir ; Lee, Sang H.: New empirical equation for the atomic form factor function in the momentum transfer range, q=0-50 A(-1) for the elements in the range 1 <= Z <= 30. In: *PloS one* 8 (2013), Januar, Nr. 8, S. e69608. – ISSN 1932–6203

[157] Henke, BL ; Gullikson, EM ; Davis, JC: X-ray interactions: photoabsorption, scattering, transmission, and reflection at E= 50-30,000 eV, Z= 1-92. In: *Atomic data and nuclear data tables* 54 (1993), S. 181–342

[158] Brentano, J: Focussing method of crystal powder analysis by X-rays. In: *Proceedings of the Physical Society of London* 184 (1924)

[159] Ruiz, Ricardo ; Choudhary, Devashish ; Nickel, Bert ; Toccoli, Tullio ; Chang, Kee-Chul ; Mayer, Alex C. ; Clancy, Paulette ; Blakely, Jack M. ; Headrick, Randall L. ; Iannotta, Salvatore ; Malliaras, George G.: Pentacene Thin Film Growth. In: *Chemistry of Materials* 16 (2004), Nr. 23, S. 4497–4508. – ISSN 08974756

[160] Dosch, Helmut: *Critical Phenomena at Surfaces and Interfaces: Evanescent X-Ray and Neutron Scattering*. Berlin Heidelberg : Springer Verlag, 1992

[161] Sinha, SK ; Sirota, EB ; Garoff, S ; Stanley, HB: X-ray and neutron scattering from rough surfaces. In: *Physical Review B* 38 (1988), Nr. 4, S. 2297–2311

[162] Kowarik, Stefan ; Gerlach, Alexander ; Sellner, Stefan ; Cavalcanti, Leide ; Konovalov, Oleg ; Schreiber, Frank: Real-time X-ray diffraction measurements of structural dynamics and polymorphism in diindenoperylene growth. In: *Applied Physics A* 95 (2008), Dezember, Nr. 1, S. 233–239. – ISSN 0947–8396

[163] Pithan, Linus: *Structure, optical properties and light-controlled molecular self-assembly of organic thin lms*, Technische Universität Berlin, Master Thesis, 2013

[164] Lazzari, Rémi: IsGISAXS : a program for grazing-incidence small-angle X-ray scattering analysis of supported islands. In: *Journal of Applied Crystallography* 35 (2002), Juli, Nr. 4, S. 406–421. – ISSN 0021–8898

[165] Babonneau, David: FitGISAXS : software package for modelling and analysis of GISAXS data using IGOR Pro. In: *Journal of Applied Crystallography* 43 (2010), Juli, Nr. 4, S. 929–936. – ISSN 0021–8898

[166] Sarkar, Kuhu ; Schaffer, Christoph J. ; González, Daniel M. ; Naumann, Anna ; Perlich, Jan ; Müller-Buschbaum, Peter: Tuning the pore size of ZnO nano-grids via time-dependent solvent annealing. In: *Journal of Materials Chemistry A* 2 (2014), Nr. 19, S. 6945. – ISSN 2050–7488

[167] Müller-Buschbaum, P: A Basic Introduction to Grazing Incidence Small-Angle X-Ray Scattering. In: Ezquerra, T.A. (Hrsg.) ; Garcia-Gutierrez, M.C. (Hrsg.) ; Nogales, A. (Hrsg.) ; Gomez, MA (Hrsg.): *Applications of Synchrotron Light to Scattering and Diffraction in Materials and Life Sciences*. Springer Berlin Heidelberg, 2009, Kapitel 3, S. 61–89

[168] Yoneda, Y: Anomalous surface reflection of X-rays. In: *Physical Review* 131 (1963), Nr. 5, S. 2010–2013

[169] Buffet, Adeline ; Rothkirch, André ; Döhrmann, Ralph ; Körstgens, Volker ; Abul Kashem, Mottakin M. ; Perlich, Jan ; Herzog, Gerd ; Schwartzkopf, Matthias ; Gehrke, Rainer ; Müller-Buschbaum, Peter ; Roth, Stephan V.: P03, the microfocus and nanofocus x-ray scattering (MiNaXS) beamline of the PETRA III storage ring: the microfocus endstation. In: *Journal of Synchrotron Radiation* 19 (2012), Juli, S. 647–653. – ISSN 1600–5775

[170] Santoro, G ; Buffet, A ; Döhrmann, R ; Yu, S ; Körstgens, V ; Müller-Buschbaum, P ; Gedde, U ; Hedenqvist, M ; Roth, S V.: Use of intermediate focus for grazing incidence small and wide angle x-ray scattering experiments at the beamline P03 of PETRA III, DESY. In: *The Review of scientific instruments* 85 (2014), April, Nr. 4, S. 043901. – ISSN 1089–7623

[171] Wikipedia: *Atomic Force Microscopy (AFM)*. `http://en.wikipedia.org/wiki/Atomic_force_microscopy`. Version: 2015

[172] Zhong, Q ; Inniss, D ; Kjoller, K ; Elings, VB: Fractured polymer/silica fiber surface studied by tapping mode atomic force microscopy. In: *Surface Science Letters* 290 (1993), S. L688–L692

[173] Müller-Buschbaum, Peter: Grazing incidence small-angle X-ray scattering : an advanced scattering technique for the investigation of nanostructured polymer films. In: *Analytical and Bioanalytical Chemistry* 376 (2003), S. 3–10. ISBN 0021600318692

[174] Henke, S. ; Thürer, K.H. ; Lindner, J.K.N. ; Rauschenbach, B. ; Stritzker, B.: Structural characterization of the temperature dependence of C60-thin films on mica (001) by x-ray diffraction. In: *Journal of Applied Physics* 76 (1994), Nr. 6, S. 3337–3340. – ISSN 00218979

[175] Felici, Roberto ; Pedio, Maddalena ; Borgatti, Francesco ; Iannotta, Salvatore ; Capozi, Mario ; Ciullo, Giuseppe ; Stierle, Andreas: X-ray-diffraction characterization of Pt(111) surface nanopatterning induced by C60 adsorption. In: *Nature Materials* 4 (2005), September, Nr. 9, S. 688–692. – ISSN 1476–1122

[176] Henke, S. ; Thürer, K.H. ; Geier, S.: X-ray pole-figure study of the epitaxial growth of C60 thin films on mica (001). In: *Applied Physics A* 389 (1995), S. 383–389

[177] Fenter, P. ; Schreiber, F. ; Zhou, L. ; Eisenberger, P. ; Forrest, S.: In situ studies of morphology, strain, and growth modes of a molecular organic thin film. In: *Physical Review B* 56 (1997), August, Nr. 6, S. 3046–3053. – ISSN 0163–1829

[178] Meyer zu Heringdorf, F J. ; Reuter, M C. ; Tromp, R M.: Growth dynamics of pentacene thin films. In: *Nature* 412 (2001), August, Nr. 6846, S. 517–20. – ISSN 0028–0836

[179] Khokhar, Fawad S. ; Hlawacek, Gregor ; Gastel, Raoul van ; Zandvliet, Harold J W. ; Teichert, Christian ; Poelsema, Bene: The influence of substrate

temperature on growth of para-sexiphenyl thin films on Ir{111} supported graphene studied by LEEM. In: *Surface science* 606 (2012), Februar, Nr. 3-4, S. 475–480. – ISSN 0039–6028

[180] Ruoff, RS ; Thornton, T ; Smith, D: Density of fullerene containing soot as determined by helium pycnometry. In: *Chemical Physics Letters* 186 (1991), Nr. 43, S. 456–458

[181] Anthony, John W. ; Bideaux, Richard A. ; Bladh, Kenneth W. ; Nichols, Monte C.: *Handbook of Mineralogy*. Mineralogical Society of America, 2001

[182] Jeng, U-Ser ; Lin, Tsang-Lang ; Shin, Kwanwoo ; Lee, Hsin-Yi ; Hsu, Chia-Hung ; Chi, Zau-Ann ; Shih, Ming C. ; Torikai, Naoya: Neutron and X-ray Scattering on the Monolayer Structure of a Lecithin Fullerene-Derivative. In: *Journal of Nanoscience and Nanotechnology* 7 (2007), April, Nr. 4, S. 1406–1413. – ISSN 15334880

[183] Rols, S. ; Cambedouzou, J. ; Chorro, M. ; Schober, H. ; Agafonov, V. ; Launois, P. ; Davydov, V. ; Rakhmanina, A. ; Kataura, H. ; Sauvajol, J.-L.: How Confinement Affects the Dynamics of C60 in Carbon Nanopeapods. In: *Physical Review Letters* 101 (2008), August, Nr. 6, S. 065507. – ISSN 0031–9007

[184] Shi, ZP ; Zhang, Z ; Swan, AK ; Wendelken, JF: Dimer Shearing as a Novel Mechanism for Cluster Diffusion and Dissociation on Metal (100) Surfaces. In: *Physical Review Letters* 76 (1996), Juni, Nr. 26, S. 4927–4930. – ISSN 1079–7114

[185] Shah, Syed I. ; Nandipati, Giridhar ; Kara, Abdelkader ; Rahman, Talat S.: Extended pattern recognition scheme for self-learning kinetic Monte Carlo simulations. In: *Journal of physics. Condensed matter : an Institute of Physics journal* 24 (2012), September, Nr. 35, S. 354004. – ISSN 1361–648X

[186] Pacheco, J. ; Prates Ramalho, J.: First-Principles Determination of the Dispersion Interaction between Fullerenes and Their Intermolecular Potential. In: *Physical Review Letters* 79 (1997), November, Nr. 20, S. 3873–3876. – ISSN 0031–9007

[187] Chiutu, C. ; Sweetman, A. M. ; Lakin, A. J. ; Stannard, A. ; Jarvis, S. ; Kantorovich, L. ; Dunn, J. L. ; Moriarty, P.: Precise Orientation of a Single C60 Molecule on the Tip of a Scanning Probe Microscope. In: *Physical Review Letters* 108 (2012), Juni, Nr. 26, S. 268302. – ISSN 0031–9007

[188] Babadi, M ; Everaers, R ; Ejtehadi, M R.: Coarse-grained interaction potentials for anisotropic molecules. In: *The Journal of chemical physics* 124 (2006), Mai, Nr. 17, S. 174708. – ISSN 0021–9606

[189] Saito, S ; Oshiyama, A: Cohesive Mechanism and Energy Bands of Solid C60. In: *Physical Review Letters* 66 (1991), Mai, Nr. 20, S. 2637–2640. – ISSN 1079–7114

[190] Troullier, N ; Martins, José L.: Structural and electronic properties of C60. In: *Physical Review B* 46 (1992), Juli, Nr. 3, S. 1754–1765. – ISSN 0163–1829

[191] Gravil, P. A. ; Devel, M ; Lambin, P ; Bouju, X ; Girard, C ; Lucas, A. A.: Adsorption of C60 molecules. In: *Physical Review B* 53 (1996), Januar, Nr. 3, S. 1622–1629. – ISSN 0163–1829

[192] Chen, Shuhan ; Liang, Jingshu ; Mo, Yunjie ; Luo, Difan ; Jiang, Shaoji: Onset of shadowing-dominated growth of Ag films in glancing angle deposition: Kinetic Monte Carlo simulation. In: *Applied Surface Science* 264 (2013), Januar, S. 552–556. – ISSN 01694332

[193] Latz, A ; Brendel, L ; Wolf, D E.: A three-dimensional self-learning kinetic Monte Carlo model: application to Ag(111). In: *Journal of Physics: Condensed Matter* 24 (2012), Februar, S. 485005. – ISSN 0953–8984

[194] Reimann, P ; Schmid, GJ ; Hänggi, P: Universal equivalence of mean first-passage time and Kramers rate. In: *Physical Review E* 60 (1999), Nr. 1, S. R1–R4

[195] Pólya, G.: Über eine Aufgabe der Wahrscheinlichkeitsrechnung betreffend die Irrfahrt im Straßennetz. In: *Mathematische Annalen* 84 (1921), S. 149 – 160

[196] Kowarik, Stefan ; Gerlach, Alexander ; Sellner, Stefan ; Cavalcanti, Leide ; Schreiber, Frank: Dewetting of an Organic Semiconductor Thin Film Observed in Real-time. In: *Advanced Engineering Materials* 11 (2009), April, Nr. 4, S. 291–294. – ISSN 14381656

[197] Pierre-Louis, O. ; Chame, Anna ; Saito, Yukio: Dewetting of a Solid Monolayer. In: *Physical Review Letters* 99 (2007), September, Nr. 13, S. 136101. – ISSN 0031–9007

[198] Truhlar, DG ; Garrett, BC ; Klippenstein, SJ: Current status of transition-state theory. In: *The Journal of Physical Chemistry* 100 (1996), S. 12771–12800

[199] Anslyn, Eric V. ; Doughtery, Dennis A.: Transition State Theory and Related Topics. In: *Modern Physical Organic Chemistry University Science Books*. University Science Books, 2006, Kapitel 7.2, S. 365–373

[200] Fischer, J E. ; Werwa, E ; Heiney, P A.: Pseudo-epitaxial C60 films prepared by a hot-wall method. In: *Applied Physics A* 56 (1993), S. 193

[201] Goodwin, Andrew L. ; Calleja, Mark ; Conterio, Michael J. ; Dove, Martin T. ; Evans, John S O. ; Keen, David a. ; Peters, Lars ; Tucker, Matthew G.: Colossal positive and negative thermal expansion in the framework material Ag3[Co(CN)6]. In: *Science (New York, N.Y.)* 319 (2008), Februar, Nr. 5864, S. 794–7. – ISSN 1095–9203

[202] Krauss, Tobias N.: *Directed Self-Assembly of Organic Semiconductors in Different Dimensionalities*, Universität Stuttgart, PhD thesis, 2009

[203] Smilgies, Detlef-M.: Geometry-independent intensity correction factors for grazing-incidence diffraction. In: *Review of Scientific Instruments* 73 (2002), Nr. 4, S. 1706. – ISSN 00346748

[204] Hadicke, E ; Graser, F: Structures of eleven perylene-3, 4: 9, 10-bis (dicarboximide) pigments. In: *Acta. Cryst. C* 42 (1986), S. 189–195

[205] Werzer, O ; Kunert, B ; Roblegg, E ; Zimmer, A ; Oehzelt, M ; Resel, R: Surface Induced Order of Solution Processed Caffeine Needles on Silica and Muscovite Mica. In: *Crystal Growth & Design* 13 (2013), Nr. 1322-1328

[206] Ehmann, HMA ; Werzer, Oliver: Surface mediated structures: stabilization of metastable polymorphs on the example of paracetamol. In: *Crystal Growth & Design* 14 (2014), Nr. 3680-3684

[207] Bommel, Sebastian: *Echtzeit-Röntgen- und optische Untersuchungen am organischen Halbleiter DIP und am molekularen Schalter TBA*, Humboldt-Universität zu Berlin, Master Thesis, 2011

[208] Drummy, L. F. ; Martin, D. C.: Thickness-Driven Orthorhombic to Triclinic Phase Transformation in Pentacene Thin Films. In: *Advanced Materials* 17 (2005), April, Nr. 7, S. 903–907. – ISSN 0935–9648

[209] Fleet, Aaron ; Dale, Darren ; Woll, AR ; Suzuki, Y. ; Brock, JD: Multiple time scales in diffraction measurements of diffusive surface relaxation. In: *Physical review letters* 96 (2006), Februar, Nr. 5, S. 055508. – ISSN 0031–9007

[210] Desai, TV ; Kish, ER ; Woll, AR ; Engsstrom, JR: Growth of N,N-Ditridecylperylene-3, 4, 9, 10-tetracarboxylic Diimide on Self-Assembled Monolayers: Adsorption Dynamics and Sub-and Multilayer Thin Film Growth. In: *The Journal of Physical Chemistry C* 115 (2011), S. 18221–18234

[211] Zhang, XueNa: *Mechanisms of Growth and Structural Properties of Diindenoperylene on Metal, Dielectric, and Organic Surfaces*, University Stuttgart, PhD thesis, 2008

A Appendix

A.1 Smooth organic thin films of PTCDI-C_8 : layer-by-layer growth of PTCDI-C_8 on SiO_2

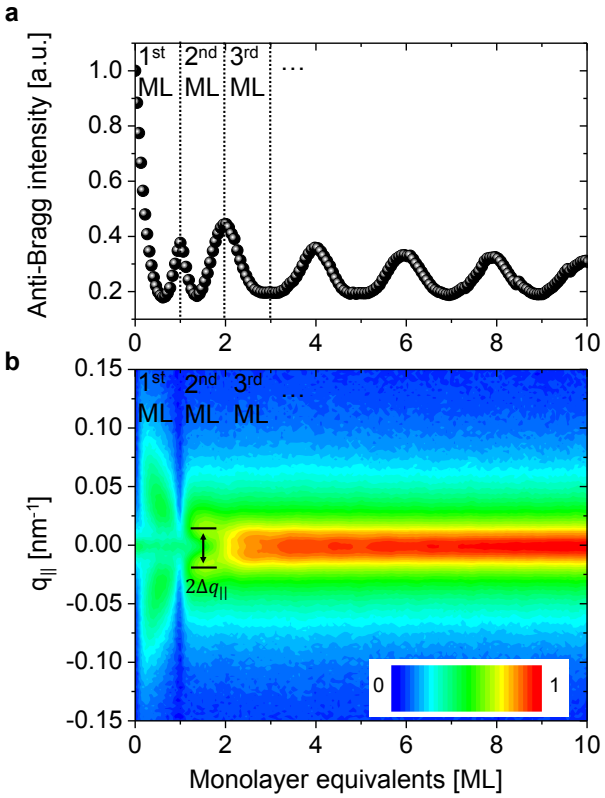

Figure A.1: Smooth thin film of PTCDI-C_8 on SiO_2 indicated by distinct x-ray growth oscillations. The intensity damping is due to the increasing roughness during the growth.

The temperature-dependent crystal structure of PTCDI-C_8 on SiO_2 exhibits anomalous thermal expansion, which is connected with cooperative rotational motions on the molecular scale. The investigated thin film with a thickness of 15 nm (7.5 ML) are highly crystalline but also very smooth. This is indicated by distinct x-ray growth oscillations during the growth of PTCDI-C_8 at a temperature of 100 °C and a deposition rate of 0.05

ML/min, which are shown in Figure A.1. Note, that a detailed analysis of the growth of PTCDI-C_8 goes beyond the scope of this thesis.

In Figure A.1a the anti-Bragg intensity for PTCDI-C_8 as a function of the monolayer equivalents is shown. Pronounced anti-Bragg growth oscillations have been observed, which indicates a smooth layer-by-layer growth. Similar growth oscillations were already observed for PTCDI-C_{13} [210]. The intensity damping is due to the increasing roughness during the growth. Note, that no post-growth dewetting has been observed and the film remains smooth after growth. As for the experiments on the multilayer growth of C_{60} the diffuse x-ray scattering has been measured simultaneously, which is shown in Figure A.1b. During the growth of PTCDI-C_8 diffuse intensity oscillations appear, which are indicative for smooth layer-by-layer growth. Please see section 4.2.1 for a detailed explanation on the appearance of growth oscillations in the diffusely scattered as well as the anti-Bragg intensity. The average island distance D causes two characteristic maxima in the diffuse scattering along $q_{||}$. After the growth of 5 monolayer the diffuse scattering is close to the resolution limit. Nevertheless, following equation 4.5 the island density can be calculated during the growth of the first five monolayer. This island density is shown in Figure A.2.

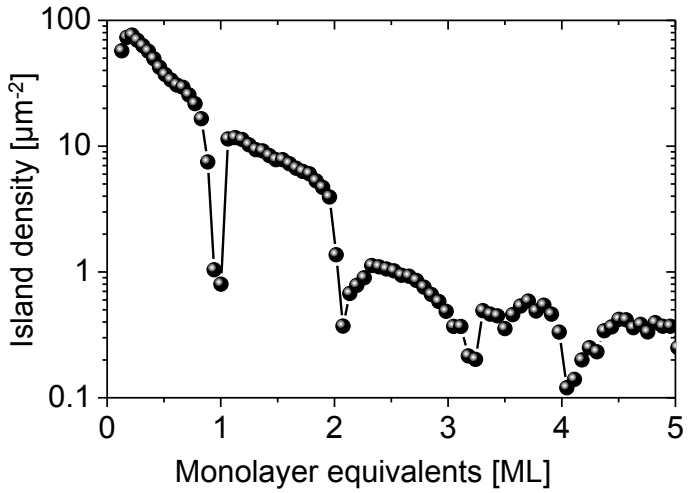

Figure A.2: Island density during the growth of PTCDI-C_8 on SiO_2. The growth of the first two monolayer is almost exclusively dominated by coalescence.

The evolution of island density within the growth of one monolayer is characterized by the three growth regimes of nucleation, lateral growth and coalescence (see section 4.2.1 for an more detailed explanation of these regimes). The growth of the first two monolayer is almost exclusively dominated by the coalescence regime. This phenomena was also observed for DIP on SiO_2 [99, 211].

A.2 Atomic form factor calculations and dispersion correction factors

The atomic form factor for bonded electrons consists of the atomic form factor for free electrons $f^0(\boldsymbol{q})$ and the dispersion correction factors $f'(E)$ and $f''(E)$.

$$f(\boldsymbol{q}, E) = f^0(\boldsymbol{q}) + f'(E) + if''(E) \tag{A.1}$$

The atomic form factor for free electrons can be approximated by

$$f^0(\boldsymbol{q}) = \sum_{j=1}^{4} a_j e^{-b_j q^2} + c_0 \tag{A.2}$$

with

	H-atom	C-atom	O-atom	N-atom
a_1	0.493002	2.31	3.0485	12.2126
b_1	10.5109	20.8439	13.2771	0.0057
a_2	0.322912	1.02	2.2868	3.1322
b_2	26.1257	10.2075	5.7011	9.8933
a_3	0.140191	1.5886	1.5463	2.0125
b_3	3.14236	0.5687	0.3239	28.9975
a_4	0.04081	0.856	0.867	1.1663
b_4	57.7997	51.6512	32.9089	0.5826
c_0	0.00308	0.2156	0.2508	-11.529

Table A.1: Parameters for describing the atomic form factors for each kind of atom

The dispersion correction factors are energy-dependent.

	H-atom	C-atom	O-atom	N-atom
f'	0	0.0075	0.02242	0.01331
f''	0	0.003326	0.0122124	0.006535

Table A.2: Dispersion correction factors for an photon energy of 12.70 keV

A.3 Calculated and experimentally observed Bragg intensities for PTCDI-C_8 for various temperatures.

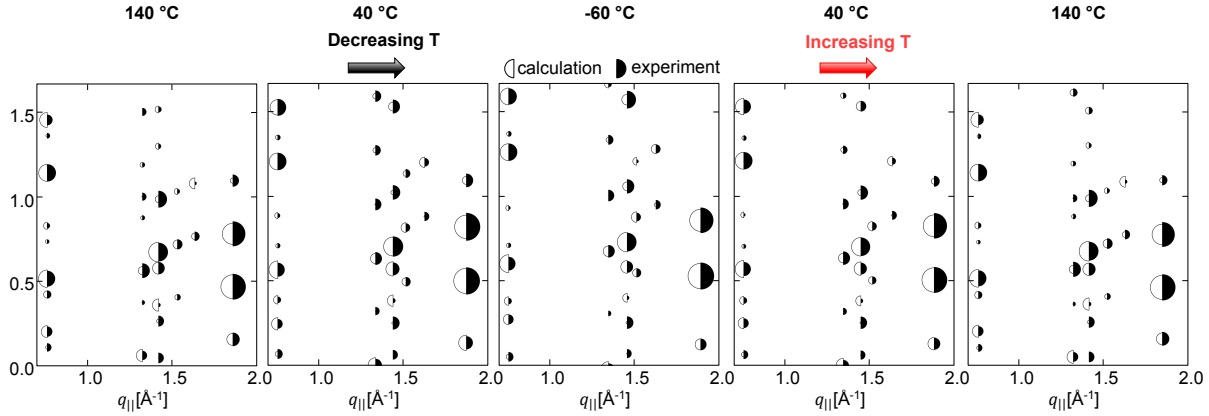

Figure A.3: Calculated and experimentally observed Bragg intensities for various temperatures. Excellent agreement not only for the initial temperature of 140 °C is observed but for all employed temperatures.

Publications

1. **S. Bommel**, N. Kleppmann, C. Weber, H. Spranger, P. Schäfer, J. Novak, S.V. Roth, F. Schreiber, S.H.L. Klapp, S. Kowarik
   "Unravelling the multilayer growth of the fullerene C_{60} in real time"
   Nature Communications 5, 5388 (2014)

2. **S. Bommel**, H. Spranger, S.V. Roth, S. Kowarik
   "Temperature dependent post-growth dewetting of the fullerene C_{60} on mica"
   in preparation

3. **S. Bommel**, L. Pithan, A. Zykov, P. Beyer, G. Santoro, S.V. Roth, S. Kowarik
   "Anomalous thermal expansion in organic thin films connected with concerted molecular rotations of PTCDI-C_8 "
   in preparation

4. **S. Bommel**, L. Pithan, A. Zykov, P. Beyer, G. Santoro, S.V. Roth, S. Kowarik
   "Study of thin film morphology and crystallinity of the organic semiconductor PTCDI-C_8 using X-ray scattering methods"
   Photon Science - HASYLAB Annual Report 2012

5. **S. Bommel**, C. Weber, J. Novak, P. Schäfer, S.V. Roth, S. Kowarik
   "Real-time and in-situ x-ray scattering during the growth of C_{60} on mica"
   Photon Science - HASYLAB Annual Report 2011

6. C. Weber, T. Liebig, M. Gensler, L. Pithan, **S. Bommel**, D. Bléger, J.P. Rabe, S. Hecht, S. Kowarik
   "Light-controlled "molecular zippers" based on azobenzene main chain polymers"
   Macromolecules 48, 1531-1537 (2015)

7. L. Pithan, C. Cocchi, H. Zschiesche, C. Weber, A. Zykov, **S. Bommel**, S.J. Leake, P. Schäfer, C. Draxl, S. Kowarik
   "Light Controls Polymorphism in Thin Films of Sexithiophene"
   Crystal Growth and Design 15, 1319-1324 (2015)

8. S. Yu, G. Santoro, K. Sakar, B. Dicke, P. Wessels, **S. Bommel**, R. Döhrmann, J. Perlich, M. Kohlmann, E. Metwalli, J. F.H. Risch, M. Schwartzkopf, M. Drescher, P. Müller-Buschbaum, S.V. Roth
   "Formation of Al Nanostructures on Alq3: An in Situ Grazing Incidence Small Angle X-ray Scattering Study during Radio Frequency Sputter Deposition"
   Journal of Physical Chemistry Letters 4, 3170 (2013)

9. R. Döhrmann, S. Botta, A. Buffet, G. Santoro, K. Schlage, M. Schwartzkopf, **S. Bommel**, J.F.H. Risch, R. Mannweiler, S. Brunner, E. Metwalli, P. Müller-Buschbaum, S.V. Roth
   "A new highly automated sputter equipment for in-situ investigation of deposition processes with synchrotron radiation"
   Review of Scientific Instruments 84, 043901 (2013)

Presentations

1. *"Temperature-dependent molecular orientation of the organic semiconductor PTCDI-C_8: Optical and structural properties"*
   DPG Spring-Meeting Condensed Matter 2014, **Dresden, Germany**

2. *"X-Ray Scattering for Exploring the Surface Structure of Topological Insulators and (Molecular) Adlayers"*
   2nd Humboldt-Princeton University Workshop 2014, **Princeton, USA**

3. *"Real-Time Characterization of Nucleation and Step-Edge Crossing during the Growth of the Fullerene C_{60} using X-ray Scattering"*
   19th International Vacuum Congress (IVC)/ 15th International Conference on Solid Surfaces (ISS), 2013, **Paris, France**

4. *"Real-time and in situ μGISAXS and x-ray growth oscillations during multi-layer growth of the fullerene C_{60}"*
   International Conference on X-ray Optics and Microanalysis (ICXOM), 2013, **Hamburg, Germany**

5. "Real-time and in-situ investigations of the nucleation and diffusion during the growth of the fullerene C_{60} using X-ray scattering"
   DPG Spring-Meeting Condensed Matter 2013, **Regensburg, Germany**

6. *"Real-time and in-situ growth study of the fullerene C_{60}: Time-resolved organic thin film morphology studied by GISAXS"*
   International Conference of Small-Angle Scattering 2012, **Sydney, Australia**

7. *"Growth-study of the fullerene C_{60} on mica using real-time and in-situ x-ray scattering"*
   3rd TU Munich-HASYLAB Colloquium 2012 "The metal-polymer interface", **Munich, Germany**

8. *"In-situ investigations of organic deposition using X-ray scattering"*
   NANO & MICRO Sciences and Technologies Workshop, Helmholtz Association, **Berlin, Germany**

9. *"Organic Molecular Beam Deposition (OMBD) at PETRA III: Real-time and in-situ X-ray scattering"*
   2nd Soft Matter & Life Science Workshop, Helmholtz Association, **Potsdam, Germany**

Posters

10. DESY Photon Science User Meeting 2015, Hamburg, Germany
11. SXNS-13 International Conference on Surface X-Ray and Neutron Scattering 2014, Hamburg, Germany
12. DPG Spring-Meeting Condensed Matter 2014, Dresden, Germany
13. DESY Photon Science User Meeting 2014, Hamburg, Germany
14. GISAXS 2013, Hamburg, Germany
15. DESY Photon Science User Meeting 2013, Hamburg, Germany
16. DPG Spring Meeting Condensed Matter 2012, Berlin, Germany
17. "2nd Soft Matter & Life Science Workshop", Helmholtz Association, Potsdam, Germany
18. DESY Hasylab User Meeting 2012, Hamburg, Germany

Acknowledgment

This thesis was prepared from September 2011 to February 2015 in a collaborative research project between the Humboldt-University Berlin and DESY in Hamburg. I want to acknowledge everyone who have helped, supported and encouraged me during the realization of this thesis.

First and formost, I would like to thank my supervisor, **Prof. Stefan Kowarik**, for giving me the opportunity to perform such exciting research. Furthermore, I want to acknowledge his support, encouragement and his advice in the last years. Especially, I thank him for his ideas and for answering my questions concerning growth and x-ray scattering.

I am particularly grateful to **Prof. Edgar Weckert**, who gave me the possibility to work at DESY in a pleasant environment and for fruitful discussions in our group meeting pushing our research forward. I also want to acknowledge **Prof. Helmut Dosch**, the director of DESY, for initiating the collaborative research project between DESY and Humboldt-University Berlin. I would like to thank **Dr. Stephan V. Roth** for his help during the beamtimes as well as during the analysis of the obtained data and for stimulating discussions. I thank **Dr. Alke Meents** for his support in my research and his administrative help at DESY.

I am grateful to **Prof. Sabine H.L. Klapp and Nicola Kleppmann** for the simulations on the growth of the fullerene C_{60}. Furthermore, I thank them for stimulating discussions on our results and Nicola especially for her patience in explaining me the theoretical aspects of growth. Furthermore, I thank **Prof. Frank Schreiber** for his ideas and his encouragement for our research on the growth of the fullerene C_{60} .

Dr. Gonzalo Santoro and Dr. Shun Yu for their experimental assistance during the beamtimes and the scientific but also non-scientific discussions we had. I would like to acknowledge **Dr. Peter Schäfer** for his advice on x-ray scattering analysis, our stimulating discussions and his help during the C_{60} beamtime.

I am in particularly grateful to my great colleagues **Christopher Weber, Anton Zykov, Linus Pithan, Holger Spranger** and **Paul Beyer** for their support and help during beamtimes and in-house experiments. I would like to thank **Philip Roedig, Dennis Goeries and Matthias Schwartzkopf** and **all colleagues of P03 and P11** for the inspiring and stimulating atmosphere in our team.

I am grateful to Merle for her unlimited support and patience during the realization of this work. Last but not least I would like to thank my parents, without which I would not be at this stage where I am today.

Utilities

Als Hilfsmittel für die Anfertigung dieser Arbeit wurden verwendet:

- Latex,
- Origin 8.6 and Origin 9,
- Mathematica 9,
- Microsoft Powerpoint 2010 (Illustrationen),
- Gwyddion 2.36,
- alle angegebenen Quellen.

Selbständigkeitserklärung

„Ich erkläre eidesstattlich, dass ich die Dissertation selbständig und nur unter Verwendung der von mir gemäß § 7 Abs. 3 der Promotionsordnung der Mathematisch-Naturwissenschaftlichen Fakultät, veröffentlicht im Amtlichen Mitteilungsblatt der Humboldt-Universität zu Berlin Nr. 126/2014 am 18.11.2014 angegebenen Hilfsmittel angefertigt habe.

Ich habe mich nicht anderwärts um einem Doktorgrad im Promotionsfach Physik beworben und besitze keinen Doktorgrad im Promotionsfach Physik.

Die Promotionsordnung der Mathematisch-Naturwissenschaftlichen Fakultät, veröffentlicht im Amtlichen Mitteilungsblatt der Humboldt-Universität zu Berlin Nr. 126/2014 am 18.11.2014 habe ich zur Kenntnis genommen."

Sebastian Bommel
16. März 2015